Forschungszentrum Jülich
in der Helmholtz-Gemeinschaft

50 Jahre / Zukunft

Molecular Electronic Building Blocks Based on Self-Assembled Monolayers

Björn Lüssem

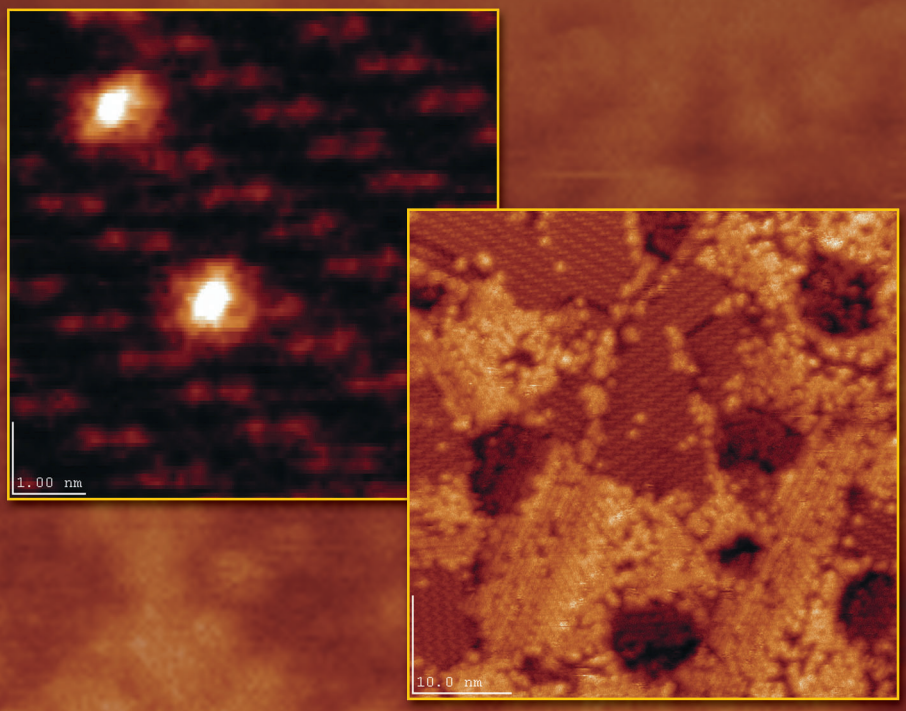

Informationstechnik
Information Technology

Schriften des Forschungszentrums Jülich
Reihe Informationstechnik / Information Technology Band / Volume 12

Forschungszentrum Jülich GmbH
Institut für Festkörperforschung 6: Elektronische Materialien

Molecular Electronic Building Blocks Based on Self-Assembled Monolayers

Björn Lüssem

Schriften des Forschungszentrums Jülich
Reihe Informationstechnik/Information Technology Band/Volume 12

ISSN 1433-5514 ISBN 3-89336-454-4

Bibliographic information published by the Deutsche Nationalbibliothek.
The Deutsche Nationalbibliothek lists this publication in the Deutsche
Nationalbibliografie; detailed bibliographic data are available in the
Internet at <http://dnb.d-nb.de>.

Publisher and Distributor:	Forschungszentrum Jülich GmbH Zentralbibliothek, Verlag 52425 Jülich Phone +49 (0) 24 61 61-53 68 · Fax +49 (0) 24 61 61-61 03 e-mail: zb-publikation@fz-juelich.de Internet: http://www.fz-juelich.de/zb
Cover Design:	Grafische Medien, Forschungszentrum Jülich GmbH
Printer:	Grafische Medien, Forschungszentrum Jülich GmbH
Copyright:	Forschungszentrum Jülich 2006

Schriften des Forschungszentrums Jülich
Reihe Informationstechnik / Information Technology Band / Volume 12

D 82 (Diss., RWTH Aachen, 2006)

ISSN 1433-5514
ISBN-10: 3-89336-454-4
ISBN-13: 978-3-89336-454-1

Molekularelektronische Bausteine basierend auf selbstorganisierten Monolagen

Die Entwicklung der Mikroelektronik, oft beschrieben durch das Moore'sche Gesetz, wird getragen durch eine stetige Verkleinerung der elektronischen Bauteile. Es wird jedoch damit gerechnet, dass die Miniaturisierung der CMOS Technik als der bisher vorherrschenden Herstellungstechnik für Transistoren und Schaltungen in 15 bis 20 Jahren durch grundlegende physikalische und technologische Begrenzungen in eine Sättigung laufen wird.

Eine zurzeit diskutierte Alternative ist die molekulare Elektronik. Es wird versucht, einzelne Moleküle zu kontaktieren und die Stromtransporteigenschaften dieser Moleküle für die Informationsspeicherung oder für komplexe logische Schaltungen zu benutzen. Eine Möglichkeit der Kontaktierung von einzelnen Molekülen wird in dieser Arbeit vorgestellt: die Rastertunnelmikroskop(RTM)-Kontaktierung von Molekülen, die mit Hilfe einer speziellen Einlagerungstechnik in einer monomolekularen Schicht isolierten werden. Hierzu wird auf einer atomar glatten, (111)-orientierten Goldschicht eine selbstorganisierte Monolage aus isolierenden Alkanthiolen abgeschieden. In diese Monolage werden in einem zweiten Schritt die zu kontaktierenden Moleküle, in dieser Arbeit Biphenylthiole, eingelagert. Die Goldschicht bildet den unteren Kontakt zu dem Molekül, der obere Kontakt wird durch eine RTM Spitze hergestellt, so dass der Strom von der Goldschicht über das Molekül zur Spitze fließt. Der obere und untere Kontakt unterscheiden sich leicht: Während das Molekül kovalent an das Gold gebunden ist, besteht der obere Kontakt nur aus einer losen Kopplung der RTM Spitze über einen Vakuumspalt mit dem Molekül.

Im Rahmen der vorliegenden Arbeit werden alle Schritte zum Aufbau der eben beschriebenen Kontaktierungsmethode durchgeführt. Insbesondere wird die Goldschicht optimiert, verschiedene Depositionsmethoden zur Herstellung von Monolagen aus Alkanthiolen evaluiert, Monolagen aus Biphenylthiolen mittels RTM im Ultrahochvakuum charakterisiert und Biphenylthiole in Monolagen aus Alkanthiolen eingebettet.

Ein Schwerpunkt der Arbeit liegt neben der Herstellung und der Bestimmung der Struktur der Molekülschichten auf der Charakterisierung des Stromtransportes durch Biphenylthiole. Zwei verschiedene Methoden werden dabei angewendet. Mit Hilfe von Strom/Abstandskurven über einer Monolage aus Biphenylthiolen wird gezeigt, dass der Strom durch die Molekülschicht am besten durch einen Tunnelprozess beschrieben wird. Die Abklinglänge der Biphenylgruppe kann aus den Messungen bestimmt werden ($\beta = 4.7 \pm 0.8 nm^{-1}$).

Zudem wird aus den unterschiedlichen Höhen der Alkanthiole und der Biphenylthiole in den RTM-Aufnahmen der gemischten Monolagen (Alkanthiole mit eingebauten Biphenylthiolen) auf die Stromtransporteigenschaften geschlossen. Wie auch mit der vorhergehenden Messmethode wird die Abklinglänge der Biphenylgruppe bestimmt ($\beta \sim 5 nm^{-1}$).

Die Bedeutung dieser Arbeit liegt nicht nur in der Charakterisierung des Stromtransportes von Biphenylthiolen, sondern ebenso in der Entwicklung einer Methodik, die die Messung der Leitfähigkeit einer ganzen Klasse von Molekülen ermöglicht. Dadurch wurde ein Hilfsmittel entwickelt, das ein breiteres Verständnis des Stromtransportes durch einzelne Moleküle ermöglicht.

Molecular Electronic Building Blocks Based on Self-Assembled Monolayers

The evolution of microelectronics often described by Moore's law is driven by a continuous downscaling of all electronic devices. However, it is expected that the miniaturisation of the CMOS technology as the currently used technique for the fabrication of transistors and integrated circuits will face fundamental physical limitations within the next 15 to 20 years.

Molecular electronics is one alternative to CMOS. The aim of molecular electronics is to contact single molecules, to utilise the current transport properties of these molecules for information technology and to build complex logical circuits. One method of contacting single molecules is described in this thesis: the method of contacting molecules embedded in a molecular monolayer by scanning tunnelling microscopy (STM). A self-assembled monolayer of insulating alkanethiols is deposited onto an atomically flat gold film. The molecules of interest, in this case biphenylthiols, are embedded into this monolayer in a second deposition step. The gold film represents the bottom contact to the molecule, and the top contact is formed by the STM tip resulting in a current flow from gold across the molecule to the tip. The bottom and top contact are slightly different: Whereas the molecule is covalently bound to the gold, the top contact results from a weak coupling of the tip with the molecule across a vacuum gap.

All necessary steps towards the completion of the aforementioned device setup are carried out in this thesis. In particular, the gold film is optimised, different methods for depositing monolayers of alkanethiols are evaluated, monolayers of biphenylthiols are studied by STM, and finally biphenylthiols are embedded into a self-assembled monolayer of alkanethiols.

One focus of the thesis is the characterisation of the current transport properties of biphenylthiols. Two different methods are used. By current vs. distance spectroscopy it is shown that the current through the monolayer of biphenylthiols is best described by a tunnelling process. The decay length of the biphenyl group can be obtained from these measurements ($\beta = 4.7 \pm 0.8 nm^{-1}$). Furthermore, the height differences between alkanethiols and biphenylthiols as seen in the STM images of mixed monolayers are interpreted in terms of a tunnelling model. As for the preceding method, the decay constant of the biphenyl group is determined ($\beta \sim 5 nm^{-1}$).

The significance of this thesis is not only based on the characterisation of the current transport through biphenylthiols, but also on the development of a setup by which the conductance of a whole class of molecules can be measured. Thereby, a method is developed that helps to gain a broader understanding of current transport through single molecules.

Contents

Acknowledgements

This thesis would not have been possible without the support of many others. First of all, I would like to thank Prof. Rainer Waser for initiating research in this area at his institute, for providing the infrastructure and for motivating me from the beginning of my work.

As my supervisor, Dr. Silvia Karthäuser holds a great share of responsibility for the successful completion of this work. During the last three years, she devoted a lot of her time to discussing my work and to stimulating ideas for further experiments. I would like to express my gratitude for her personal and scientific support.

I would like to thank Lars Müller-Meskamp for his support and successful co-operation. Many results were only possible due to his ideas and his commitment.

Thanks are also due to Manuela Alba for her help and co-operation in the work for chapter 6. For countless gold films I want to thank Hans Haselier, who always prepared these films as fast as possible. For the friendly working conditions I would like to thank Stephan Kronholz, Reji Thomas, Andreas Rüdiger and Christina Rohde.

For the synthesis of the biphenylthiol molecules I am grateful to Prof. Ulrich Simon and Dr. Melanie Homberger.

For help with the STM I acknowledge support from Prof. K. Szot.

Finally, I want to thank my parents for facilitating my education and for always encouraging me in many ways. For her motivation and patience during the last years I want to thank Inga Winkler.

Chapter 1

From Micro- to Nanoelectronics

1.1 Microelectronics

Ever since the invention of the transistor [1] or the first integrated circuit [2], microelectronics have evolved in a tremendous way. Every 18 to 24 months the complexity of integrated circuits is doubled, an observation known as Moores law [3]. This rapid development, also known as the microelectronics revolution, has not only changed science and engineering, but also had a great impact on society [4].

Microelectronics entered our daily life a long time ago. Radios and TVs have become affordable mass products, personal computers can be found in nearly every household, the internet has changed the way we communicate and the whole area of mobile communications has only been possible due to the rapid development of low power, inexpensive integrated circuits.

1.1.1 CMOS - the Basis of Current Microelectronics

In current microelectronics, almost all integrated circuits are based on the Complementary Metal-Oxide-Semiconductor (CMOS) technology. The basic element of a CMOS circuit is a Metal-Oxide Semiconductor Field-Effect Transistor (MOSFET) as shown in figure 1.1. Without a voltage applied to the gate, the highly n-doped source and drain regions are isolated from each other by the p-doped region beneath the gate. Only if the gate voltage exceeds a certain threshold voltage, V_{th}, negative inversion charges accumulate under the gate and a conductive channel between source and drain is formed.

The transistor shown in figure 1.1 is an n-channel enhancement transistor, which means that source and drain are n-doped and a channel of electrons is formed by a positive voltage applied at the gate. For CMOS, the complementary transistor type is also used: a p-channel enhancement transistor. In these transistors, source and drain

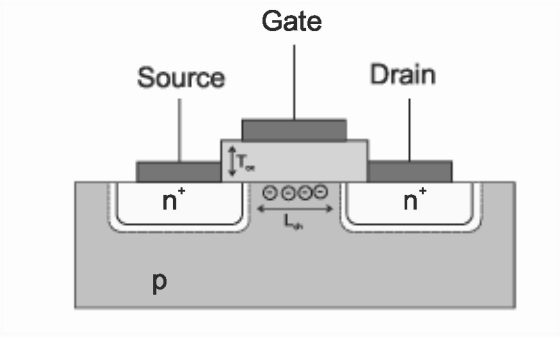

Figure 1.1: An n-channel enhancement transistor

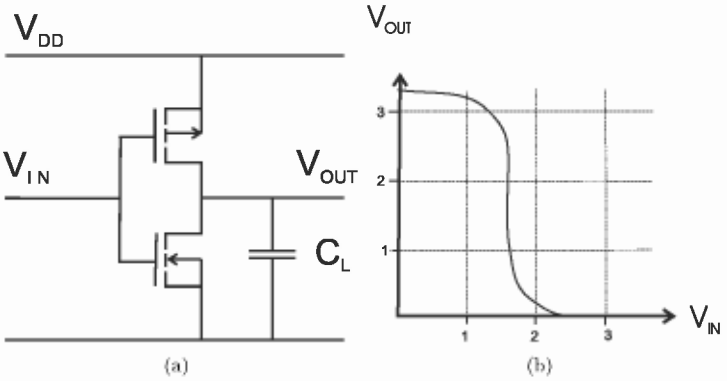

Figure 1.2: CMOS inverter gate is shown in part (a) and its transfer characteristic in part (b)

are p-doped and a conductive p-type channel is formed for negative voltages between gate and source. These two complementary transistor types can be combined to yield a low-power, fast-switching logic gate, shown for an inverter in figure 1.2(a).

CMOS technology has some very important properties which currently make it the best choice for low power microelectronics. Due to the modulation of the drain current by the field effect, these devices show very low static power losses. Furthermore, CMOS leads to fast switching times, a steep transfer characteristic (see figure 1.2(b)) and a full voltage swing from zero to the full supply voltage.

1.1.2 The Evolution of CMOS

The evolution of microelectronics is driven by a continuous decrease in lateral and vertical device dimensions. To keep the electric field constant, the voltage is also reduced

(constant field scaling). This decrease in device size has several interesting consequences.

First of all, by scaling down all device dimensions by a constant factor $\alpha < 1$, all capacitances of the circuit decrease by the same factor α. Furthermore, the saturation current I_{sat} of the transistor also decreases by α [5].

This decrease in capacitance and saturation current has very important implications for the switching speed. The switching time t_d for a single gate is given by the time needed to charge the load capacitance C_L by the saturation current through the channel I_{sat}(see figure 1.2(a)) [6].

$$t_d \approx C_L \frac{V_{DD}}{I_{sat}} \tag{1.1}$$

Considering that the supply voltage V_{DD} is also reduced by approximately α, the delay time is also proportional to α. Therefore, by making the circuit smaller and smaller it becomes faster.

Similary, by downscaling the device by α the power dissipation per circuit

$$P_D \sim V_D I_D \tag{1.2}$$

decreases by α^2. Consequently, the dissipated energy per logical operation $E_d = P_d t_d$, a measure for the efficiency of a certain device or architecture, decreases by α^3.

These dependencies are only valid for ideal scaling, i.e. all device dimensions and the voltage are scaled by the same factor. However, in reality the evolution of the switching time t_d and the energy per operation E_d approximates the aforementioned dependencies. If F denotes the minimum feature size, the switching time scales with $F^{1.4}$ and the energy per operation with $F^{2.7}$ up to feature sizes of above 100nm [6]. For smaller feature sizes, this evolution is expected to slow down gradually.

1.1.3 Where are the Limits?

Like any exponentionally developing technology, CMOS technology has certain limits and the exponential growth of complexity of microprocessors will come to an end in the future. There are several limits that CMOS encounters if downscaling persists, some of them are fundamental and exist in every implementation of a digital circuit.

Fundamental Limits

There are three fundamental limits, known as the *thermodynamic*, the *quantum mechanical* and the *electromagnetic limit* [6–9]. The *thermodynamic limit* states that every irreversible binary operation requires at least an energy of $E_d = k_B T \ln 2$. This limit is closely related to the concept of distinguishability, i.e. the two states representing the binary values 1 and 0 have to be distinguishable and there has to be only a low probability of a spontaneous transition between these states [9].

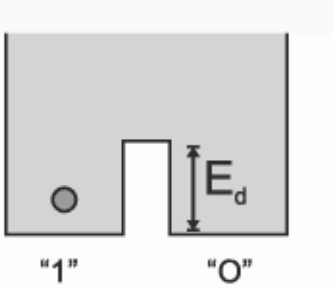

Figure 1.3: Gedanken Model of Zhirnov et al. [9]. If the energy barrier is lower than $E_d < k_B T \ln 2$ (the thermodynamic limit), the hopping probability between the two states becomes 0.5 so that these states are called to be indistinguishable.

In a Gedanken Model, Zhirnov et al. used two energy wells to represent the two logical states. These wells are separated by an energy barrier E_d [9] (see figure 1.3). An electron can change between the two wells if an energy of E_d is supplied to it.

Apart from this intentional switching between the two wells, the electron can also hop from one state to the other due to its thermal energy. The probability of a hopping event is given by $P_{hop} = \exp\left(-\frac{E_d}{k_B T}\right)$. If the energy barrier is lower than the thermodynamic limit, i.e. $E_d < k_B T \ln 2$, the hopping probability is larger than 0.5. The probability of an electron to spontaneously hop to the neighboring well exceeds the probability to stay in its original well. The two wells, or the two logic states associated with them, are therefore called to be indistinguishable.

The *quantum mechanical limit* is given by the Heisenberg Uncertainty relation $\Delta E \Delta t \geq \hbar$. In its consequence, any state with an uncertainty in energy of ΔE needs at least a time $\Delta t = \hbar / \Delta E$ to evolve into a distinguishable state, i.e. any switching event has to last for at least Δt.

The last fundamental limit, the *electromagnetic limit*, is given by the maximum speed of any signal, the speed of light c_0. Within a time Δt any signal can only cover a distance of $a = c_0 \Delta t$, which causes problems for long interconnects.

Material and Device Specific Limits

The fundamental limits of computing cannot be bypassed by any technology, even if this technology is much more advanced than today´s CMOS technology. However, besides these fundamental limits there are some material and device specific limits for CMOS.

One class of device specific limits is caused by the *minimum channel length*. Due to short channel effects like drain induced barrier lowering (DIBL) [10], the length of the channel of MOSFETs, L_{ch}, cannot shrink indefinitely. These short channel effects

decrease the threshold value V_{th} of the transistor, the subthreshold current increases and the transistor no longer operates efficiently as a switch. Consequently, there is an intrinsic switching delay of a MOSFET, given by $t_d = L_{ch}v_d$, where L_{ch} denotes the minimum channel length and v_d the saturation velocity of the electrons. Furthermore, there is a minimum switching energy for the MOSFET given by the energy needed to charge the gate capacitance, $E_{min} \approx \frac{\epsilon_{ox} L_{ch}^2 V_{dd}^2}{2T_{ox}}$, with ϵ_{ox} the permittivity of the gate oxide and T_{ox} the thickness of the gate oxide [7, 8].

The second severe limit for CMOS is a material dependent limit called the *thermal conductance limit* [8]. As the dimensions of CMOS scale down, the energy per operation decreases, but the dissipated power per area increases. This power has to be removed by thermal conduction of the silicon chip, which is believed to be possible up to a limit of $100W/cm^2$ [6]. If this heat conduction limit is reached, the scaling of CMOS is no longer determined by the feature size, but all dimensions are set so that the maximum dissipated power per area is not exceeded. Scaling of CMOS changes from a feature size controlled regime to a power dissipation controlled regime [6].

Further limits to the scaling of CMOS technology are the limit set by the *random placement of dopant atoms*, which leads to statistical variations of the MOSFET parameters as the devices are scaled down. Additionally, as the thickness of the gate oxide T_{ox} is scaled down into the nanometer regime, *leakage currents through the gate oxide* become a severe problem, which increases the static power losses. This problem is tried to be overcome by the use of so called "high-k" materials, materials with a high permitivitiy, so that the thickness of the gate can be increased by keeping the capacitance of the gate constant.

To conclude, CMOS technology which has faciliated the evolution of microelectronics to date will run into severe problems in the near future. The ITRS Roadmap [11] proposes that from about 2019 additional technologies will have to supplement CMOS, if Moores law is continue to be valid.

1.2 Nanolectronics

In the National Nanotechnology Initiative of the USA [12], nanotechnology is defined as the technology of devices with a diameter of less than 100nm. The International Technology Roadmap for Semiconductors (ITRS) predicts the physical gate length of MOSFETs to scale down to 7nm in 2018. In 2005 state of the art transistors already have a physical gate length of 37nm [11]. In this way, microelectronics has already evolved into nanoelectronics.

However, considering that on the nanoscale new physical phenomena occur that can be exploited for new functionalities, nanotechnology and nanoelectronics are not only an evolutionary, but a revolutionary development.

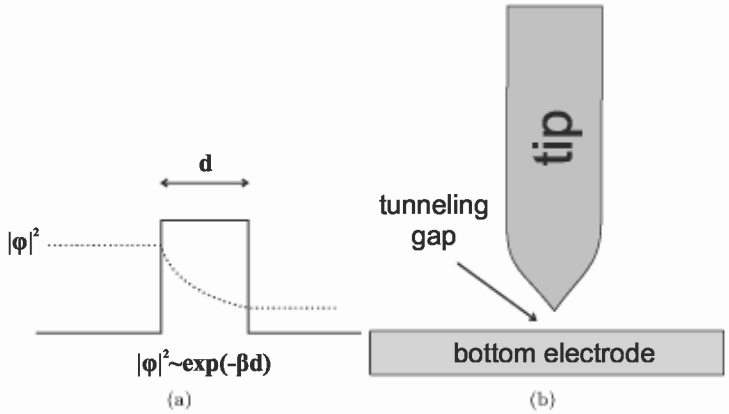

Figure 1.4: In (a) the square of the wave function of an electron which tunnels through a vacuum barrier is shown. In (b) the working principle of an STM is sketched.

1.2.1 Physics at the Nanoscale

Quantum effects

Most important for nanoelectronics, quantum effects become pronounced if the devices are scaled into the nanometer regime. The first major effect of quantum mechanics that comes into play for very small dimensions is *quantum confinement* [13]. If a particle is confined in a small energy well, the electron wave function has to obey certain boundary conditions at the walls of the well, e.g. the wave function has to be zero at the wall for indefinitely deep energy wells. Therefore, standing electron waves develop, and the energies of these standing waves are the only allowed states that an electron can occupy within the well.

Another most interesting effect is *quantum mechanical tunneling*. Classically, an electron with an energy below the energy of an energy barrier cannot pass this barrier and is reflected. However, in quantum mechanics, there is a low probability of the electron penetrating into the barrier and, if the barrier is thin, tunneling through the barrier. The tunneling effect is sketched in figure 1.4(a). The probability of an electron tunneling through an energy barrier is exponentially dependent on the thickness of the tunneling barrier d.

$$P_{tunnel} \sim \exp(-\beta d) \tag{1.3}$$

β is called the decay length and is dependent on the barrier height and the mass of the electron.

Both quantum confinement and quantum mechanical tunneling are indispensable

for understanding molecular conduction. They are used in section 1.3.1 to develop a theoretical basis for the resistance of molecular wires.

Brownian motion

On the nanoscale, all objects such as atoms or molecules show a statistical, undirected motion called *Brownian motion*. For example, the drift velocity of electrons due to an external electric field is only defined as a statistical average over many electrons. If the motion of a single electron is followed, it will show a seemingly chaotic behavior and will move in every direction. Only if the motion of the electron is tracked over a longer period of time or if the average of many electrons is taken, do these electrons show a directed motion along the electric field.

The average energy of any particle due to its Brownian motion depends on the temperature. Therefore, for many observations on the nanoscale, the objects are cooled down to very low temperatures to freeze in the inherent motion of particles. This allows to observe single molecules or atoms. In this thesis, a different way of fixing single molecules is shown: the molecules are embedded into a host matrix of different, insulating molecules, so that the molecules cannot move on the surface and are fixed in one adsorption site (see chapter 5).

Stickiness

Due to van der Waals or dispersion forces, all nano-objects tend to stick together. This "stickiness" of small objects is used, for example, in organic molecular beam epitaxy (OMBE). Molecules are thermally evaporated and a substrate is held into the beam of these evaporated molecules. Although the molecules do not chemically bind to the substrate, they stick to the surface and a layer of the organic material starts to grow.

On the other hand, this stickiness can be undesirable. If, for example, small clusters of only a few gold molecules are prepared[1], they have to be prevented from sticking to their neighboring clusters and building larger clusters. Therefore, these gold clusters are protected by a ligand shell of organic molecules.

Besides the quantum effects, the brownian motion and the stickiness of small objects, there are other physical effects at the nanoscale that are of great importance for nanotechnology in general, but of only limited importance for nanoelectronics, like the *growing importance of viscosity* compared to inertial forces and the *growing strength* of small objects. A more in-depth introduction into physics at the nanoscale can be found in the book by R.A.L. Jones [14].

[1] Such gold clusters are used in chapter 5

1.2.2 STM as a Universal Tool for Nanotechnology

Since the invention of the Scanning Tunneling Microscope (STM) by Binning and Rohrer in the early 1980s [15–17], the STM has become a vital tool for nanotechnology. Nowadays, STM is an essential experimental technique for the whole field of surface science, a fact that led to the Nobel Prize in Physics in 1986 for G. Binning and H. Rohrer [18].

The working principle of an STM is surprisingly simple and is illustrated in figure 1.4(b). A very sharp tip, preferably a tip with only a single atom at its apex, is moved close to a conducting surface. If a voltage is applied between the tip and the surface, a current flows from the tip to the surface. Most importantly, this current can already flow before the tip actually touches the surface. Any gap between the tip and the surface forms an energy barrier and the electrons can tunnel through this barrier if the gap is thin enough (a few nanometers).

As shown in figure 1.4(a), the tunneling current is exponentially proportional to the tunneling distance. Therefore, a small change in the distance between the tip and the surface results in a large change in current and can be easily detected. This property of the tunneling current enables the STM to show a vertical resolution in the sub-angstrom regime.

A two-dimensional image of the surface topography is obtained by scanning with the tip line by line over the surface. This scan can be done in the constant current mode, i.e. the distance between the tip and the surface is controlled by a feedback circuit so that the tunneling current is kept constant. This mode of scanning the surface topography needs a very precise method of positioning the tip, which can be achieved by piezo-ceramic materials. These materials translate an applied voltage into a precise mechanical deformation in the sub-angstrom range.

A theoretical description of the STM has been proposed by Tersoff and Hamann [19]. They show that the tunneling current I_t is proportional to the density of states at the Fermi level of the tip $\rho_{tip}(\epsilon_F)$ and of the surface $\rho_{surf}(\epsilon_F)$ [19, 20]

$$I_t \sim V_t \rho_{tip}(\epsilon_F) \rho_{surf}(\epsilon_F) \tag{1.4}$$

Normal to the surface, the density of states decreases exponentially into the vacuum, confirming the exponential proportionality of I_t to the distance d as obtained by the simple tunneling model [20].

STM provides a surprisingly simple and, compared to electron microscopes, affordable method of imaging individual atoms or molecules on a surface. Besides this application, it can be used to determine the density of states spectroscopically and spatially resolved[2], to move around single atoms [21] or to initiate complex chemical reactions

[2] According to Binning and Rohrer [18] this spatially resolved spectroscopy was their primary objective in building the first STM, not the imaging capabilities of such a microscope.

[22]. But still, probably the most important feature of the STM is the ability of this microscope to reveal the aesthetics of the structures on the nanoscale. Binning best expressed this after having measured the 7×7 reconstruction of Si(111) for the first time. "I could not stop looking at the images. It was like entering a new world. This appeared to me as the unsurpassable highlight of my scientific career and therefore, in a way, its end" [18].

1.3 Molecules as Building Blocks for Nanoelectronics

Current microelectronics, which has already evolved into nanoelectronics, is driven by a continuous decrease in device dimensions. This decrease will cause severe problems in the future, so that new approaches have to be followed to continue the tremendous increase in computational power.

In the ITRS roadmap for emerging devices, several approaches are listed that will complement CMOS from approximately the year 2019 on. One of these approaches is the field of *molecular electronics*, i.e. logical circuits or memory devices made of single or a small number of organic molecules. These devices are projected to show a lower energy per logical operation and to possess lower critical dimensions than silicon based CMOS. Furthermore, the cost per gate is proposed to be lower [11].

Molecular devices have another major advantage over silicon based CMOS. As the device sizes shrink to only a few nanometers, the device parameters become very dependent on the exact composition and size of the device. At its extreme, the composition of the device has to be controlled up to the exact number of atoms. Whereas this precision of fabrication cannot be reached with state of the art lithographic methods, for single molecules organic chemistry provides a method of building nano objects with exactly defined composition and size.

There are several molecules that have been proposed for molecular electronics (see table 1.1 and the molecules shown in [44, 45]). They all show one general feature: the conduction mechanism is very different from the conduction of electrons in larger objects.

1.3.1 Electrical Transport through Single Molecules

A generalized setup for the measurement of electrical transport across single molecules is shown in figure 1.5. A molecule is connected to two electrodes with Fermi levels μ_L and μ_R. The states $|i\rangle$ of the left and $|j\rangle$ of the right contact are filled with electrons according to the Fermi-Dirac distribution $f(\epsilon)$

$$f(\epsilon - \mu) = \frac{1}{1 + \exp\left(\frac{\epsilon - \mu}{kT}\right)} \tag{1.5}$$

Molecule	Proposed Function	References
Alkanethiols ($C_nH_{2n+2}S$)	insulator	[23–25]
Phenylene-ethylene oligomers (Tour Wires)	NDR and memory	[26 28]
Carbon Nanotubes	FET, oscillator, conductor	[29–31]
Oligothiophene	conductor, memory	[32]
Rotaxane	memory	[33]
Fullerene	FET	[34, 35]
Porphyrins	memory	[36]
$C_{16}H_{33}Q$-3CNQ	diode	[37, 38]
$Co(tpy\text{-}(CH_2)_5\text{-}SH)_2$	FET	[39]
Phenylenes	conductor	[25, 40]
Ferrocene	NDR, memory	[41, 42]

Table 1.1: Some molecules that have been proposed for molecular electronics. Please note that recent results suggest that the memory effect of Rotaxane is in fact molecule independent, limiting the use of these molecules [43].

with μ: Fermi level of the right or the left contact, ϵ: energy, k: Boltzman constant, T: temperature.

If a voltage V is applied across the device the Fermi level of the left electrode shifts up by $eV/2$ and the Fermi level of the right electrode shifts down by the same amount. Due to the voltage difference, electrons flow from the left contact to the right. However, only a part of all incident electrons are transmitted from the left to the right since the molecule between the electrodes efficiently scatters the electrons.

The transmission of the electrons is mediated by the energetic levels of the molecule as shown in figure 1.6. Each time a molecular level enters the energy window spanned by the two Fermi levels of the left and right contacts the current rises.

Depending on the strength of the coupling of the electrodes with the molecule, there are two domains of the electron transport: the *weak coupling limit* and the *strong coupling limit*. To distinguish between these two limits, the Hamiltonian H of the whole system has to be split up into several contributions:

$$H = H_L + H_M + H_R + V = H_0 + V \tag{1.6}$$

with H_L, H_M, H_R being the Hamiltonian of the isolated left electrode, molecule and right electrode and V coupling of the three parts. V consists of the coupling of the molecule with the left contact V_{LM}, the coupling of the molecule with the right contact V_{RM} and the coupling of both electrodes V_{LR}.

If one defines a coupling strength Γ_m^L or Γ_m^R for the left and the right contact by the

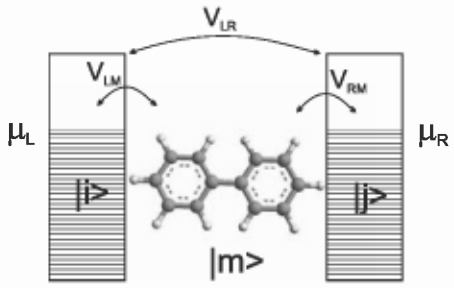

Figure 1.5: Model of a molecular device. The molecule is attached to two electrodes with Fermi levels μ_L and μ_R and eigenstates $|i\rangle$ and $|j\rangle$. Coupling of the molecule with the electrodes is described by the operators V_{LM} and V_{RM}, coupling of the electrodes directly is included by the operator V_{LR}.

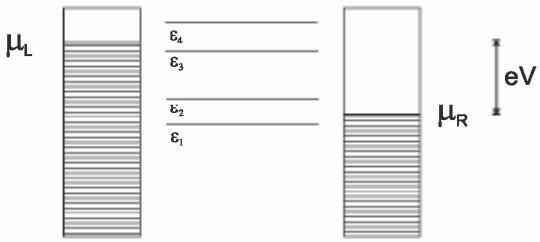

Figure 1.6: Applying a voltage V across the molecule shifts the Fermi levels of the electrodes. Each time a molecular level enters the energy window spanned by the two Fermi levels of the left and right contacts, the current rises sharply.

equation

$$\Gamma_m^L = 2\pi \sum_{i \in L} |V_{i,m}| \, \delta(\epsilon_i - \epsilon_m) \tag{1.7}$$

$$\Gamma_m^R = 2\pi \sum_{j \in R} |V_{m,j}| \, \delta(\epsilon_j - \epsilon_m) \tag{1.8}$$

with m representing the eigenstates of the molecule and i, j the states of the left and the right electrode, the weak coupling limit is valid for small Γ (i.e. $\Gamma \ll \epsilon_m$) and the strong coupling limit corresponds to high Γ.

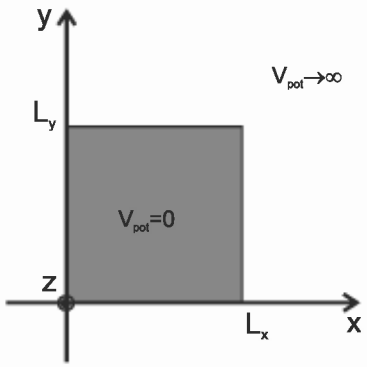

Figure 1.7: Infinitely deep two dimensional potential well as defined by equation (1.10). Along the x and y directions the electrons are confined within an interval $[-L_{x/y}, L_{x/y}]$.

The Strong Coupling Regime

In the strong coupling limit the current is expressed in terms of a transmission coefficient $T(\epsilon)$ by the equation [13, 46]

$$I = \frac{2e}{h} \int T(\epsilon) \left\{ f(\epsilon - \mu_R) - f(\epsilon - \mu_L) \right\} d\epsilon \tag{1.9}$$

To discuss this equation, an idealized one-dimensional wire, approximated by a two-dimensional potential well as shown in figure 1.7, is assumed.

$$V_{pot}(x,y,z) = \begin{cases} 0 & x \in [0, L_x], y \in [0, L_y] \\ \infty & x \notin [0, L_x], y \notin [0, L_y] \end{cases} \tag{1.10}$$

The eigenstates ϕ of this system can be split into separate functions for each direction in space ($\phi(x,y,z) = \varphi_x(x)\varphi_y(y)\varphi_z(z)$). Along the confined axes (x and y) $\varphi_x(x)$ and $\varphi_y(y)$ form standing waves

$$\varphi_x(x) = \sqrt{\frac{2}{L_x}} \sin\left(\frac{\epsilon_p^x 2m}{\hbar^2} x\right) \tag{1.11}$$

$$\varphi_y(y) = \sqrt{\frac{2}{L_y}} \sin\left(\frac{\epsilon_q^y 2m}{\hbar^2} y\right) \tag{1.12}$$

with $\epsilon_p^x = \left(\frac{p\pi}{L_x}\right)^2 \frac{\hbar^2}{2m}$ and $\epsilon_q^y = \left(\frac{q\pi}{L_y}\right)^2 \frac{\hbar^2}{2m}$, $p, q \in N$, i.e. there are different states or modes in the x and y direction. Each mode is denoted by a combination of the numbers p and q.

Along the free axis z, straightforward calculations yield for $\varphi_z(z)$

$$\varphi_z(z) \propto \exp(-jk_z z) \tag{1.13}$$

$$k_z = \sqrt{\frac{2m}{\hbar^2}\left(\epsilon - \epsilon_p^x - \epsilon_q^y\right)} \tag{1.14}$$

with ϵ being the overall energy of the eigenstate. This overall energy is divided between the three directions in space. Whereas part of the energy is stored in standing waves along the x and y direction (ϵ_p^x and ϵ^y), the remaining energy forms a traveling wave in z-direction.

Equations (1.11)-(1.14) show that different modes or eigenstates with different combinations of p and q are possible. Depending on the mode, the wavenumber in z-direction, k_z, is determined by equation (1.14). Usually only modes are considered which have the form of traveling waves. This implies a real wave vector k and a minimum energy for each mode $\epsilon_{p,q}^0 = \epsilon_p^x + \epsilon_q^y = \frac{\hbar^2}{2m}\left[\left(\frac{p\pi}{L_x}\right)^2 + \left(\frac{q\pi}{L_y}\right)^2\right]$.

If a voltage is applied across this idealized one-dimensional wire, a current can be transmitted across these modes. Due to the constant potential along the wire, the modes are scatter-free and the transmission coefficient equals one. Therefore, if only transmission across the lowest mode in the limit of low temperatures is considered, it follows for the conductance of the wire [46]

$$G = \frac{2e^2}{h} \equiv G_0 \tag{1.15}$$

G_0 is called the quantum of conductance and amounts to $77\mu S$. G_0 is the conductance of a single mode. Each time an additional mode enters the energy window $[-eV/2, +eV/2]$, the conductance rises by G_0.

Generally, the energy levels of a molecule are not scatter-free, i.e. $T(\epsilon) < 1$. Furthermore, the transmission coefficient is not constant over a small energy range, but peaks at the molecular levels. Therefore, a general solution of equation (1.9) is only possible by numerical evaluation. An analytical solution for a single level is given by Delerue ([13], section 8.3.2).

The Weak Coupling Regime

In contrast to the strong coupling limit, in the weak coupling limit the transport of the electrons can be seen as a sequential tunneling process from one electrode to the molecule and in a second step from the molecule to the other electrode. The charge carriers spend a certain time on the molecule, giving rise to effects such as the coulomb blockade.

In the weak coupling limit, the current across a single molecular level m is given by

[13]

$$I = \frac{e}{\hbar}\left[f(\epsilon_m - \mu_R) - f(\epsilon_m - \mu_L)\right]\frac{\Gamma_m^L \Gamma_m^R}{\Gamma_m^L + \Gamma_m^R} \tag{1.16}$$

If more than a single molecular level is included in the energy window spanned by the applied voltage, the current cannot be simply obtained by a summation of the contributions of the two levels according to equation (1.16). The transfer of electrons from one molecular level to the other has to be included in the calculation, making the determination of the current more complicated.

Conduction Below the Lowest Mode: Tunneling Currents

Either in the weak or in the strong coupling limit, the transmission of electrons is mediated by the molecular levels. However, if no energy level lies in the energy window which is spanned by the applied voltage, the current can be described by a simple tunneling model. For example, in the strong coupling regime only real solutions of equation (1.14) have been considered so far. If one allows $\boldsymbol{k}$ to become imaginary, the current can be transmitted via decaying or tunneling modes $\varphi_z(z) \propto \exp(-k_z z)$. For long systems, these states are usually neglected, but for small distances that are defined by the length of the molecule as shown in figure 1.5, these modes cannot be disregarded and carry most of the current through the molecule.

If one defines the complex wave vector $\boldsymbol{k}$ as $\boldsymbol{k} = \alpha + i\beta/2$, the k vector is imaginary below the lowest energy level ϵ_0 and it follows for β

$$\beta = 2\sqrt{\frac{2m}{\hbar^2}(\epsilon_0 - \epsilon)} \tag{1.17}$$

The probability of electrons tunneling through the molecule is equal to $\left(\frac{\varphi_z(L_z)}{\varphi_z(0)}\right)^2 = \exp(-\beta L_z)$. Therefore, Tomfohr proposes the following modification of equation (1.15) for the conductance below the lowest molecular level [47]

$$G \approx G_0 \exp(-\beta L_z) \tag{1.18}$$

A more quantitative determination of the tunneling current is possible by the Simmons equation [48], which has frequently been used to discuss the conductance of a molecular film [24, 49]. Simmons showed that the tunneling current j through a thin insulating film with a mean barrier height $\bar{\phi}$ is given by

$$j = j_0\left\{\bar{\phi}\exp\left[-\gamma\beta(\bar{\phi})L_z\right] - (\bar{\phi} + eV)\exp\left[-\gamma\beta(\bar{\phi} + eV)L_z\right]\right\} \tag{1.19}$$

$$j_0 = \frac{e}{2\pi h(\gamma L_z)^2} \tag{1.20}$$

$$\beta(\bar{\phi}) = 2\sqrt{\frac{2m\bar{\phi}}{\hbar^2}} \tag{1.21}$$

with γ a correction factor close to unity.

Depending on the voltage range, Simmons gives several approximations of equation (1.19) [48, 51], which are shown in table 1.2. Whereas in the low bias regime the current is linearly dependent on the voltage, in the intermediate bias regime the current scales with $(V + \delta V^3)$ and exponentially in the high bias regime.

In a first approximation, the distance dependence of the pre-exponential factor (G in the low bias regime and j_0 in the intermediate and high bias regime) can be neglected compared to the exponential factor $\exp[-\beta(\bar{\phi})L_z]$. This approximation, which has been validated in many experiments [24, 52 60], leads to a current vs. distance dependency of

$$I = G(V)\exp[-\beta(\bar{\phi})L_z]V \tag{1.22}$$

In the low bias regime, the conductance G, which is commonly called the contact conductance, is bias independent so that equation (1.18) can be qualitatively recovered.

The length dependence of the conductance of a molecule is determined by the so called decay length β. In later discussions, this decay length is especially helpful to compare the conductance of molecules, which are equally contacted.

1.4 Fabrication of a Nanodevice by Self-Assembly

In current microelectronics, all devices are fabricated by optical lithography. The ITRS roadmap predicts that this optical technique will function down to the 45nm generation and for all later generations new methods such as extreme ultraviolet lithography (EUV), electron projection lithography (EPL), or imprint lithography will have to be developed [11].

Besides these lithographic methods, complex structures can be built by a different technique: *self-organization*. Self-organization generally denotes the increase in order of a system, which is not guided from the outside. Self-organization can be observed in a variety of fields like physics, chemistry, biology or the social sciences.

In chemistry, self-organization is often called self-assembly. A famous example of self-assembly is self-assembled monolayers (SAMs), a class of monolayers of molecules that adsorb spontaneously onto a surface and show a highly ordered structure. Different classes of molecule/substrate combinations are found that show this self-assembling property, e.g. organosilicon derivatives (silanes) on oxidic surfaces [61] and organosulfur compounds on gold [62].

In this thesis, nanodevices are assembled without any patterning step, simply by using the self-assembling properties of SAMs of organosulfur compounds on gold. These

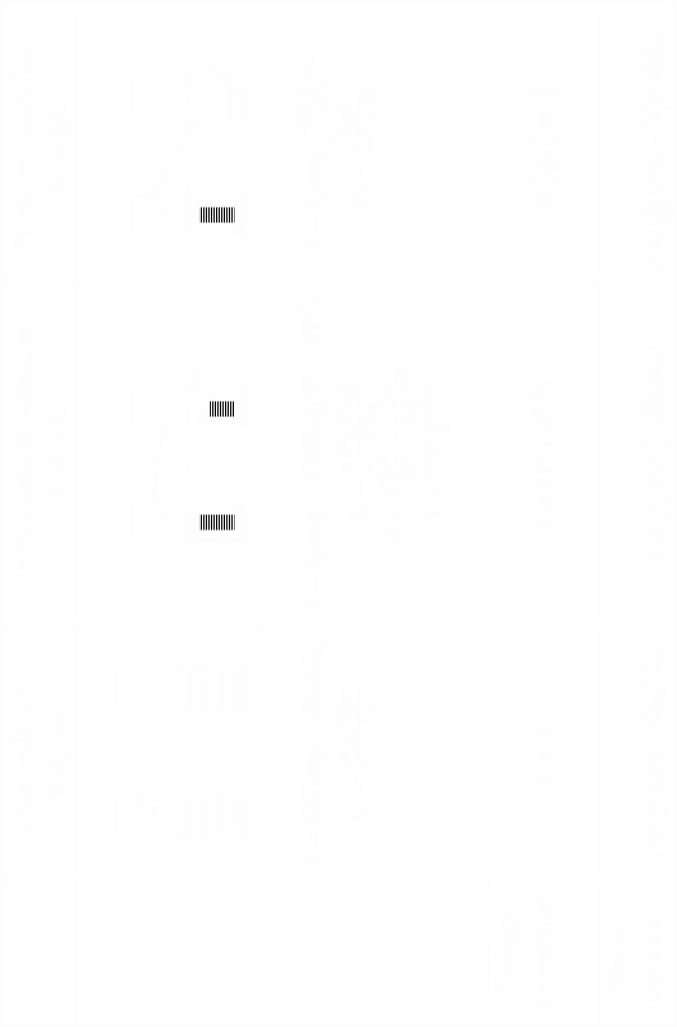

Table 1.2: Different approximations of equation (1.19) for different voltage regimes.

monolayers assemble onto gold in a very well defined manner. The structure of these films is given by the energetic minimum of the overall energy of the whole layer. The overall energy of such a layer is the sum of several contributions.

The *molecule-substrate interaction* energy is probably the most important. SAMs of organosulfur compounds chemisorb onto gold via sulfur-gold bonding. It turns out that on (111)-oriented gold the sulfur head group of the molecule preferentially binds onto the threefold hollow sites, so that the molecules preferentially form a $\left(\sqrt{3} \times \sqrt{3}\right)$ lattice.

Conformational energies are an additional contribution to the overall energy. For example, since every gauche defect in an isolated hydrocarbon chain is energetically costly, in their lowest energy configuration SAMs of alkanethiols ($C_nH_{2n-2}S$) possess a straight molecular backbone, which is directed almost perpendicular to the substrate surface [63]. Furthermore, the sulfur head group preferentially binds to the gold lattice in a sp^3 configuration, giving rise to an angle between the gold, the sulfur and the first carbon atom of $104°$.

The third important contribution is the energy due to *intermolecular interaction*. Whereas, for example, for alkanethiols the intermolecular interaction is mainly due to van der Waals forces, for aromatic thiols π-π interactions prevail.

The resulting structure of an SAM is found as the minimum of the overall energy. As a first approximation, intermolecular distances and the preferred conformation of the molecule can often be obtained by comparison with the bulk crystal structure. This optimized structure has to fit the substrate, i.e. the molecule has to be able to retain its preferred conformation of the bulk crystal structure and has to bind to the gold lattice in the energetically best form, i.e. to the threefold hollow sites.

For alkanethiols it is shown in chapter 3 that the interaction of all forces acting on the molecule leads to a very well-ordered structure. For biphenylthiols it is shown in chapter 4 that for some classes of biphenylthiols this energetic minimum cannot be reached due to steric hinderance.

1.5 Outline of the Thesis

The ITRS roadmap lists several challenges for emergent devices that are supposed to complement CMOS beyond 2019. One of them is the characterization of critical material properties at the nanometer scale for both charge transport and non charge transport devices. Another challange is more concerned with molecular electronics: The identification of contact materials that do not damage the bonding in the molecule [11]. This thesis will contribute to the area of research surrounding these two questions. How can single molecules or a small number of molecules be contacted and how can the current transport through these molecules be characterized?

A test setup is developed by means of which different molecules can be characterized regarding their current transport properties. More specifically, the current transport properties of 4´-methyl-1,1´-biphenyl-4-alkanethiols (CH_3-C_6H_4-C_6H_4-$(CH_2)_n$-SH, **BPn**, n: number of CH_2 units included between biphenyl and sulfur group, see figure 4.1(a)) are studied. These molecules show an interesting combination of insulating parts (the alkane chain) and a part which consists of conjugated double bonds (the biphenyl group), which will increase conductivity. It is shown how the overall transport properties of the whole molecule can be estimated from the transport properties of these two parts.

To electrically characterize the molecule, the decay length $\boldsymbol{\beta}$ is measured (see equation (1.21)). This decay constant is the most important parameter and provides a measure for distinguishing insulating molecules from conducting ones. In the limit of $\boldsymbol{\beta \to 0}$, the conductance of the molecule will be independent of the length of the molecule. Such a molecule would be a perfect molecular wire.

The setup of the nanodevice as shown in figure 1.9 is used. A SAM of insulating alkanethiols (Cn, n: number of CH_2 units) is deposited onto gold. Into this SAM, BPn molecules are embedded and the current transport through these molecules is measured via an STM tip above the BPn molecule. In accordance with this device setup, the thesis is divided into several parts.

Gold Bottom Electrode

In chapter 2, the optimization of the gold bottom electrode is described. The device setup and the measurement method make high demands on the quality of the bottom electrode. SAMs of alkanethiols are known to be highly ordered on (111)-oriented gold. Therefore, the gold films have to be crystalline with a strong (111)-orientation. In later stages of the thesis, the films are studied with molecular resolution, i.e. single molecules are visualized. To facilitate this molecular resolution, the gold substrate has to exhibit a very low surface roughness. This demand is equivalent to the requirement of large, atomically flat terraces of the gold (111)-surface. Furthermore, for STM measurements and for electrically contacting the molecules, the gold film has to be continuous so that it is electrically conductive.

Alkanethiol SAM

The alkanethiol SAM acts as an insulating matrix in which the BPn molecules are embedded. To be able to distinguish the embedded molecules from the surrounding alkanethiol SAM, the structure of the alkanethiol SAM is characterized in detail. Furthermore, the quality of the alkanethiol SAM (cleanliness, large molecular domains and low defect density) is optimized. Details of the characterization and optimization of

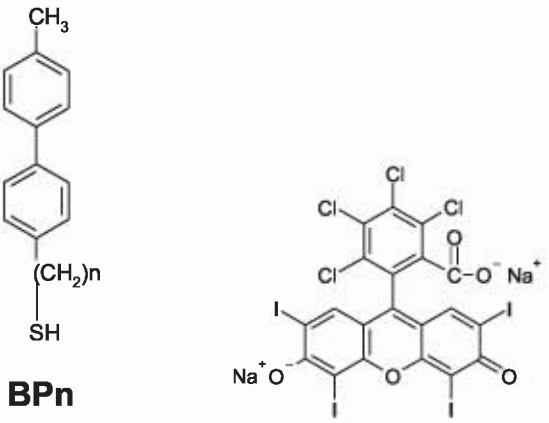

(a) Biphenylthiol (b) Rose Bengal

Figure 1.8: The molecules used in this thesis: biphenylthiol or BPn (CH_3-C_6H_4-C_6H_4-$(CH_2)_n$-SH, n=1..4) (a) and Rose Bengal (b).

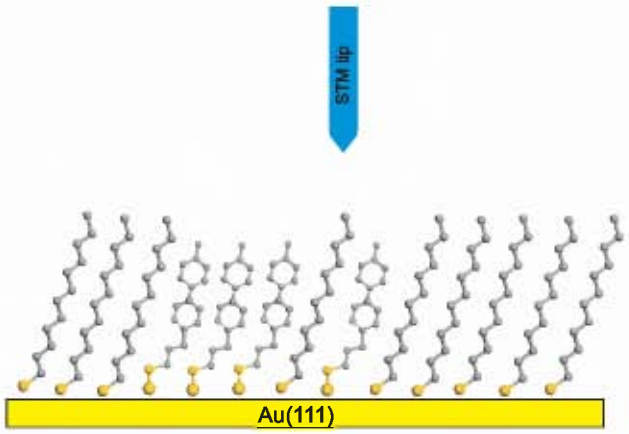

Figure 1.9: Measurement setup for the characterization of the current transport properties of BPn. BPn molecules are embedded into a C12 SAM and are contacted by the gold bottom electrode and an STM tip.

alkanethiol SAMs are given in chapter 3.

Characterization of Full Coverage SAMs of BPn

Before measuring the electron transport through embedded BPn molecules, the electrical properties are studied on full coverage SAMs of biphenylthiols (chapter 4). On the basis of the experimental data a simple model is developed to describe the current transport. Prior to studying the electrical properties of SAMs of BPn, the structure of these films on Au(111) is studied.

Characterization of Embedded BPn Molecules in Alkanethiol SAMs

The embedding process is first studied by embedding simple alkanedithiols into a SAM of alkanemonothiols. These dithiols are further contacted by gold nanoclusters. Following these prelimary studies, BPn molecules are embedded into an alkanethiol SAM. It is shown how the embedding process can be controlled. Depending on the experimental details, the BPn molecules are either isolated or several BPn molecules grouped together and islands of BPn molecules are built in the alkanethiol SAM. The height difference between the surrounding alkanethiol SAM and the BPn islands is interpreted in terms of the model developed in chapter 4.

A Candidate for a Switching Molecule: Rose Bengal

Interesting in terms of applications is a molecule which can switch between two different conduction states. Such a molecule can be used as a building block for a molecular memory. In literature, Rose Bengal (4,5,6,7-Tetrachlor-2',4',5',7'-Tetraiodfluorescein, see figure 1.8) has been proposed as such a switchable molecule. To study the switching effect, an additional device setup is used in Chapter 6. The molecule is sandwiched as a thin film ($\sim 100nm$) between two metallic electrodes (MIM-structure).

Chapter 2

Optimization of the Gold Bottom Electrode

Self-Assembled Monolayers (SAMs) of alkanethiols have been deposited on a wide variety of substrates like mercury [64], iron [65], copper [66], GaAs [67], silver [68] and stainless steel [69]. The most commonly used substrate is (111)-oriented gold, on which the SAM is known to form a commensurate $(\sqrt{3} \times \sqrt{3})R30°$ overlayer [63]. The commensurability implies that every distortion in the gold surface inevitably distorts the structure of the overlying SAM. Therefore, a very high quality gold layer with a very low surface roughness is needed for the deposition of highly ordered monolayers of alkanethiols.

2.1 Growth of Thin Films

The deposition of a thin film starts with the arrival of single atoms at the surface. For growth from the gas phase, the arrival rate R is proportional to the vapor pressure p_{vp} of the deposited species above the substrate and inversely proportional to the temperature T of the evaporation source [70]:

$$R \propto \frac{p_{vp}}{\sqrt{2\pi mkT}} \tag{2.1}$$

with m: molecular weight of the deposited material, k: Boltzmann constant.

When they hit the surface, the atoms dissipate energy into the substrate and occupy a lower energy level than in the gas phase. The atoms are now adsorbed on the substrate, but can still move laterally on the surface. Although the atoms are localized in an energy minimum of the surface potential, they are able to hop from one energy minimum to the next one. This process is thermally activated and described by the diffusion coefficient

D [71, 72]:

$$D = \alpha \nu_0 N_0^{-1} \exp -\frac{E_d}{kT_s} \tag{2.2}$$

with N_0: substrate atomic density, α=0.25 for diffusion in two dimensions, ν_0: phonon frequency, E_d: energy barrier, T_s: temperature of substrate.

While moving over the surface, the adsorbed atoms or adatoms can either re-evaporate or they can eventually hit another adatom and form a dimer. Again, these dimers can be hit by an adatom resulting in the formation of a trimer and so forth. These accumulations of atoms (called nuclei) are not necessarily stable; thermodynamic arguments predict a critical nucleus size. For nuclei with a number of atoms below the critical size, dissolution of the nuclei is favorable, whereas clusters with more atoms than the critical size are stable and tend to grow.

The shape of the nuclei is determined by the balance of the crystal energy, the surface energies of the substrate and the film. If the surface energy of the substrate is higher than the sum of the surface energy of the film and the interface energy between film and substrate, the deposited material minimizes its energy by avoiding as much surface energy of the substrate as possible, i.e. it tries to wet the whole substrate. This results in flat nuclei (two dimensional), which gives this growth mode its name: two-dimensional growth mode[1].

In contrast to the two-dimensional growth mode, three-dimensional growth[2] occurs if the surface energy of the substrate is lower than the sum of the surface energy of the film and the interface energy between film and substrate. Then, the nuclei can save energy if they do not completely wet the substrate and form a continuous layer, but build drop like three dimensional islands. The contact angle ϕ of these islands (the angle between the substrate and the tangent of the surface of the drop at the contact point) is determined by Young's equation:

$$\gamma_{sub} = \gamma_{film} \cos\phi + \gamma_{int} \tag{2.3}$$

with γ_{sub}: surface energy of the substrate, γ_{film}: surface energy of the film and γ_{int}: interface energy between film and substrate.

After nucleation, the stable nuclei grow by incorporating more and more adatoms until different islands touch each other on the surface. At this point, the islands can either retain their shape and crystallographic orientation or they can merge and form a new, larger island with a single crystallographic orientation. The latter coalescence process predominantly occurs at high temperatures.

[1] Also called layer-by-layer growth or Frank van der Merwe growth.
[2] Also termed island or Volmer-Weber growth mode.

The growth of thin films is a rather complex process that consists of different steps with different dependencies on process variables like substrate temperature and deposition rate. This process can be treated quantitatively by the so-called Mean Field Theory. In the Mean Field Theory only the mean of all the characteristics of thin film growth is examined and all local variations are neglected. On the assumption that only monomers are mobile on the surface, the Mean Field Theory proposes the following set of differential equations [71–73]:

$$\frac{dn_1(t)}{dt} = R - \frac{n_1(t)}{\tau_d} - 2U_1 - \sum_{j>1}^{\infty} U_j \tag{2.4}$$

$$\frac{dn_i(t)}{dt} = U_{i-1} - U_i; \qquad i > 2 \tag{2.5}$$

with n_i: density of clusters containing i atoms, U_i: capture rates of clusters of size i, τ_d: desorption time of adatoms, R: deposition rate.

These equations can be easily understood. The density of adatoms (n_1) increases by the deposition rate (R) and decreases by re-evaporation ($\frac{n_1}{\tau_d}$), the formation of a dimer by two monomers ($2U_1$) and the incorporation of adatoms into clusters of i atoms (U_i). The density of clusters consisting of i-atoms increases by incorporating an extra atom into a cluster of $i-1$ atoms (U_{i-1}) and decreases by adding one atom to a cluster of i atoms (U_i).

For 3D growth and complete condensation (re-evaporation is negligible) the set of differential equations can be solved. It follows for the density of stable clusters n_s [73]:

$$n_s(R,T,i) \propto \left(\frac{R}{N_0\nu}\right)^{2i/(2i+5)} \times \exp\left(\frac{1}{k_BT}\frac{2}{2i+5}(E_i + iE_d)\right) \tag{2.6}$$

with N_0: areal density of absorption sites, ν: surface vibrational frequency, T: substrate temperature, i: size of the critical nucleus, E_i: formation energy of the critical nucleus, E_d: activation energy for surface diffusion.

If re-evaporation becomes relevant, equation (2.6) changes to [73]:

$$n_s(R,T,i) \propto \left(\frac{R}{N_0\nu}\right)^{2i/3} \times \exp\left(\frac{1}{3k_BT}(E_i + (i+1)E_a - E_d)\right) \tag{2.7}$$

Both equations reveal a dependency $n_s \propto R^p$ [73, 74] of the density of stable islands on the deposition rate and an arrhenius type dependency $n_s \propto \exp(E/(k_BT))$ of n_s on the temperature, i.e. the density of stable islands increases with increasing flux and decreases with temperature.

2.2 Deposition of Thin Films of (111)-Oriented Gold

There is a huge amount of literature on the topic of growth of thin films of gold [75–102]. Different factors such as the choice of substrate material, pretreatment of the substrate, deposition temperature, deposition rate and annealing conditions were identified to influence the morphology of a gold layer.

The influence of the substrate on the gold layer was for the first time investigated by Vancea [98]. Five different materials were examined: glass, silicon, NaCl, HOPG and mica. The films on glass and silicon showed a rough surface, whereas the films on NaCl and HOPG revealed a much smoother surface. The films on mica were not uniform: some parts of the surface were rough, but some were smooth. The growth of gold films on silicon was studied by various authors [80, 83, 84, 86, 87, 90, 101]. For example, Okamato [90] published some results on the deposition of gold films on silicon. He showed that atomic flat gold-terraces can be built on silicon without any special thermal treatment. However, these terraces were small (only 10nm in diameter) and some amount of silicon always diffuses into the gold layer [80, 83, 84].

In the majority of publications, mica was used as substrate for the deposition of gold. Mica, or more precisely muscovite ($KAl_2|(OH)_2|AlSi_3O_{10}|$), is a natural mineral. Most importantly, this material can be easily cleaved along the (001)-plane so that a very smooth and clean surface can be easily obtained.

In most publications, mica was heated in vacuum prior to depositing the gold layer. The influence of this heating procedure was examined by DeRose [76]. He stated that the roughness of gold films decreases exponentially with the duration of heating. The heating temperatures and heating durations vary significantly from author to author (200°C -500°C , 1h to several days).

The most important parameter for the growth of thin films is the deposition temperature. At all temperatures 3D growth of gold on mica is predominant. In accordance with equations (2.6) or (2.7), the density of islands decreases with increasing temperature. Films deposited at room temperature consist of small hills or islands, each around 7.5nm high and 50nm wide [75]. By increasing the deposition temperature, the size of the hills increases and the density of stable islands decreases [93][75]. DeRose et al. [76] examined the influence of the deposition temperature on the surface roughness and stated that the roughness decreases with higher temperatures.

Even though in most publications low deposition rates were used (0.05nm/s - 0.5nm/s), the experiments of Putnam et al. [93] showed a higher homogeneity and lower roughness with higher deposition rates (up to 16nm/s). Höpfner et al. [82] proposed a two step deposition process. In the first step, the gold film was deposited at high rates (2nm/s), whereas in the second step the deposition rate was drastically reduced (0.2nm/s). This process increased the homogeneity of the gold film.

Following the deposition process, the gold film is sometimes annealed. This annealing step has a similar effect on the film morphology to that of an increase in the deposition temperature [91]. Common temperatures are 500°C for several hours [76, 82, 95].

2.3 Slow Deposition of Gold on Mica

As in most publications, in the first experiments gold is deposited on mica at a low rate (0.1nm/s). To obtain gold films with low roughness these films are deposited at high temperatures: 464°C , 550°C and 610°C. The films are prepared in an e-gun evaporation chamber at a base pressure of $10^{-7}mbar$. Prior to deposition, mica[3] is freshly cleaved and heated in vacuum for 6h at the respective deposition temperature. After heating, 200nm of gold are deposited at the above mentioned temperatures. Following the deposition, the films are annealed for 1h at the deposition temperature.

The films are characterized by AFM and XRD measurements. XRD measurements confirm the (111)-orientation of the film. The AFM measurements are shown in figures 2.1(a)-2.3(a).

2.3.1 Results

In figure 2.1(a) the film morphology of gold films deposited at 464°C is shown. As already mentioned in the preceding section, the growth occurs in a 3D fashion, i.e. the surface consists of distinct hills or islands, each around $1\mu m$ in diameter. A few hills already seem to coalescence, but this process is not very pronounced and most hills are isolated from their neighbors. Some islands show a regular hexagonal shape, which is due to the (111)-orientation of the layer.

In figure 2.1(b), a linescan of figure 2.1(a) is shown. Deep trenches between two hills can be noticed. Sometimes, the depth of these trenches is in the range of the overall thickness of the gold layer (200nm). Consistent with these results is the observation that the films do not show any or only a very poor lateral electric conduction.

By raising the temperature to 550°C, the size of the hills increases to several micrometers (figure 2.2(a)). Furthermore, the coalescence process is more advanced than in the 464°C sample so that several clusters of islands have been formed. But there are still deep trenches between these clusters of islands, also visible in the linescan in figure 2.2(b). Again, the layers are not conducting.

To accelerate the coalescence process, the gold films are deposited at an even higher temperature (610°C) so that eventually all hills flow together and form a continuous, electrically conducting layer.

[3]Plano GmbH, Glimmer ULTRACLEAN, article no. G250-7

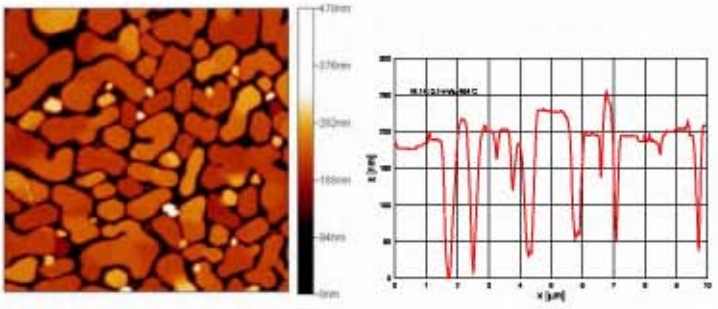

(a) Topography ($10 \times 10\mu m^2$). (b) Linescan.

Figure 2.1: 200nm gold on mica, deposited at a rate of 0.1nm/s at 464°C. The film consists of separated islands.

The surface of a gold film deposited at 610°C is shown in figure 2.3(a). In contrast to equations (2.6) and (2.7), the size of the hills decreases to approximately $1\mu m$. This contradiction to the theory could be due to a change in the properties of the substrate with increasing temperatures. To examine the behavior of mica at high temperatures the thermogravimetric measurement shown in figure 2.4 is taken. For this measurement, the mass loss of mica heated from room temperature to 750°C at a rate of 0.3K/min at reduced pressure (50mbar) is recorded. In figure 2.4 the mass loss in percent is plotted as a function of the heating temperature.

It can be seen that mica slowly loses mass at temperatures above 350°C. For higher temperatures(>600°C) the degradation of mica accelerates. This acceleration of decomposition is close to the deposition temperature of the gold film shown in figure 2.3(a). Therefore, the decrease in island size at temperatures above 600°C can be explained by the decomposition of mica at high temperatures.

2.3.2 Conclusion

The growth of thin films on mica is three-dimensional. The size of the gold islands is dependent on the deposition temperature. Whereas raising the temperature from 464°C to 550°C results in an increase in island diameter, at temperatures of above 600°C the mica substrate degrades and the island diameter decreases again. Due to very weak coalescence, at all temperatures the islands are not connected resulting in no electrical conduction of the layer. This observation agrees with the publication by Zheng et al. [102], who found a transition from continuous gold films on mica to discontinuous films

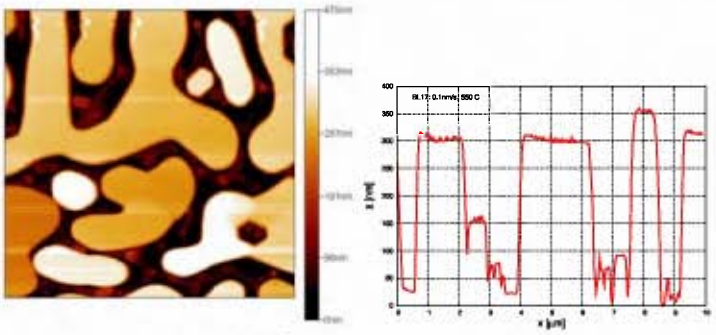

(a) Topography ($10 \times 10\mu m^2$). (b) Linescan.

Figure 2.2: 200nm gold on mica, deposited at a rate of 0.1nm/s at 550°C. By increasing the temperature, the islands size increases, but the film is still discontinous.

at elevated temperatures. Zheng et al. measured a transition temperature of about 540-570°C, which is higher than the lowest temperature used in this thesis (464°C). This discrepancy is most probably due to differences in the position where the temperature is measured. A temperature of 400°C as used in this thesis relates to the temperature which is measured directly on the substrate. This temperature correlates to a heater temperature of approximately 600°C.

Zheng et al. explained the development of discontinuous films by the interplay of high temperatures and low deposition rates. At high temperatures, the surface diffusion of the gold atoms is high leading to a low density of islands. Furthermore, if two islands grow together, they avoid interfacial energy between mica and gold by increasing in height, thereby decreasing the substrate coverage (e.g. see figures 2.1(b) and 2.2(b)).

2.4 Fast Deposition of Gold on Mica

The slow deposition process results in layers of gold which are not conducting so that these layers cannot be used as bottom electrodes. Furthermore, the characterization of these films by STM is impossible, which would be necessary to obtain atomic resolution. Zheng et al. [102] explained the growth of discontinuous gold films by the interplay of high temperatures and low deposition rates. By increasing the deposition rate, more stable islands will be formed so that the film is forced to become continuous. Therefore, it is tried to overcome this problem by using higher deposition rates. A film grown at a rate of 5nm/s at 550°C under otherwise unchanged deposition conditions is shown in figure 2.5. The difference to the layers deposited in the slow process is promising. No

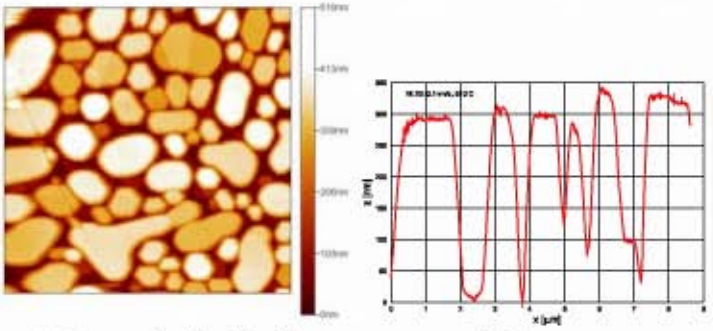

(a) Topography ($10 \times 10 \mu m^2$). (b) Linescan.

Figure 2.3: 200nm gold on mica, deposited at a rate of 0.1nm/s at 610°C. The decrease in island size is due to decomposition of the substrate material.

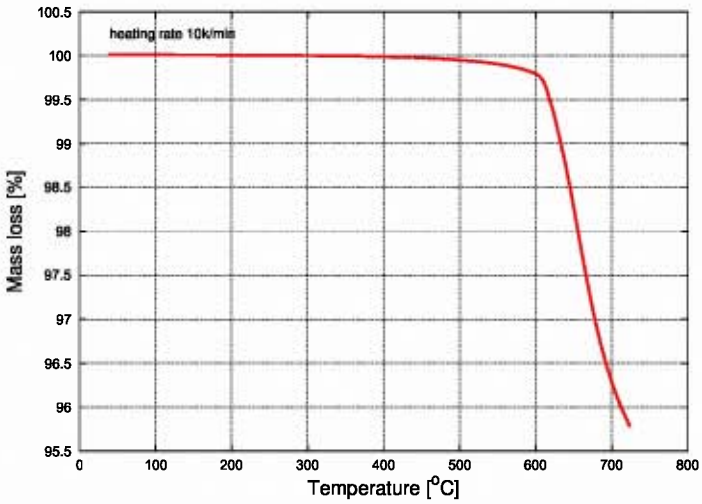

Figure 2.4: Thermogravimetric measurement of mica. Above 350°C a slow loss of mass is visible, which accelerates above 600°C.

hills can be seen, the growth mode changes from purely three dimensional to layer by layer growth. However, deep holes are seen in the gold films, which are most probably due to the fast deposition.

To fill these holes, the gold film is deposited in a two step process, similar to the experiments by Höpfner et al. |82|. In the first step, 150nm of gold is deposited at a rate of 5nm/s. This step is followed by the deposition of 50nm of Au at 0.05nm/s. Films are produced at three different temperatures: 400°C, 450°C, 550°C. Otherwise, the same parameters as for the gold layers of the preceding section are used: mica is freshly cleaved before transferring it into the vacuum chamber ($\sim 10^{-7} mbar$). In the vacuum chamber mica is heated at the deposition temperature for 6h. Following deposition, the gold films are annealed for 1h before they are cooled down slowly.

2.4.1 Characterization by AFM

In figure 2.6(a) an AFM scan of the gold layer deposited at 400°C by the two step process is shown. Again, as in the single step process with a high deposition rate, layer by layer growth is predominant, but in contrast to figure 2.5, the holes seen in the single step process have vanished. Gold terraces can be identified on the surface. Two kinds of step edges of the terraces are seen: rounded and straight step edges. The straight step edges are oriented along the $\langle 01\bar{1} \rangle$ directions. The overall roughness of the surface, defined as the rms-value of the height variation, is very low (2-3Å in an area of $25 \mu m^2$). A roughness in this range has only been reached for template-stripped gold films obtained by Wagner et al. [79, 99], which were prepared by a much more complex technique.

In the films deposited at 450°C (see figure 2.6(b)), deep cracks draw through the sample. The cracks are linear and run in the same directions as the lines already observed in the 400°C sample. Due to the cracks, the rms-value of the height variation rises to several nanometers.

At 550°C, the surface is similar to the 450°C sample (figure 2.6(c)). Again, there are linear cracks, running in the $\langle 01\bar{1} \rangle$ directions. However, although the 550°C sample is microscopically similar to the other samples, macroscopically the gold layer starts to flake off the mica substrate. Macroscopically, the layer is very rough, despite the fact that microscopically there are flat and smooth areas (roughness 6.5nm on $25 \mu m^2$).

Due to the change from 3D to 2D growth, all layers show electrical conduction, making STM measurements possible.

2.4.2 Characterization by STM

Different UHV-STM scans of a gold layer prepared at 400°C are shown in figure 2.7(a)-2.7(b). Similar to the AFM scans, large atomically flat gold terraces (100nm-300nm

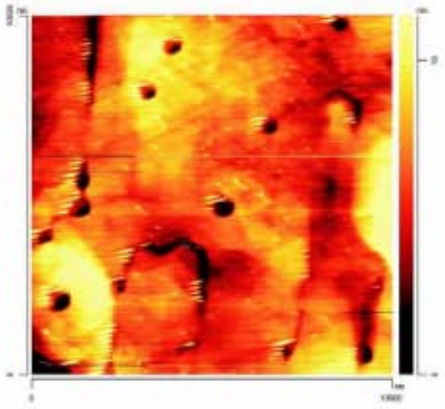

Figure 2.5: Gold film prepared at 550°C at an increased rate (5nm/s) ($10 \times 10 \mu m^2$). By increasing the deposition rate, the film becomes continuous, but there are deep holes (>20nm).

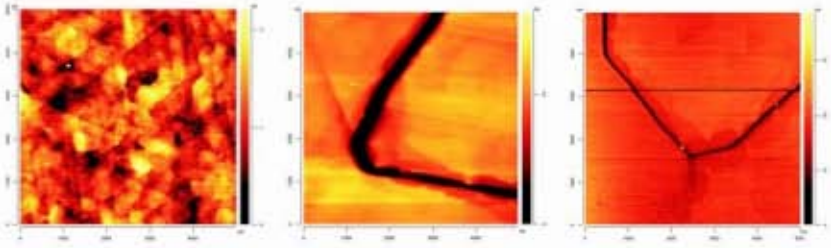

(a) AFM 400°C ($5 \times 5 \mu m^2$). (b) AFM 450°C ($5 \times 5 \mu m^2$). (c) AFM 550°C ($5 \times 5 \mu m^2$).

Figure 2.6: Gold film prepared at 400°C, 450°C and 550°C in the two step process. The holes seen in the single step process are filled. For temperatures above 400°C cracks form in the sample indicating high stress in the film.

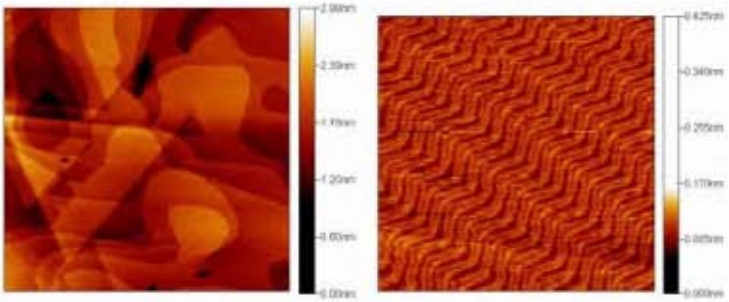

(a) 1x1μm^2. (b) 115x115nm^2.

Figure 2.7: STM scans of a film prepared at 400°C in the two step process. The gold terraces are seen in part (a). There are two kinds of step edges: rounded and straight step edges (facets). At higher magnification, the herringbone reconstruction of (111)-oriented gold is seen.

width) and two distinct structures can be seen: facets with linear step edges along the $\langle 01\bar{1} \rangle$ directions and structures with rounded step edges (see 2.7(a)). At a higher resolution as shown in figure 2.7(b), the so called herringbone reconstruction can be resolved (zig-zag lines in figure 2.7(b)), a famous and, due to its large size, probably unique surface reconstruction.

The Herringbone Reconstruction

Until 1973 the (111)-surface of gold was considered to be unreconstructed. For the first time, Perdereau et al. [103] found an anomalous diffraction structure by studying the deposition of lead onto (111)- oriented gold by Low Energy Electron Diffraction (LEED), and interpreted it as a reconstruction of the top layer of the clean gold surface. Later, this finding was confirmed by further LEED [104], Transmission Electron Microscopy (TEM) studies [105–108] and High-Resolution Helium-Atom Diffraction [109]. Real space information on the surface structure was for the first time obtained by STM studies [110, 111].

From these studies, a consistent picture emerged. The reconstruction is formed by squeezing 24 surface gold atoms into 23 bulk lattice sites leading to a 4.4% contraction along the $[1\bar{1}0]$ direction. Therefore, the reconstruction can be described by a $(\sqrt{3} \times 23)$ rect unit cell. Due to the contraction, the surface atoms have to periodically change from fcc- to hcp-stacking. The resulting model of the surface atoms is shown in figure 2.8. The positions of the surface atoms are shown with respect to the atoms in the second layer. Open circles represent surface atoms, and crosses indicate atoms in the second layer. In

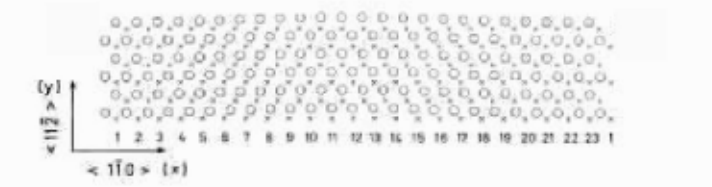

Figure 2.8: Schematic of the $(\sqrt{3} \times 23)$rect herringbone reconstruction [109]. The reconstruction is formed by a 4.4% contraction along the $[1\bar{1}0]$ direction and a periodic change from fcc- to hcp- stacking.

the left and right part of the image, the uppermost atoms are fcc terminated (region C), whereas in the middle the surface atoms are hcp terminated (region A). Between the different regions, there is a certain transition zone. Whereas in early LEED studies a uniform contraction along the $[1\bar{1}0]$ direction and therefore a smooth transition between these regions [104] was proposed, in TEM studies a sharp transition was postulated [105]. Helium diffraction studies revealed that the most probable structure is a mixture of these extremes: The transition between A and C regions is gradual, but the compression of the surface atoms is not uniform [109]. These studies also revealed that the hcp-regions are smaller than the fcc, which reflects the energetic preference of fcc compared to hcp stacking. With this model, a surface height modulation of about 0.015nm was proposed (see top of figure 2.8), which was later confirmed by STM studies [110, 111]. With STM, an additional superstructure was discovered [111]: This superstructure is apparent by zig-zag lines as seen in figure 2.7(b). These zig-zag lines represent different rotational domains of the same $(\sqrt{3} \times 23)$rect unit cell. It is this large range superstructure which finally gave the herringbone structure its name.

The Origin of Faceting

One significant feature of the gold films, which has already been described in the discussion of figure 2.6(a) and 2.7(a), is the three sets of straight lines in the three equivalent $\langle 01\bar{1} \rangle$ directions. This phenomenon is known as faceting in literature, and several possible explanations for this structure have been proposed [76]. It is argued that the facets are formed during the deposition process as a consequence of the (111)-orientation of the film. Another explanation is that faceting is caused by stacking faults in the gold film due to steps of the freshly cleaved mica. Other authors suggest that the facets are induced by stress caused by the STM or AFM tip, which is relaxed in linear steps.

None of these explanations can fully explain the experimental observations. The facets cannot be created during the deposition process (as in the first two propositions),

since the rounded step edges grow over the linear facets and are not influenced by them (see figure 2.7(a)). This indicates that the facets emerge after the round terraces have been formed during deposition. Consequently, the linear steps have to be formed during annealing or during cooling down from the deposition temperature (400°C) to room temperature. Likewise, stress induced by the STM or AFM tip should always result in facets in the scan direction and not in all three $\langle 01\bar{1} \rangle$ directions.

More recently Shimoni et al. [112] have shown that facets or straight step edges can be generated by electromigration. However, relatively large currents are needed for this mechanism (50-500mA, 104-105 Acm^{-2}), whereas for the STM measurements in this work only small currents are passed through the sample (<1nA, $10^{-4}Acm^{-2}$). These small tunnel currents do not change the surface topography and do not generate surface steps in the experiments, consistent with the results of Shimoni et al. [112], who state that STM measurements with a typical tunneling resistance of 200MΩ do not affect the surface dynamics of atoms in the gold film.

Here, an alternative explanation is put forward. As already discussed, the rounded step edges coexist with the linear facets. This indicates that the facets are built after the round terraces have been formed, most probably during annealing or during cooling down after deposition.

To verify this hypothesis, a gold film is successively heated in vacuum (10^{-9}mbar) for 45min at 410°C, 470°C and 520°C. After each heating step, the film is examined by UHV-STM at room temperature. In figure 2.9(a)-2.9(d), representative scans of the surfaces are shown. In the freshly deposited sample, the rounded structure dominates, and after annealing the number of facets rises dramatically. At the bottom of figure 2.9(c), it can be seen that several facets group together and form a deep trench. This process correlates to the deep trenches seen in in gold films deposited in the two step process at 450°C and 550°C (see figure 2.6(b) and 2.6(c)). These trenches indicate high stress in the samples.

This stress in the gold film most probably originates from the gold/mica interface and is caused by cooling down from elevated temperatures to room temperature and slightly different coefficients of thermal expansion. This stress created at the interface can be released by a glide along (100)-planes in the $\langle 011 \rangle$ direction (see figure 2.10(a) and 2.10(b)), similar to the relaxation of stress in thin layers of PbSe [113] and in flame annealed gold films on glass induced by electromigration [112]. The consequence of this gliding mechanism is facets with minimal step heights $h_{min} = 0.24$ nm elongated along the $\langle 011 \rangle$ directions. Due to geometrical considerations, the mean distance between two facets λ necessary to relieve strain ϵ can be estimated as [113]:

$$\lambda = \frac{3}{2} \frac{|b| \sin(\theta)}{\epsilon} \frac{h}{h_{min}} \tag{2.8}$$

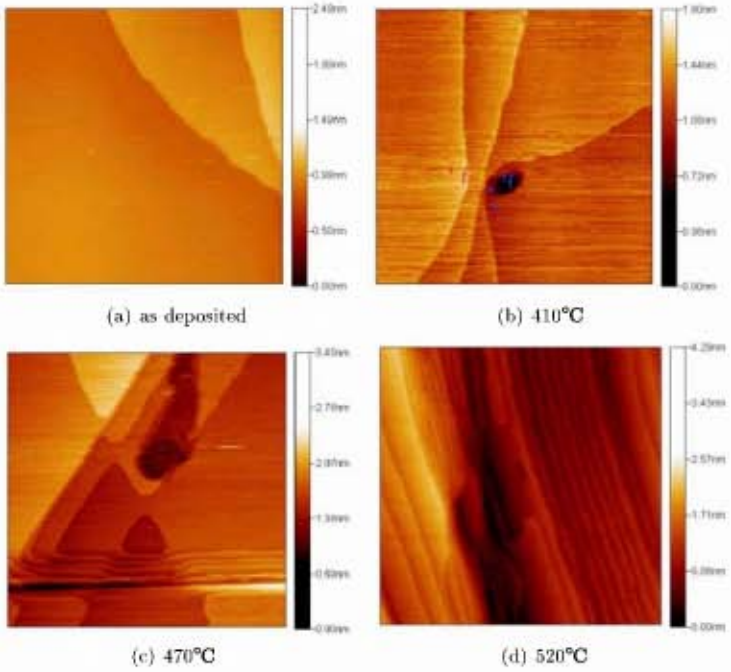

(a) as deposited (b) 410°C

(c) 470°C (d) 520°C

Figure 2.9: STM scans of a gold film, prepared at 400°C in the two step process, which is afterwards heated to 410°C (b), 470°C (c) and 520°C (c) in UHV. The size of all images is $200 \times 200nm$. This additional heating step increases the number of facets.

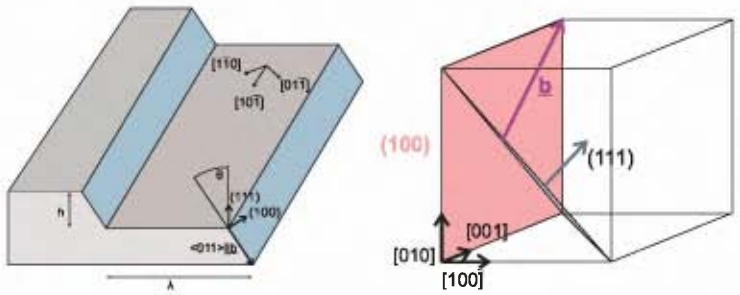

Figure 2.10: Surface steps resulting from a glide along (100)-glide planes (a) and burgers vector and orientation of (100) glide plane in an fcc unit cell (b).

with $\underline{b}$: Burgers vector ($\underline{b} = \frac{1}{2} < 011 >$), θ : angle between the surface normal of the (111)-plane and $\underline{b}$, h : mean step height and h_{min} : minimal step height (0.24nm).

At 400°C the stress is mainly due to the different thermal coefficients of expansion of mica and gold ($10\times\ 10^{-6}/°C$ for mica (200°C), parallel to the cleavage plane; $14.1\ \times\ 10^{-6}/°C$ for gold [114]). Using equation (2.8), one can estimate a mean distance between parallel linear steps of 170nm for the given coefficients of expansion. Taking figure 2.7(a), one can count 2-3 steps in each of the $\langle 01\bar{1} \rangle$ directions, corresponding to a distance between facets of approximately 350nm to 500nm (some of the steps are two lattice constants high, therefore they have to be counted twice). The difference between the calculated and measured mean distance between the linear steps could be caused by the uncertainty in the coefficient of expansion of mica. Furthermore, equation (2.8) is only a lower bound of the mean distance between facets, because it does not involve any energetic considerations and does not involve stress released by other mechanisms. The formation of facets involves an increase in surface energy due to additional step edges. This could lead to a situation where the stress is only partially released by this mechanism, because the energy gain from the relaxation in the bulk cannot compensate the necessary energy to form additional surface steps.

As an additional source of strain, mica is known to decompose at higher temperatures [76], as already seen in figure 2.4. This leads to the conclusion that, at higher temperatures, the decomposition of mica adds further stress to the sample and therefore, even more facets are formed. In particular, the more than linear increase in the density of facets in figure 2.9(c) and 2.9(d) can be attributed to the change in mica.

2.5 Conclusion

The growth of gold on mica has been studied. For low deposition rates, the films are discontinuous and show only a very poor conductivity. Continuous layers of gold are produced by increasing the deposition rate. This high deposition rate leads to holes in the films so that a second slow deposition step has been introduced, which fills these holes.

This two step deposition procedure leads to very smooth gold films with large terraces, as needed for the characterization of SAMs on gold by STM. Two structures of the terrace edges can be seen: rounded step edges and linear step edges along the $\langle 01\bar{1} \rangle$ directions (faceting). A new explanation of the hexagonal faceting of gold films on mica is put forward in this thesis. The facets coexist with a rounded structure, indicating that these two structures must have different origins. Furthermore, the rounded structure is not influenced by the facets, which shows that the facets are built after the rounded structure is formed. By annealing the sample over 450°C the number of facets rises so that it can be concluded that the facets are not due to a rearrangement of rounded structures. With increasing temperature, more and more facets arise and finally form deep cracks, which suggests that the facets are induced by strong stress in the film. It is shown that up to 400°C the stress originating at the gold/mica interface caused by the different coefficients of thermal expansion of mica and gold is appropriate to explain the formation of facets due to stress release by a glide along the (100)-glide plane. At higher temperatures, disintegration of mica causes a change in the surface morphology, which adds further stress to the gold, resulting in a more than linear increase in faceting and deep trenches in the sample.

Chapter 3

Characterization of Self-Assembled Monolayers of Alkanethiols on Gold

Thiol-based self-assembled monolayers (SAMs) of organic molecules are an effective tool for tailoring the surface properties of metals [63, 115]. The applications of SAMs range from wetting control [116–119], corrosion inhibition [120], protein adsorption [121], and lateral structuring [122] to molecular electronics [23]. In this thesis, alkanethiol SAMs are used as host matrices in which electrically active molecules are embedded. For this application, special demands are imposed on the layers: they have to possess a low defect density, large molecular domains and they have to be very clean. To be able to distinguish between the embedded molecules and the surrounding alkanethiol SAM, the structure of the SAM has to be studied in detail. The preparation and characterization of SAMs of alkanethiols is described in the following chapter.

3.1 The History of SAMs of Alkanethiols on Gold

Even in the 1930s, it was possible to produce organic monolayers using the methods invented by Langmuir and Blodgett [123, 124]. This method consists of the assembly of amphiphilic molecules on the surface of a liquid and the transfer of this monolayer onto a solid substrate. Later research focused on methods that assemble monolayers of molecules directly onto a solid substrate. Several material systems were found that showed this behavior; the most popular are organosilicon derivatives (silanes) on oxidic surfaces and organosulfur compounds on gold.

Monolayers of silanes were discovered by Polymeropoulos and Sagiv [61] in 1978. For this material class the term self-assembled (or assembling) monolayer was first used by an anonymous author in a short article in New Scientist [125].

Later, Nuzzo and Allara [62] and Li et al. [126, 127] independently discovered monolayers of molecules bound via sulfur-gold bonds onto a gold substrate. Whereas

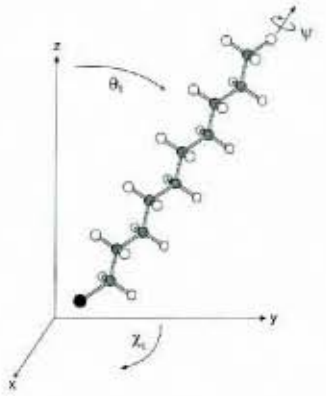

Figure 3.1: The conformation of dodecanethiol on gold [63] is shown. The molecules bind with the sulfur head group onto gold and the molecular axis is tilted by $\Theta_m = 32.5°$ at an angle of $\chi = 13.8°$ away from the NN direction [131]. The molecular backbone is twisted by $\Phi_t = 55°$.

Li et al. did not further examine the properties of the monolayer and used the film only for binding and separating electroactive molecules onto several metals including gold, Nuzzo et al. conducted most of the early experiments to elucidate the structure of this new class of monolayer. At first, the experiments concentrated on disulfides and in particular on dialkyl-disulfide (H_3C-$(CH_2)_{n-1}$-S-S-$(CH_2)_{n-1}$-CH_3) on gold. By means of ellipsometry [62, 128, 129], infrared spectroscopy [62, 128], X-Ray Photoelectron Spectroscopy (XPS), temperature-programmed desorption (TPD) and high-resolution Electron Energy Loss Spectroscopy (EELS) [130] it was found that the disulfide bond is dissociated and the remaining sulfur atoms are bound onto the gold substrate. Even at this very early stage of research, Nuzzo et al. hypothesised that the molecules adsorb at the threefold hollow sites of the gold lattice thereby forming a $\left(\sqrt{3} \times \sqrt{3}\right) R30°$ hexagonal overlayer [130]. Vertically, the alkane chain is directed almost upright on the sample, with a tilt Θ_m of 37° out of the surface normal and a twist Φ_t of 55° around the molecular backbone (see fig. 3.1) [128]. Thereby, a highly ordered and dense monolayer was formed.

Following these studies, the structure of alkane (mono)-thiols (HS-$(CH_2)_{n-1}CH_3$)was found to reassemble the structure of the disulfides [132 134]. However, the adsorption of monothiols involves breaking of an S-H bond instead of the dissociation of the S-S bond, leading to different adsorption kinetics [133]. The exact values of the molecular tilt angle Θ_m, twist angle Φ_t and twist angle of the molecular backbone around the

(a) α-phase (b) β-phase (c) γ-phase (d) δ-phase (e) ϵ-phase

Figure 3.2: (a) to (e) show different phases of the c(4x2) unit cell. Small circles represent gold atoms, and large circle adsorption sites of dodecanethiol. Gray shaded molecules appear lower in STM images.

surface normal (relative to the nearest-neighbor(NN) direction) χ were determined in a grazing incidence x-ray diffraction study for various alkane chain lengths [131].

The lateral structure was further clarified by electron diffraction [135] and low energy helium diffraction [136, 137]. These studies confirmed the hexagonal $\left(\sqrt{3} \times \sqrt{3}\right) R30°$ structure[1].

In 1990, Nuzzo et al. published the first indications that the $(\sqrt{3} \times \sqrt{3})R30°$ hexagonal lattice of alkanethiols has a further superstructure with two inequivalent molecules per unit cell [139]. In analogy to bulk phases of alkanethiols, they proposed that the superstructure is formed by different twist angles for the two inequivalent molecules. By means of low energy helium diffraction, Camillone et al. determined the unit cell of this reconstruction to be $c(4 \times 2)$ or equivalently $3 \times 2\sqrt{3}$ [140].

Scanning Probe Methods proved to be enormously powerful for the characterization of SAMs. The first molecularly resolved STM study of an alkanethiol monolayer was published in 1991 [141], followed by an AFM study in 1992 [142]. In both studies, the $(\sqrt{3} \times \sqrt{3})R30°$ lattice was resolved. In 1994, Poirier et al. [143] and Delamarche et al. [144] simultaneously resolved the c(4x2) superstructure in their STM scans. High resolution images showed for the first time real-space information on the arrangement of the molecules in the unit cell.

In STM measurements, the inequivalent molecules in the c(4x2) unit cell differ in their apparent height. Different arrangements of apparently higher and lower molecules are described in literature [144–147] denoted as phase α to ϵ (see figure 3.2). The α-phase is the normal $\left(\sqrt{3} \times \sqrt{3}\right) R30°$ structure without any superlattice, whereas the β [144, 145], γ [145] and δ [143–145, 147] phases consist of molecules with two different heights. More recently, a c(4x2) structure with as many as three different molecular heights was discovered in octanethiol (C8) and dodecanethiol (C12) SAMs (ϵ-phase)

[1] In their original publication [135], Strong and Whiteside proposed an 8×8 structure. However, a reinterpretation of their data [138] showed that their diffraction pattern is also consistent with the $\left(\sqrt{3} \times \sqrt{3}\right) R30°$ structure.

[146, 147].

The height difference in STM images is believed to be due to different conformations of the molecule. Since the molecular backbone is tilted approximately 30° out of the surface normal, the terminal methyl group appears higher or lower if the molecule is twisted. For a full rotation, a maximum height difference of 0.6-0.7Å is expected [140, 144].

Similarly, different bonding sites of the sulfur head group on the gold surface, as proposed by grazing incidence X-ray diffraction [148], sum frequency generation [149], the X-ray standing wave technique [150] and high resolution electron-energy-loss spectroscopy [151] would lead to different heights in STM images. Different bonding sites cause the tunneling conditions to vary, which leads to the contrast between different molecules in the unit cell. For example Fenter et al. [148] propose that the sulfur head group dimerizes, resulting in an S-S spacing of 2Å and two inequivalent bonding sites (three fold hollow site and Au bridge site). They argue that the height modulation in STM images is due to both the inequivalent bonding site, resulting in different tunneling conditions, and different twists of the hydrocarbon chains about the chain axis.

After the high-density full coverage phase had been fully characterized, a new, lower coverage phase was found by Camillone et al. [152]. In contrast to the c(4x2) phase, in the new phase the molecules are not directed almost perpendicularly to the substrate, but lie flat on the surface so that this phase is called the lying-down phase. It can be described as a $(p \times \sqrt{3})$ structure, with p being a chain length and deposition parameter dependent constant. This phase can be generated through gas phase deposition at low exposures [153, 154] or by annealing a full coverage c(4x2) layer [152].

In the following, based on the literature described above, SAMs of dodecanethiol are characterized in detail by UHV-STM and optimized in terms of the quality of the films.

3.2 Experimental Details

For the characterization of the SAMs, molecular resolution is needed, which imposes high demands on the careful preparation and imaging of the samples. In the course of this thesis, the following factors have proved to be important.

Gold Substrates

The preparation of the gold substrates is described in detail in chapter 2. The two step deposition process is used for all following experiments. The substrates are always freshly prepared and used within one week after removal from the deposition chamber to minimize contamination.

Preparation of the SAMs

There are two ways of preparing SAMs, that are used in this thesis: deposition from solution and deposition from the gas phase. For deposition from solution, a clean gold sample is immersed into a highly diluted (1mM) ethanolic solution of the alkanethiol. Deposition is rather fast with a monolayer already being built after a few minutes [133]. To ensure that the film reaches equilibrium, the samples are kept in solution for several hours (typical immersion times are 12-24h). After deposition, the samples are thoroughly cleaned by pure ethanol to wash away physisorbed thiols.

Also employed in this thesis is deposition from the gas phase. For this kind of deposition, a UHV system with a base pressure of 10^{-7}mbar has been designed. This system consists of two chambers, one deposition chamber, in which the SAM is deposited onto the gold sample, and one evaporation chamber, in which the alkanethiols are evaporated. The evaporated alkanethiols are directed via a valve and a nozzle from the evaporation chamber towards the gold surface in the deposition chamber. The amount of molecules that hit the surface is controlled via the valve and the pressure in the deposition chamber.

STM Scanning Environment

The first STM scans have been done in air with a JEOL JSPM-5200 Environmental Scanning Probe Microscope. However, imaging SAMs with high resolution in air is rather difficult due to the contamination of the surface. The image quality is greatly improved by scanning with a JEOL JSPM-4500 Ultrahigh Vacuum - STM (base pressure 5×10^{-10}mbar). All STM scans are performed in constant current mode.

STM Tip Preparation

Probably the most important factor for the scan quality is the preparation of the STM tip. For the first experiments, tips made by cutting a platinum wire with a edge cutter have been employed. However, tips of this kind limit the resolution of the STM scan and are highly irreproducible. In contrast to cut platinum wires, etched wires of tungsten have a much lower tip radius and are more reproducible. The optimization of the preparation of the tungsten tips was examined in detail by Müller-Meskamp [155]. The preparation consists of etching a tungsten wire at the surface of an electrolyte (NaOH) with a dc voltage applied. At the surface of the electrolyte, the wire diameter is thinned until the wire breaks and the lower part of the wire drops down. This breaking of the wire causes a drop in etching current. This drop is detected by an etch controller, which stops the etching process immediately (switching time of $45ns$). The tip radius is directly related to fast off switching [156, 157]. For details of the etch controller and

tip preparation the reader is referred to [155].

Scan Parameters

Due to the highly insulating character and the mechanical softness of alkanethiol films, the STM parameters (tunneling voltage and current) have to be carefully chosen. In the first STM study of alkanethiol SAMs by Widrig et al. [141], the film was imaged with a very low tunneling impedance of $100M\Omega$ (200mV and 2nA). Consequently, the tip was believed to push into the film so that imaging results from tunneling between the tip and the Au-bond sulfur atoms. Later, by increasing the tunneling gap ($3G\Omega$ in [143] and $400M\Omega$ in [144]), Poirier and Delamarche greatly improved the resolution so that additional details of the c(4x2) superstructure could be resolved. This increase in quality was explained by the tip scanning above the SAM.

Following these publications, in this study the tunneling gap is chosen to be around $40G\Omega$ (2V, 50pA) to ensure that the tip does not penetrate the molecular layer. This tunneling impedance is the highest possible since higher voltages result in damage to the film and lower currents are not possible due to the noise level of the STM.

3.3 SAMs Grown from Solution

Due to the ease of preparation, in the first experiments the SAMs are assembled from solution. A representative scan is shown in figure 3.3(a) and 3.3(b). The SAM consists of a layer of dodecanethiol (C12), assembled from a 1mM solution for 20h45. Scanning is done at a tunneling voltage of 2V and a tunneling current of 50pA.

Figure 3.3(a) shows one terrace of the gold substrate covered by C12. Different domains of the C12 molecules are clearly visible, each domain being separated by a boundary which appears lower in the STM scan (white arrow). The domains have a size of approximately $50nm - 100nm$ and show a distinct stripe pattern. Three different orientations of the domains are visible according to the directions of the stripes, each orientation differing by an angle of 60°. Preferably along the domain boundaries, there are small black holes in the film. These black holes are approximately one gold layer deep (0.24nm), which points towards vacancy islands in the underlying gold, which are also covered by the C12 layer.

These results are consistent with the results of Poirier et al. [143], who showed that SAMs of short chain alkanethiols ($HS\text{-}(CH_2)_{n-1}CH_3$, Cn, n=4,6,8,10) build domains with domain size diameters between 5 and 15nm. They observed two types of domain boundaries: rotational boundaries and antiphase boundaries. Rotational boundaries are also seen in figure 3.3(a). The two unit cells of two adjacent domains are marked in the middle of the image, indicating the 60° twist between the two domains.

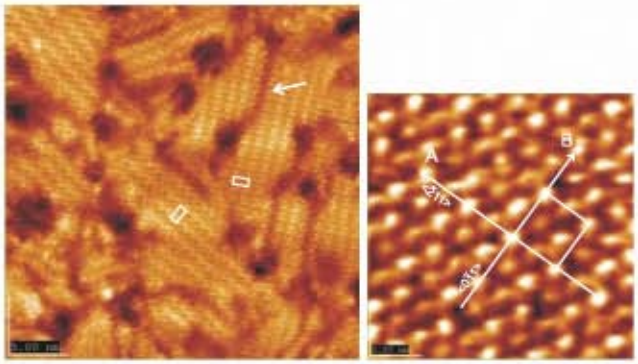

(a) $30 \times 30nm^2$

(b) $5 \times 5nm^2$

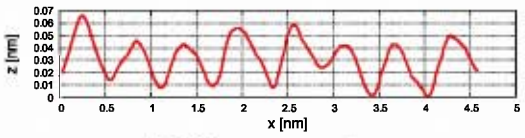

(c) NN or $\langle \bar{2}11 \rangle$ direction

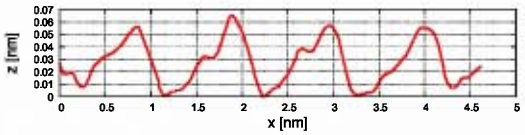

(d) NNN or $\langle 0\bar{1}1 \rangle$ direction

Figure 3.3: STM scan of a C12 SAM ($V_t = 2V, I_t = 50pA$). (a) shows a $30 \times 30nm^2$ scan of one terrace of the C12 covered gold surface. Different domains of the monolayer are seen. The domains are separated by boundaries appearing as dark lines. In (b) a high resolution scan is shown, displaying the delta phase of the c(4x2) unit cell. (c) and (d) show cross sections along line A (NN direction) and B (NNN direction), respectively.

These holes or vacancy islands were also observed in early STM studies of alkanethiol SAMs [158 166]. The pits were first interpreted as defects in the alkanethiol layer [165, 166] or as areas with an increased disorder in the film [165, 166]. Several experimental results questioned this interpretation. As in figure 3.3(a), the depth of the holes equals one gold terrace height (0.24nm) [164] and is independent of the alkane chain length and the imaging parameters (i.e. even if the tip penetrates the alkanethiol monolayer) [159, 161]. Furthermore, using high impedance STM, it was shown that the bottom of the holes is also covered with alkanethiols [160]. Therefore, it was concluded that the holes are one layer deep vacancy islands in the underlying gold substrate and not in the alkanethiol layer [160].

The widely accepted model for the mechanism of vacancy formation was proposed by Poirier [167]. He studied the growth of SAMs on reconstructed Au(111) from the gas phase and was able to show that the herringbone reconstruction is lifted during the growth of the monolayer. He showed that during lifting of the reconstruction two gold atoms per $(\sqrt{3} \times 23)$rect unit cell instead of only one are expelled from the surface. Thereby, gold vacancies are formed that can migrate and coalescence to vacancy islands as seen in figure 3.3(a).

Figure 3.3(b) shows a high resolution scan of a single domain. Individual molecules can be seen as protrusions. Cross sections along the NN- and NNN-directions are shown in figure 3.3(c) and 3.3(d). An exact analysis yields a slightly distorted hexagonal lattice with lattice constants of 0.57nm and 0.5nm. These lattice constants agree within the error of the STM with the $(\sqrt{3} \times \sqrt{3})R30°$ structure. A closer inspection also shows that some molecules appear higher and some lower and form the delta phase of the c(4x2) superstructure shown in figure 3.2(d). From the high resolution scan, the stripes in the large area scan can be explained as lines of molecules appearing higher running along the NNN-direction.

3.3.1 Thermal Annealing of SAMs Grown From Solution

Solution-based growth at room temperature resulted in films with small domain sizes ($50nm - 100nm$) and a high density of vacancy islands. To increase the quality of the films, they are annealed at elevated temperatures. Such an annealing step was shown to increase the domain size and to reduce the density of vacancy islands by a grazing incidence x-ray diffraction [131] and an STM study [168]. Annealing in air results in partial desorption and missing row patterns [168] so that for the following experiments the films are annealed in an ethanolic solution of dodecanethiol, similar to the procedure described by Bumm et al. [169].

The dodecanethiol (C12) films are produced as described in section 3.2. Following the normal room temperature deposition step, the films are annealed in a solution of

C12 at 50°C for 1h, at 78°C for 1h and at 78°C for 6.5h. The results are shown in figure 3.4(a)-3.4(c).

Compared to figure 3.3(a), the morphology of the SAM annealed at 50°C shown in figure 3.4(a) has not changed. The film consists of several domains, each domain having a diameter of approximately 5-15nm. At the domain boundaries, many small vacancy islands have formed.

In contrast to the film annealed at 50°C, annealing at 78°C has a higher impact on the film. The domain boundaries are more pronounced and the reconstruction lines of the c(4x2) structure are now clearly visible. Most important, the diameter of the domains increases to about 15-25nm, and the number of vacancy islands decreases. An exact analysis of the vacancy diameter is shown in the histogram in figure 3.4(d). The distribution of the vacancy diameter for figure 3.4(a) and 3.4(b) is shown in red and blue. It can be seen that the number of vacancies decreases (from 64 to 21), but the diameter increases (mean diameter for the 50°C sample 3.1nm and for the 78°C sample 4.7nm). Combining these two processes, annealing at 78°C results in a small decrease in the area of the sample covered with vacancy islands of approximately 20%. This observation can be explained by the Ostwald ripening mechanism proposed by Cavalleri et al. [158]. They observed a power law dependency of the radius r of the vacancy islands on the annealing time t: $r \propto t^{0.52}$. This behavior is explained by the detachment of monovacancies from smaller holes and intralayer diffusion of these monovacancies toward larger holes so that larger holes grow at the expense of smaller ones. Furthermore, at higher temperatures, some vacancy islands diffuse towards the gold step edges and annihilate there [159], which explains the decrease in area occupied by vacancy islands.

For longer annealing times (6.5h at 78°C), a new structure forms (figure 3.4(c)). This new structure coexists with domains of the full coverage structure and is characterized by a stripe pattern and a lower height compared to the standing-up c(4x2) domains. These observations point toward a lower coverage lying-down phase similar to the phase described by Camillone et al. [152]. Therefore, for longer annealing times desorption of C12 molecules becomes important. Different periodicities of the stripe pattern of the lying-down phase exist on the surface, indicating domains of different sub-monolayer coverage and suggesting that these structures are kinetically trapped rather than in thermodynamic equilibrium.

The distribution of vacancy islands is shown in figure 3.4(d) in black. As already observed for annealing at shorter times, the island diameter increases to 6.5nm. In contrast to the results obtained for shorter annealing times, the density of vacancies does not decrease and consequently the area of the sample, which is covered by vacancy islands, increases. Obviously, during the desorption of the molecules, additional gold

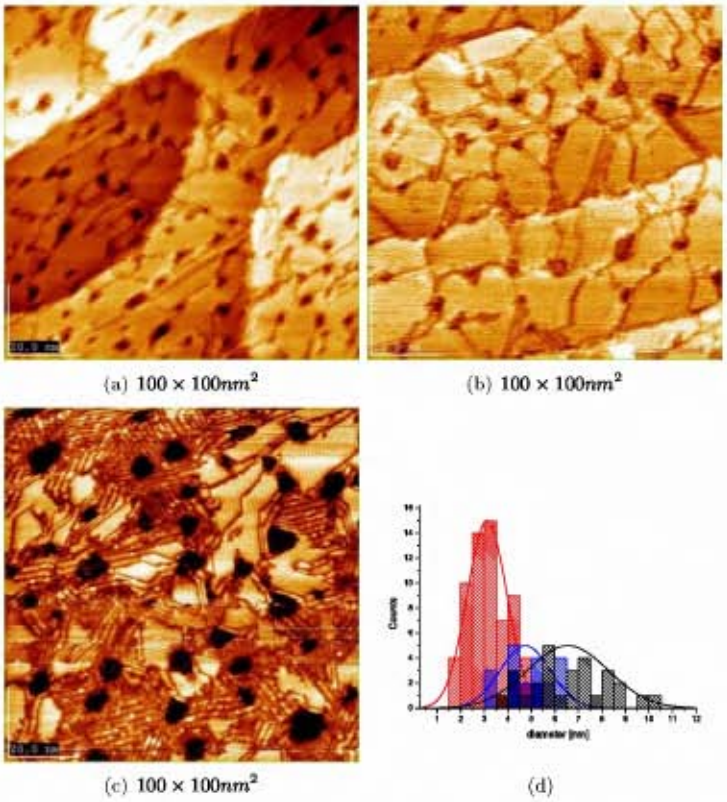

(a) $100 \times 100nm^2$ (b) $100 \times 100nm^2$

(c) $100 \times 100nm^2$ (d)

Figure 3.4: SAM of dodecanethiol annealed in solution at 50°C for 1h (a), at 78°C for 1h (b) and for 6.5h at the same temperature (c). In (d) the histogram of the radius of vacancy islands is shown. Whereas annealing at 50°C has no impact on the film, annealing at 78°C for 1h increases the domain size and reduces the area covered by vacancy islands. For longer annealing times, lying-down phases appear.

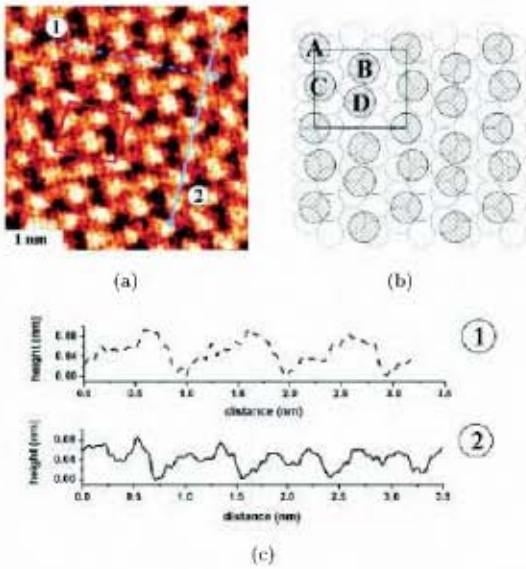

Figure 3.5: (a) Full coverage structure of the sample annealed at 78°C for 6.5h [170]. Deviations from the normal c(4x2) structure are visible, which lead to the structure shown in (b). In (c) cross sections along line 1 and 2 are shown.

atoms are expelled from the surface, leading to an increase in holes in the sample surface.

A closer inspection of the full coverage standing-up phase reveals some interesting deviations from the normal c(4x2) structure (see figure 3.5(a)), which are described in the publication by Müller-Meskamp et al. [170]. The modified structure of figure 3.5(a) has the same unit cell (8.5 ± 0.1Å$\times 10 \pm 0.1$Å) and the same packing density ($0.216 nm^2$ per molecule) as the c(4x2) structure. However, for the c(4x2) phase it is assumed that the thiols are bound to the threefold hollow sites of the gold lattice, which cannot explain the arrangement of the molecules in figure 3.5(a). Thus, a new molecular arrangement is proposed in figure 3.5(b). The corner molecules (A) are positioned on threefold hollow sites at the same positions as in the c(4x2) structure. To match the observed lattice, two of the center molecules are placed on a bridge (B) and a half bridge (C) position, respectively. Molecule D is on a different threefold hollow position. If A is on a hexagonal close-packed site, then D is on a face-centered cubic site and vice versa. Considering, that desorption is pronounced in this sample, the surface arrangement described here is most probably a kinetically trapped phase close to desorption.

In conclusion, solution-based growth results in SAMs that consist of many small domains and vacancy islands. The size of the domains can be increased and the density

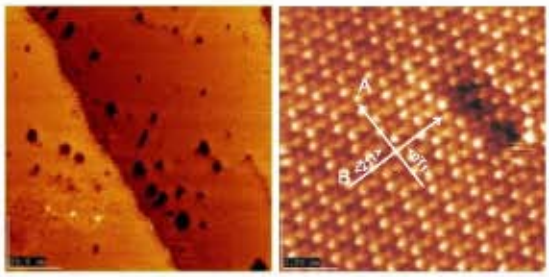

(a) $100 \times 100nm^2$ (b) $10 \times 10nm^2$

(c) NNN or $\langle 0\bar{1}1 \rangle$ direction

(d) NN or $\langle \bar{2}11 \rangle$ direction

Figure 3.6: A large area scan ($100 \times 100nm^2$) of a dodecanthiol SAM grown by vapor phase deposition is shown in (a). A higher resolution reveals the δ-phase of the $c(4x2)$ structure (b). (c) and (d) show cross sections along line A (NNN-direction) and line B (NN-direction) respectively.

of vacancy islands be decreased by an additional annealing step at 78°C for 1h. Longer annealing times result in desorption of C12 molecules and the appearance of lower coverage phases (lying-down phases). By this desorption process, gold atoms are also expelled from the surface so that the area which is covered by vacancy islands increases again. Furthermore, the high coverage phase of the sample annealed for a long time shows slight deviations in the molecular arrangement compared to the c(4x2) phase.

3.4 SAMs Grown from the Gas Phase

By thermal annealing of solution-grown SAMs, the diameter of the domains can be increased and the density of the vacancy islands be decreased, but the diameter of the domains still remains below 25nm. As is shown in this section, gas phase growth of SAMs increases the quality of the films substantially.

A large area scan of a dodecanethiol SAM grown by vapor phase deposition is shown in figure 3.6(a). The film is grown at a pressure of the C12 vapor in the deposition chamber of $\mathbf{2 \times 10^{-5}}$mbar for 30min. In units of Langmuir (1 Langmuir = 1 L = 10^{-6}Torr s), this corresponds to an exposure of 27000L, which is high enough to ensure that a dense monolayer of the c(4x2) phase is built |171|.

Several gold terraces are visible in figure 3.6(a). The monolayer of C12 can be seen by a stripe pattern with a periodicity of 1nm, which indicates the c(4x2) structure. Compared to the SAMs grown from solution, the size of the domains of C12 increases dramatically. No domain boundaries can be seen and the domain extends over the whole gold terrace. Since Kondoh et al. [171] also showed large area domains of a hexanethiol (C6) SAM grown by vapor deposition, this effect seems to be due to different growth dynamics of vapor phase growth compared to growth from solution. Compared to SAMs of alkanethiols grown from solution, the one gold atom deep vacancy islands are not connected by domain boundaries and there is a large variation in size of the vacancy islands.

In high resolution images, the c(4x2) reconstruction can be resolved (figure 3.6 and 3.7). Two different phases of c(4x2) can be identified: the normal δ-phase with two different heights in each unit cell (figure 3.6) and a new phase with four different heights (figure 3.7).

Cross sections along line A (NNN-direction) and line B (NN- direction) of the δ-phase are shown in figure 3.6(b) and 3.6(c). An exact analysis yields a ($\mathbf{5.3}$Å$\times\mathbf{5.1}$Å) lattice in agreement with the $\mathbf{(\sqrt{3} \times \sqrt{3})R30°}$ basis structure. Compared to the high resolution images on solution grown samples (figure 3.3(b)), the single molecules are much better resolved indicating a higher cleanliness of the film. In the upper right corner of figure 3.6(b), a single vacancy island can be identified. Molecules that cover the bottom of the vacancy island are clearly visible, confirming that vacancy islands are not due to holes in the C12 lattice.

The height differences between neighboring molecules of the new phase are shown in the cross sections along line A and B in figure 3.7. Along line A, there are groups of four molecules, in which each molecule appears approximately 0.3Å lower than the preceding molecule. Along line B, one high molecule and one low molecule alternate. This pattern leads to the ζ-phase shown in figure 3.7(b) [172]. Because both phases, the normal δ-phase and the new ζ-phase, can be resolved on the same sample with the same tip and the same scanning parameters, it can be excluded that the new phase is due to tip artifacts.

As discussed in the introduction to section 3.1, the new ζ-phase can be explained by the disulfide model of Fenter et al. |148|, the twisting of the molecules or a combination of both. A slight modification of the disulfide model, which results in its original form in

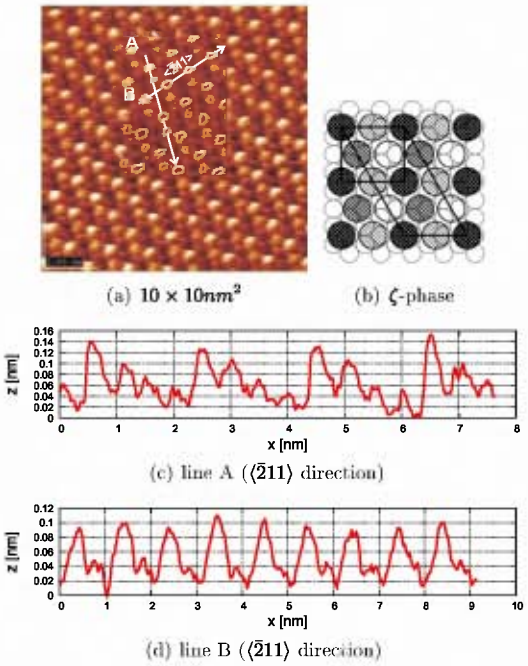

(a) $10 \times 10nm^2$ (b) ζ-phase

(c) line A ($\langle\bar{2}11\rangle$ direction)

(d) line B ($\langle\bar{2}11\rangle$ direction)

Figure 3.7: New ζ-phase of the c(4x2) structure [172]. Part (c) and (d) show cross sections along line A and B (both NN-directions), respectively. The cross sections lead to the model shown in part (b).

two different STM heights, can account for the height modulation presented here. More than two inequivalent bonding sites of the sulfur head group on the Au(111) surface or likewise two different bonding sites of the disulfides on the gold substrate would lead to different tunneling conditions and to four molecules having different heights in STM images.

Similarly, if more than two twist angles in the unit cell are assumed, one could also explain the structure presented here. The maximum height difference observed in the new structure (approx. 0.9Å) is close to the maximum height difference that can be explained by a twist of the molecular backbone [144]. Since STM cannot distinguish between real height differences due to a twist of the molecules and differences in tunneling conditions due to inequivalent bonding sites, the structure shown in figure 3.7 can be explained by both theories.

3.5 Conclusion

Self-assembled monolayers are grown from solution and from the gas phase. Both deposition methods result in highly ordered monolayers and adopt the c(4x2) structure.

SAMs grown from solution have small molecular domains and many small vacancy islands. Annealing the samples for a short time in solution results in an increase in domain size and a decrease in vacancy island number. For longer annealing times, desorption of the molecules becomes important, which leads to the appearance of lying-down and new standing-up molecular structures.

SAMs grown from the gas phase are superior to samples grown from solution in terms of domain size and cleanliness of the film. It is shown that the samples display different phases of the c(4x2) structure, the well known δ-phase and a new ζ-phase.

Chapter 4

Self-Assembled Monolayers of Biphenylthiols

The electron transfer properties of full coverage self-assembled monolayers of biphenylthiols (CH_3-C_6H_4-C_6H_4-$(CH_2)_n$-SH, **BPn**, n: number of CH_2 units included between biphenyl and sulfur group, see figure 4.1(a)) is studied by current vs. voltage and current vs. distance spectroscopy. Before characterizing these layers electrically, the structure of these layers is determined by UHV-STM.

The measurement of the electrical characteristics of BPn reveals some important aspects that can be used in the discussion of the electron transport properties of embedded BPn, which is described in the next chapter. Therefore, full coverage SAMs of BPn are a suitable test system in preparation for the next chapter, which describes how the BPn molecules are embedded into an alkanethiol SAM.

4.1 The Structure of SAMs of BPn

SAMs built of aromatic thiols display various properties which make them interesting for future applications. For molecular electronics it is of great importance that the tunneling conductance along the molecular backbone is increased due to the conjugation along the molecular axis of the molecules. For example, Bumm et al. [23] showed that an aromatic molecule inserted into an alkanethiol SAM behaves like a molecular wire, i.e. the embedded molecules show an increased conduction compared to the surrounding alkanethiol SAM. Furthermore, due to stronger intermolecular interaction compared to aliphatic thiols (π-π interactions versus van der Waals interaction), aromatic thiols are assumed to form more stable SAMs. Even for lithography, SAMs of aromatic thiols are of great interest. Whereas aliphatic SAMs act as positive resist under electron irradiation (i.e. the SAM is destroyed), aromatic SAMs quasi-polymerize and thereby form a negative resist [173].

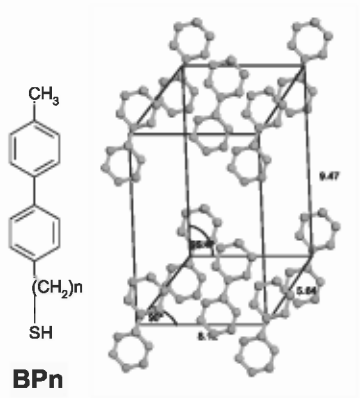

Figure 4.1: In (a) the structural formula of ω -(4'-methyl-biphenyl-4)-alkanethiols (BPn) is shown. (b) illustrates the 3D crystal structure of biphenyl. The monoclinic unit cell is occupied by two molecules.

Self-assembled monolayers of different aromatic molecules like arenethiols [174, 175], phenylthiols [176, 177], biphenylthiols [178 183], biphenyldithiols [184] or terphenylthiols [185] have been studied. In a study by Tao et al. [186] it was shown that the order of a biphenylthiol-SAM is greatly increased by the inclusion of a CH_2 group between the sulfur and the biphenyl group.

This observation triggered several studies concerning the structure of SAMs built by molecules of the homologous series of 4´-methyl-1,1´-biphenyl-4-alkanethiols (CH_3-C_6H_4-C_6H_4-$(CH_2)_n$-SH, **BPn**, n: number of CH_2 units included between biphenyl and sulfur group, see figure 4.1(a)). This new kind of SAM was studied using IR-spectroscopy and ellipsometry [186, 187], near edge X-ray adsorption fine structure (NEXAFS), Fourier transform absorption spectroscopy (FTIRRAS) and X-ray photoelectron spectroscopy (XPS) [188], high-resolution XPS [183], cyclic voltammetry [189, 190] and Scanning Tunneling Microscopy (STM) [191–194].

SAMs of BPn can be divided into two classes: one class in which an even number of CH_2 groups is included between the sulfur group and the biphenyl unit (BPn, n=even) and another class in which the number is odd (BPn, n=odd). These two classes differ, for example, in their resistance to electron beam modification [173], in desorption potentials [190] and in resistance to replacement by alkanethiols [189]. In all these studies, BPn with n−even is shown to be more unstable. This effect is explained by different molecular conformations in the SAMs, i.e. different bonding angles and orientations of the biphenyl group of odd and even numbered BPn, which in turn is caused by the

structural mismatch between the bulk crystal structure of biphenyls and the crystal structure of the supporting gold lattice.

In its crystalline form, biphenyl adopts a monoclinic unit cell occupied by two molecules (a=8.12Å, b=5.64Å, c=9.47Å, β=95.4° , see figure 4.1(b)) [195]. Most important, the biphenyls are inclined by an angle of 18.6° relative to the |001| direction. For 2D assembly, this structure has to be matched with the gold lattice via anchoring sulfur groups and alkane chains.

The sulfur group preferentially binds to the gold lattice in a sp^3 configuration and thereby the lowest energy configuration of the linkage between gold and sulfur displays a C-S-Au angle of 104° [187]. For an odd number of CH_2 units, this C-S-Au angle causes the last CH-bond to be oriented rather upright and allows the biphenyl unit to adopt a conformation close to its bulk structure (see figure 4.2(a)). By IR-spectroscopy and NEXAFS it is shown that the biphenyl unit in SAMs of BPn with n=odd is inclined only by 23° out of the surface normal, close to the bulk value of 18.6° [187]. Furthermore, STM experiments showed that the molecule adopts a $(2\sqrt{3} \times \sqrt{3})R30$ or equivalently a $(3 \times \sqrt{3})$rect lattice (see figure 4.3(a)) with intermolecular distances of 8.66Å and 5Å, which are also close to the bulk values of 8.12Å and 5.64Å [193, 194]. Therefore, for an odd number of CH_2 units, the molecule can adopt a low energy conformation, both in terms of sulfur bonding to the gold lattice and orientation of the biphenyl unit.

For an even number of CH_2 groups, the molecule cannot adopt such a low energy conformation. As can be seen in figure 4.2(b), due to the even number of carbon atoms, the tilt of the last CC-bond and the biphenyl group is significantly increased compared to odd numbered BPn. This causes the biphenyl group to be forced out of its preferred crystal structure. To relax this unfavorable conformation of the biphenyl unit to some extent, the C-S-Au bonding angle is increased so that the alkane chain adopts a rather upright position and the tilt angle of the biphenyl group is reduced. The resulting conformation is shown in figure 4.2(b). The biphenyl unit is tilted by 45° out of the surface normal and the C-S-Au bonding angle is increased to above 130° [187]. However, this structure is only a compromise between the crystal structure of biphenyls and the prefered Au-S-C bonding angle. Both the increased tilt of the biphenyl group compared to the crystal structure, which decreases the distance between neighboring biphenyl groups, and the increase in C-S-Au bonding angle, are energetically costly.

This mismatch of bulk and SAM structure results in energetically unfavorable structures and therefore less stable SAMs. This energy can be partly decreased by increasing the intermolecular distances compared to the spacing found for BPn, n=odd. However, due to the very complex interplay between the preferred orientation of the biphenyl unit, the preferred Au-S-C bonding angle and the binding site, more than just one surface structure was found by STM for BPn, n=even. The probably best characterized

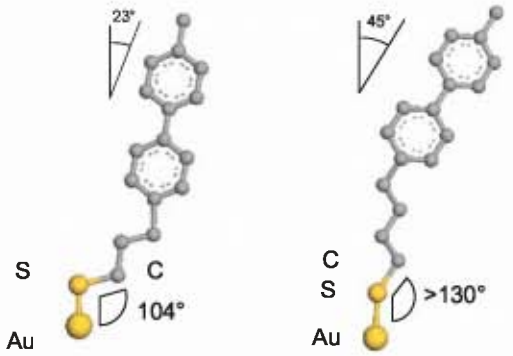

Figure 4.2: Conformation of BPn in an SAM for n=odd (a) and n=even (b)[187]. Compared to the conformation of BPn, n=odd, even numbered BPn differ strongly from the bulk biphenyl structure and the preferred Au-S-C bonding angle (104°) is greatly increased, resulting in a less stable SAM.

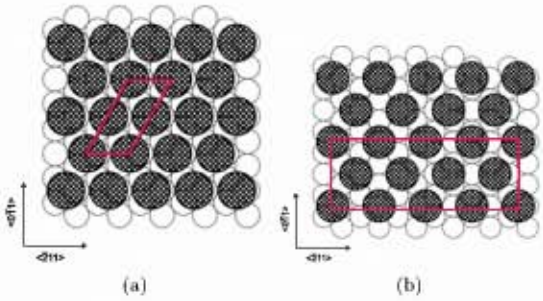

Figure 4.3: $(2\sqrt{3} \times \sqrt{3})$ structure for BPn, n=odd (a) and $(3 \times 5\sqrt{3})$ structure for n=even (b).

	Structure	Deposition Temperature	Reference
BP2	$\left(3 \times 5\sqrt{3}\right)$	RT, 333K-343K	[193, 194]
	$\left(2\sqrt{3} \times 4\right)$	RT, 333K	[196]
	$\left(3 \times 2\sqrt{3}\right)$	330K	[197]
BP4	$\left(3 \times 5\sqrt{3}\right)$	RT, 333K-343K, 360K	[193, 194, 198]
	$\left(6\sqrt{3} \times 2\sqrt{3}\right)$	373K	[192]
	$\left(3 \times 4\sqrt{3}\right)$	330K	[197]
	$\left(2\sqrt{3} \times 5\sqrt{3}\right)$	360K	[198]
BP6	$\left(3 \times 5\sqrt{3}\right)$	RT, 343K	[193]
	$\left(2\sqrt{3} \times 5\sqrt{3}\right)$	360K, 390K	[198]
	$\left(2\sqrt{3} \times 6\sqrt{3}\right)$	390K	[198]

Table 4.1: Different structures of even numbered BPn molecules

structure is a $\left(3 \times 5\sqrt{3}\right)$ structure [193, 194], shown in figure 4.3(b). Cyganik et al. state that this structure applies to all BPn with n=even [193]. The structure consists of eight molecules with an intermolecular distance of 5Å along the $\langle 0\bar{1}1 \rangle$ and 6.25Å along the $\langle \bar{2}11 \rangle$-direction. The distance of 6.25Å implies that the molecules have to bind at different sites on the gold lattice [193] and that the density of molecules on the gold surface is decreased by approximately 25% compared to odd numbered BPn. Besides this structure, various other structures have been found by different authors. These structures are listed in table 4.1.

4.2 Experimental Details

As for alkanethiol SAMs, gold films are prepared in the two step deposition process described in section 2. Biphenylthiols are synthesized according to Rong et al. [187] via Grignard C-C coupling, reactions of the corresponding phenyl- or alkylbromides, and finally the conversion of the bromide into the thiol via thiourea[1].

For solution deposition, the gold films are kept in a 0.1mM ethanolic solution of the molecules overnight. The films are thoroughly rinsed before they are transferred to the UHV-STM. Following deposition, the films are heated in vacuum (1×10^{-9}mbar) by an indirect resistive heating element at 64°C for 1-2h to desorb physisorbed molecules, before the SAMs are characterized by a UHV- STM (JEOL JSPM 4500, base pressure 3×10^{-10}mbar).

For gas phase deposition, the same experimental setup as for alkanethiols is used.

[1] This synthesis was done in the group of Prof. U. Simon at the Institute of Inorganic Chemistry at the RWTH Aachen.

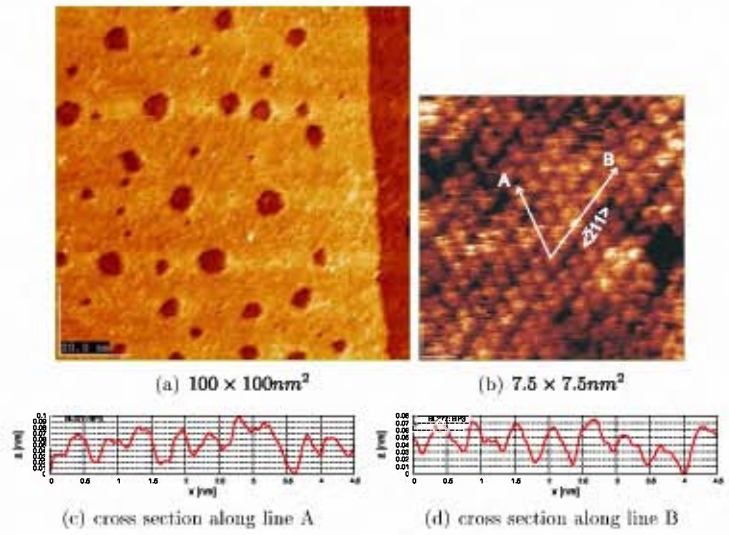

(a) $100 \times 100nm^2$ (b) $7.5 \times 7.5nm^2$

(c) cross section along line A (d) cross section along line B

Figure 4.4: STM scan of BP3 SAM. (a) shows a large area scan ($100 \times 100nm^2$, $V_t = 1V, I_t = 100pA$). In (b) a higher resolution scan is shown, which reveals the $\left(2\sqrt{3} \times \sqrt{3}\right)$ structure. (c) and (d) are cross sections along line A and B.

The biphenylthiols are evaporated at 75°C and the biphenylthiol vapor is directed via a valve and a nozzle onto the gold film. To avoid adsorption onto the walls of the deposition chamber, the chamber is heated to 100°C . Similar to the samples grown from solution, the films are transferred to the UHV-STM system immediately after deposition.

4.3 Structural Characterization

4.3.1 Biphenylthiols with an Odd Number of Carbon Atoms – BP3

Figure 4.4(a) shows a large area scan of an SAM of BP3 ($100 \times 100nm^2$). The film is deposited by immersing the sample into a 0.1 mM solution of BP3 for 29h. Following deposition, the film is annealed at 64°C for 3h.

The film resembles SAMs of alkanethiols as shown in chapter 3. On the right-hand side, the edge of a gold terrace with the characteristic step height of 0.24nm can be seen. Furthermore, the top of the terrace on the left-hand side is covered by holes with diameters of 5-8nm and depths which equal the gold terrace step height. Thereby, these holes can be identified as gold vacancy islands of the same character as

the vacancy islands seen in layers of alkanethiols (see section 3.3). The vacancy islands for alkanethiols have been explained by the lifting of the herringbone reconstruction of (111)-oriented gold and the subsequent release of two gold atoms per herringbone unit cell. Considering that BP3 or biphenythiols in general also attach via gold-sulfur bonding to the reconstructed gold surface, the occurrence of the vacancy islands in biphenylthiol SAM can be explained in the same way as for alkanethiols.

Upon close inspection, a structure formed by the BP3 molecules can be seen on top of the terraces and several domains can be identified. In contrast to SAMs of alkanethiols, these domains are not separated by deep trenches as visible in figure 3.3(a).

In figure 4.4(b), a high resolution scan of a single domain of BP3 is shown. Exact analysis reveals a $\mathbf{0.92}$nm$\times\mathbf{0.54}$nm lattice in agreement with the $\left(\mathbf{2\sqrt{3} \times \sqrt{3}}\right)$ structure found by Azzam et al. [193, 194] (see figure 4.3(a)). This $\left(\mathbf{2\sqrt{3} \times \sqrt{3}}\right)$ unit cell consists of two inequivalent molecules. Whereas Azzam et al. observed that these two molecules differ in their apparent height, in the measurement shown in figure 4.4(b) the molecules differ slightly in their position. Along line A in figure 4.4(c) there are always pairs of two molecules with a slightly decreased distance. This can also be seen as rows of double lines of molecules in figure 4.4(b) that run along line B ($\langle\bar{2}11\rangle$-direction). This pairing of molecules can be explained by both different bonding sites of the sulfur group to the gold lattice and slightly different conformations of the molecules. Since STM provides only an image of the top of the SAM, these two explanations cannot be distinguished.

4.3.2 Biphenylthiols with an Even Number of Carbon Atoms – BP2 and BP4

As an example of an odd numbered BPn, BP3 was shown in the preceding section to exhibit a very well defined surface structure with a unit cell that fits onto the gold lattice. However, as already indicated in the introduction, BPn with n=even behaves remarkably differently.

Deposition of BP2 at room temperature

In figure 4.5(a), a $\mathbf{300 \times 300}\boldsymbol{nm^2}$ STM scan of BP2 is shown. Similar to the SAM of BP3, the film is grown from solution at room temperature (immersion time 16h30min) and annealed at $\mathbf{64°C}$ for 1h50min in vacuum. As for the BP3 film in figure 4.4(a), the film shows gold vacancy islands on the whole surface of the film. In contrast to the BP3 film, between individual domains of BP2 molecules the domain boundaries are again visible as trenches.

A high resolution scan of an SAM of BPn with n=even proves to be more difficult than for n=odd. Furthermore, the quality of the scans is poorer than for BP3 so that, for structural analysis, the scans had to be slightly fourier filtered.

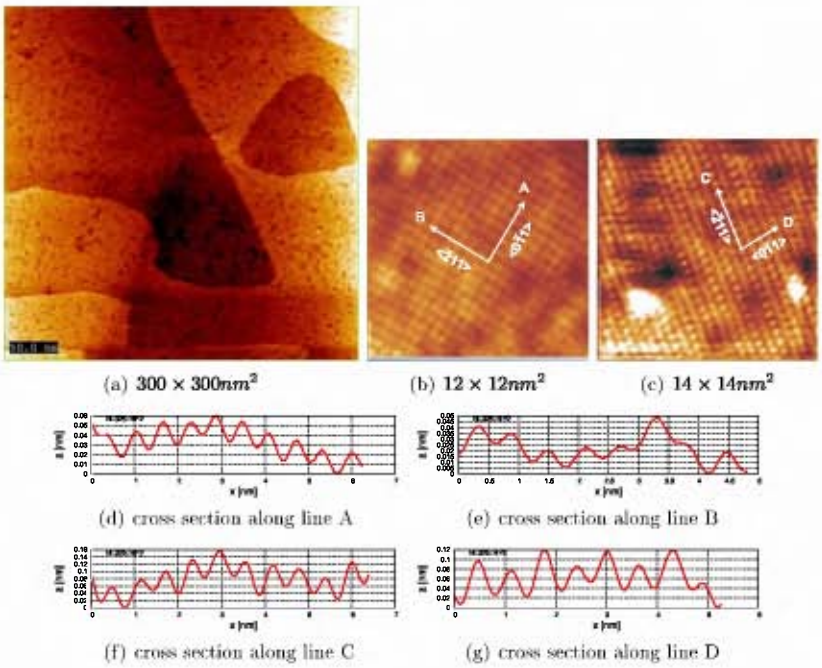

(a) $300 \times 300nm^2$ (b) $12 \times 12nm^2$ (c) $14 \times 14nm^2$

(d) cross section along line A (e) cross section along line B

(f) cross section along line C (g) cross section along line D

Figure 4.5: STM scan of BP2 SAM. (a) shows a large area scan ($300 \times 300nm^2$, $V_t = 0.2V, I_t = 500pA$). (b) and (c) show two structures: both can be described by an $(4 \times 6\sqrt{3})$ unit cell. (d) to (g) are cross sections along line A to D.

Two structures can be resolved in BP2 SAMs grown at room temperature, shown in figure 4.5(b)-4.5(g). The first structure is shown in the STM scan in figure 4.5(b). It can be described by a quadratic lattice with a lattice constant of ~ 0.6nm ($0.61nm \times 0.62nm$). Assuming commensurability, this structure can be mapped to the gold lattice as a $(4 \times 6\sqrt{3})$ structure as shown in figure 4.6(b). The structure consists of ten molecules. Along the $\langle\bar{2}11\rangle$-direction, the molecules adopt different bonding sites and after five molecules the same bonding site as for the first one is reached again. It should be noted that due to the variety of bonding sites, this structure has only a very loose relationship to the gold lattice.

The second structure is shown in figure 4.5(c) and in the cross sections in figures 4.5(f) and 4.5(g). It can be described by the same $(4 \times 6\sqrt{3})$ unit cell as the previous structure (measured unit cell size: $1.27 \times 3.08nm^2$). The only difference lies in the position of the molecules in the center of the unit cell. Compared to the structure shown in figure 4.6(b), the molecules in the center of the unit cell move to the left (see

figure 4.6(a)).

In particular, the structure shown in figure 4.6(a) is very similar to the $(3 \times 5\sqrt{3})$ structure described by Azzam et al. [193, 194] (see figure 4.3(b)). Compared to this structure, the unit cell shown in figure 4.5(c) is expanded along the $\langle 0\bar{1}1 \rangle$-direction (from 0.86nm to 1.2nm) and the spacing of the molecules along the $\langle \bar{2}11 \rangle$-direction is slightly decreased from 0.625nm to 0.6nm. This decrease causes the length of the unit cell to increase to $6\sqrt{3}$ compared to $5\sqrt{3}$, because only after 5 molecules is the same bonding site on the gold lattice as for the first molecule reached again. Whereas this difference in intermolecular spacing along the $\langle \bar{2}11 \rangle$-direction is very small and lies probably within the error margin of the STM, the expansion along the $\langle 0\bar{1}1 \rangle$-direction is too large to be explained by measurement artifacts.

Deposition of BP2 at Higher Temperatures

The deposition of BP2 at room temperature resulted in structures which deviate slightly from the unit cell described in literature. By deposition of BP2 at higher temperatures it is possible to explain this difference.

In figure 4.7 a SAM of BP2 is shown, which is deposited at 90°C for 7h in solution. Several of the films characteristics differ from the room temperature sample. As already seen for annealing of SAMs of alkanethiols in solution, the number of vacancy islands decreases and their diameter increases. This effect has been explained by an Ostwald ripening mechanism (see section 3.3.1). Furthermore, compared to the room temperature sample the diameter of the domains of the high temperature sample increases to 30 - 50nm.

This increased domain size leads to the occurrence of another very interesting observation. Within the molecular domains, the SAM displays a long range periodic height variation. The period and orientation of this long range pattern varies slightly on the sample (3-6nm). This observation is in accordance with the studies by Cyganik et al. on SAMs of BP2 deposited at 70°C [191]. They explained this pattern by a mismatch between the lattice constant favored by BP2 and the Au lattice. The strain due to this mismatch is relaxed by forming small regions, in which the SAM is commensurate with the gold lattice. These small regions are separated by so-called solitons or domain walls, in which the molecules adopt different adsorption sites and in which the registry with the gold lattice is low.

This model proposes regions of perfect registry with the gold lattice and regions in which the registry is broken. The mismatch between the SAM and the gold lattice is relaxed only in the domain walls. Analogous to the discussion of the herringbone reconstruction in section 2.4.2, one can also postulate that the strain due to the mismatch is not only relaxed in the domain walls, but that the mismatch is homogeneously

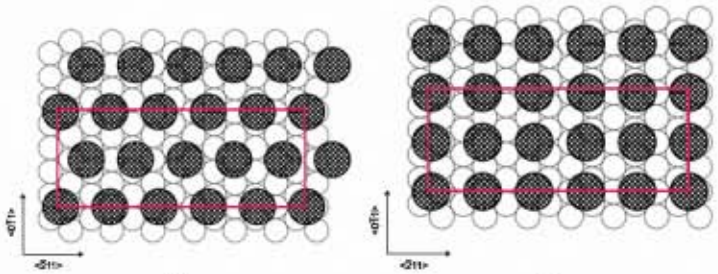

(a) (b)

Figure 4.6: Schematic of $(4 \times 6\sqrt{3})$ structures as seen in figure 4.5(b) and 4.5(c).

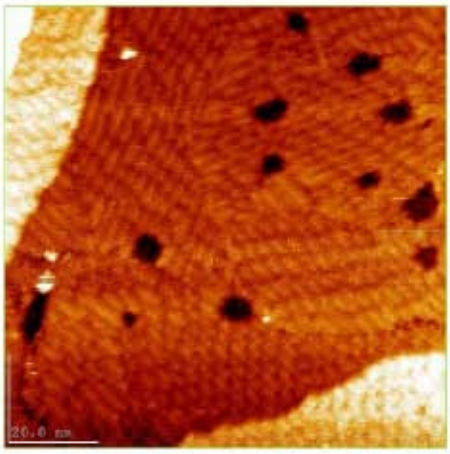

Figure 4.7: STM scan of a BP2 SAM grown at 90℃ ($100 \times 100nm^2$, $V_t = 1.5V, I_t = 100pA$). A long range height variation is visible.

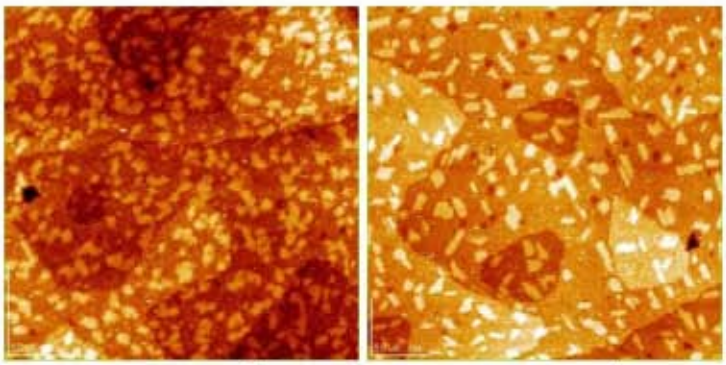

(a) $200 \times 200nm^2$ (b) $300 \times 300nm^2$

Figure 4.8: SAM of BP4 grown from the gas phase. (a) and (b) show an SAM with a sub monolayer coverage. (a) shows the film as deposited, whereas in (b) the SAM is annealed at 64°C for 12h30 hours.

distributed over the whole SAM. This model is supported by the observation that the height pattern is smooth and continuous and does not show sharp transitions as one would expect for the model, in which the misfit is relaxed only in the domain walls.

Both of these explanations show that BP2 exhibits a high structural misfit with the gold lattice. As already discussed in section 4.1, BPn with n−even can only bind to the gold lattice by increasing the Au-S-C bond angle and the tilt of the biphenyl unit. Both of these deviations from the energetically lowest configuration generate stress in the SAM. Therefore, SAMs of BPn with n−even are less stable than for n−odd and have only a low registry with the gold lattice. Cyganic et al. even state that "the simple unit cells often determined from STM measurements have to be viewed with caution. Given the limited precision of STM techniques, images have to be acquired on scales large enough to reveal longer range contrast variations indicative of incommensurability" [191].

This low registry with the gold lattice of BP2 can explain the difference of the structures shown in figure 4.5(b) and 4.5(c) from the $(3 \times 5\sqrt{3})$ structure described by Azzam et al. [193, 194] (see figure 4.3(b)). The structure of BP2 on Au(111) is not as well defined as for odd numbered BPn and consequently different structures are possible.

Deposition of BP4 from the Gas Phase

As a second example of even numbered BPn, SAMs of BP4 are examined. In accordance with the experience from alkanethiol SAMs, where it was shown that gas phase

deposition yields SAMs with a higher order, the SAMs of BP4 are prepared from the gas phase.

Figure 4.8(a) shows an SAM of BP4 grown at low exposures (p=1.5×10^{-5}mbar, t−1min), resulting in a coverage of less than one monolayer. The film consists of several islands of BP4 with an approximate diameter of 5-10nm and a height of 3-4 Å. The shape of the islands is highly irregular.

Heating the sample at 64℃ for 12h30min yields a change in surface morphology (see figure 4.8(b)). The islands of BP4 adopt a more regular shape with straight edges. The islands have a slight form anisotropy, i.e. they are elongated along one axis. Most interestingly, the orientation of different islands differs by angles of multiplies of 60°, which can be explained by the hexagonal structure of the (111)-gold substrate.

Between different BP4 islands, gold vacancy islands have formed. The height of the biphenyl islands does not change significantly by the additional annealing step and at 3-4Å is still much lower than the theoretical height of a BP4 molecule (~ 12.5Å). This height difference is due to the principle of operation of the STM. All images are acquired in the constant current mode of the STM, i.e. the height of the STM tip above the molecule is adjusted by the feedback loop of the STM so that the tunneling current is kept constant. Therefore, the STM always measures a combination of physical height difference and differences in the tunneling conditions. Since tunneling from the gold substrate through a biphenyl molecule is different from tunneling directly from the gold substrate to the tip, the height difference as measured by STM is much lower than the physical height of a BP4 molecule. In the following chapter, this behavior of the STM will be used to explain the height difference in SAMs composed of different molecular species.

Longer exposures yield full coverage SAMs as shown in figure 4.9(a). This SAM is grown at a pressure of BP4 vapor of 5×10^{-6}mbar for 30min. Different domains and several gold vacancy islands can be seen. The domains exhibit a patterned surface. By zooming into a domain of BP4, the high resolution scan shown in figure 4.9(b) is acquired. Similar to the structure of BP2 shown in figure 4.5(b), the molecules form a rectangular lattice. However, the lattice constants are slightly different. Whereas along line A the molecules have a distance of 0.63 nm, along line B the distance is decreased to 0.51nm. Therefore, this structure can be described by a $(4 \times \sqrt{3})$ lattice as shown in figure 4.11. This structure has already been observed by Azzam for BP2 grown at room temperature [196].

Annealing the sample at 64℃ does not change the surface morphology significantly (see figure 4.10(a)). A close inspection of the structure shown in figure 4.10(b) yields the same $(4 \times 6\sqrt{3})$ unit cell as already observed for BP2 (measured unit cell size $1.16 \times 3.7nm^2$, see figure 4.5(c)). The occurrence of this structure compared to the

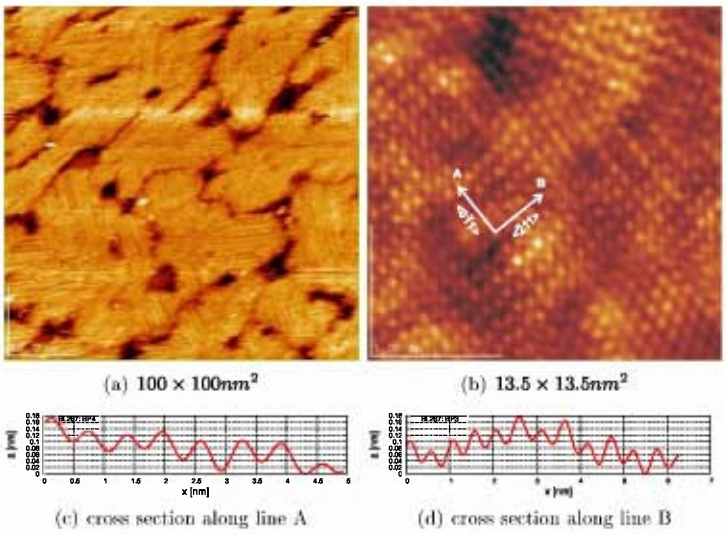

(a) $100 \times 100nm^2$ (b) $13.5 \times 13.5nm^2$

(c) cross section along line A (d) cross section along line B

Figure 4.9: STM scan of a BP4 SAM grown from the vapor phase ($100 \times 100nm^2, V_t = 2V, I_t = 50pA$). (b) shows a high resolution image. (c) and (d) are cross sections along line A and B.

$(4 \times \sqrt{3})$ structure seen in the sample before annealing is not necessarily an effect of the annealing step. More probably, considering the stress in the films due to the structural misfit of the biphenylthiols and the gold lattice, both structures coexist before and after annealing.

4.3.3 Conclusion

The structure of SAMs of biphenylthiols on gold has been studied. These SAMs display a distinct odd-even effect. Whereas BPn with n=3 as an example of odd numbered BPn [193, 194] shows a very well defined $\left(2\sqrt{3} \times \sqrt{3}\right)$ structure, the structure of BPn with n=even is much less defined.

This behavior can be explained by the structural misfit of BPn with n=even with the gold lattice. The structure of the SAMs is defined by the interplay of intermolecular forces (i.e. forces between the biphenyl units), the preference of the Au-S-C bond for the sp^3 angle of 104° and the tendency of the molecule to bind to the gold threefold hollow sites. For BPn, n− odd, all these energy contributions can be minimized, i.e. the forces between the biphenyl units are minimized since they almost adopt their crystalline orientation, the Au-S-C bond is approximately 104° and the molecules bind to the threefold hollow sites.

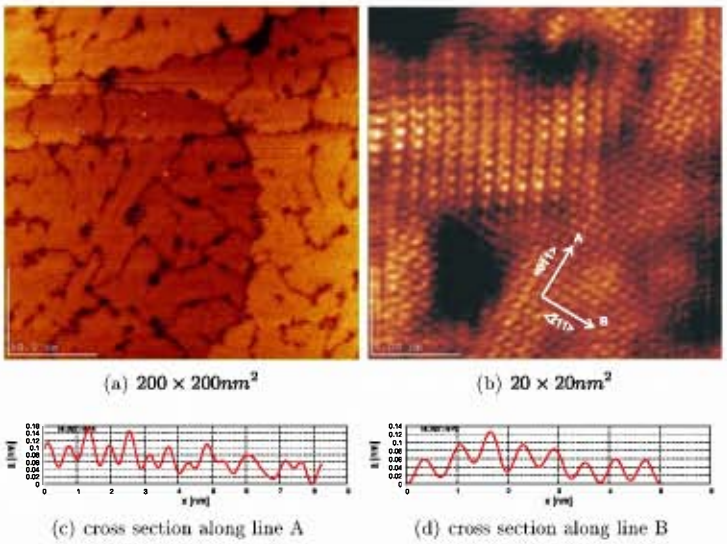

(a) $200 \times 200nm^2$ (b) $20 \times 20nm^2$

(c) cross section along line A (d) cross section along line B

Figure 4.10: STM scan of a BP4 SAM grown from the vapor phase ($200 \times 200nm^2, V_t = 1.5V, I_t = 50pA$) and annealed at 64°C . (b) shows a high resolution image. (c) and (d) are cross sections along line A and B.

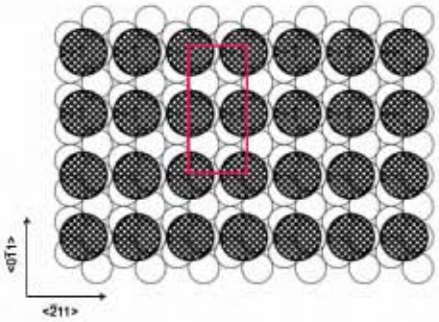

Figure 4.11: $(4 \times \sqrt{3})$ of BP4 grown from the gas phase.

Such a configuration is not possible for n=even, because the even number of CH_2 units forces the biphenyl unit into a considerably more tilted conformation. Thereby, the whole structure is determined by a very complex compromise between the forces acting on the molecule. This makes the structure of BPn, n=even, much less defined and consequently different molecular structures are found: a $(4 \times 6\sqrt{3})$ structure for BP2 and BP4 and a $(4 \times \sqrt{3})$ structure for BP4. Considering the low registry of the $\left(4 \times 6\sqrt{3}\right)$ structure shown in figure 4.6(a), it can be questioned whether the structure is commensurable or if the π-π interactions of the biphenyl units outweigh the forces the gold substrate can exert on the molecule. However, at least a small influence of the gold lattice can be seen in figure 4.8(b), where the different BP4 islands grow in the $\langle 01\bar{1} \rangle$ directions of the gold lattice.

4.4 Electrical Characterization of SAMs of BPn

The full coverage SAMs of BPn have primarily been studied to characterize the electron transport properties of biphenylthiols in a dense monolayer before turning to the more difficult case of single BPn molecules embedded in an alkanethiol SAM. Therefore, after having examined the structure of SAMs of BPn, the current transport through layers of BPn is measured by current vs. voltage and current vs. distance spectroscopy.

4.4.1 Current vs. Voltage Spectroscopy

An IV characteristic of an SAM of BP2, deposited for 16.5h in 0.1 mM solution, is shown in figure 4.12(a). It is measured by positioning the STM tip above the SAM, controlling the distance between the tip and the film to a certain set-point (0.2V, 100-500pA), switching off the feedback of the STM and sweeping the voltage from $-2V$ to $2V$. Three plots for three different current set-points are shown: for 100pA(black),

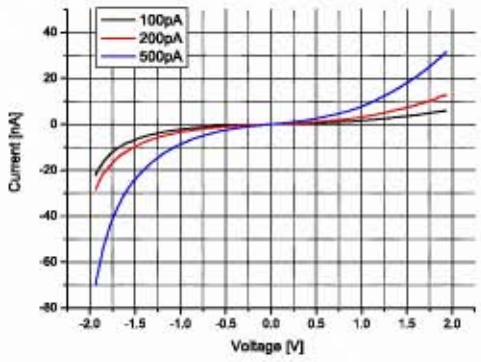

(a)

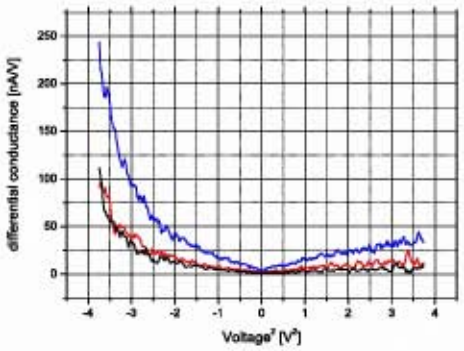

(b)

Figure 4.12: IV-characteristic (a) and differential conductance (b) of the SAM of BP2 shown in figure 4.5(a) for different tunneling conditions ($V_t = 0.2V, I_t = 100pA, 200pA, 500pA$).

200pA(red) and 500pA(blue). In addition, in figure 4.12(b), the derivative of the IV function, i.e. the differential conductance, is shown.

A comparison of the different plots for different current set-points shows that the current and the conductance increase with increasing set-point current. This increase in current and conductance with the current set-point can be explained by the mode of operation of the STM. By increasing the set-point current, the size of the vacuum gap between the tip and the molecule is decreased by the feedback loop of the STM until the set-point current is reached for the same tunneling voltage (0.2V). Consequently, the tip/vacuum gap/molecule/gold junction becomes more conductive.

Most interestingly, both the current and the conductance are asymmetric and show a higher conductivity for negative voltages. This asymmetry of the IV dependence is caused by the asymmetric measurement setup. The molecule is coupled differently to contacts of different materials. Whereas the molecule is covalently bonded to the gold substrate by the sulfur group, the top of the molecule is only weakly coupled to the tungsten tip. Therefore, depending on the polarity of the voltage, the current has to tunnel through barriers of different heights.

Figures 4.12(a) and 4.12(b) show that all IV-characteristics and the differential conductance exhibit a tunneling behavior. This behavior of the current and the differential conductance can be explained using the ideas of section 1.3.1. It has been shown that the current below the lowest energy level of the molecule is described by the Simmons equation (1.19).

$$j = j_0 \{\bar{\phi} \exp\left[-\gamma\beta(\bar{\phi})L_z\right] - (\bar{\phi} + eV) \exp\left[-\gamma\beta(\bar{\phi} + eV)L_z\right]\} \tag{4.1}$$

$$j_0 = \frac{e}{2\pi h(\gamma L_z)^2} \tag{4.2}$$

$$\beta(\bar{\phi}) = 2\sqrt{\frac{2m\bar{\phi}}{\hbar^2}} \tag{4.3}$$

Several approximations are given for low, intermediate and high voltages (see table 1.2). For low voltages, equation (1.19) predicts a linear dependence of the current on the voltage and in the intermediate voltage range a proportionality of $I \propto V + \delta V^3$. For high voltages, the current rises exponentially with the voltage. Consequently, the differential conductance rises quadratically in the intermediate regime and exponentially in the high voltage regime.

The Simmons equation is valid only below the lowest molecular level. If the voltage is large enough for a molecular level to enter the energy window $[-eV/2, +eV/2]$, the current and the conductance rise sharply (see figure 1.6). However, such a sharp increase in current is neither visible in the IV plot (figure 4.12(a)), nor in the plot of the differential conductance (figure 4.12(b)). Therefore, the current can indeed be described

by a pure tunneling current below the lowest energy level and the Simmons equation (1.19)-(1.21) can be applied.

This absence of any resonant peak due to a molecular level is in accordance with the results of Hong et al. [199]. In their publication, they used current vs. voltage spectroscopy of various phenylene compounds and particularly of biphenylthiols very similar to those used in this thesis. They only observed a resonant peak above 2.5V, a voltage which leads to irreversible destruction of the film in the experiments conducted for this thesis.

The applicability of the Simmons model can be further validated by figure 4.12(b). In this plot, the conductance is plotted versus V^2. For positive voltages, the plot shows a linear behavior, whereas for negative voltages, the plot is linear only for voltages below $\sim 1.5V$. For larger voltages, the conductance rises exponentially. Therefore, the approximation for intermediate voltages can be used for positive voltages below 2V and negative voltages below 1.5V.

4.4.2 Current vs. Distance Spectroscopy

As already mentioned in the discussion of figure 4.12(a), the current rises with increasing current set-point. This has been explained by a decreasing distance between the STM tip and the molecule. A more systematic way of examining the dependency of the current on the tunneling distance d between the tip and the gold substrate is the current vs. distance spectroscopy (IS-spectroscopy).

For this kind of spectroscopy, the STM tip is positioned above the SAM. As for the current vs. voltage spectroscopy, the distance between the tip and the SAM is controlled by the tunneling set-point (current and voltage set-point). Once the feedback of the STM has adjusted the tunneling set-point, it is turned off, the tip is moved towards the SAM and the current is measured simultaneously.

IS Spectroscopy of BP2

Figure 4.13 shows the result of an IS measurement of the same SAM as in figure 4.12(a). The distance axis is a relative axis, a tip displacement of 0nm denotes the position of the tip at the tunneling set-point (2V, 100pA). Negative displacements represent an increase in tunneling distance (i.e. the tip is retracted), and positive displacements a decrease in tunneling distance (i.e. the tip is pushed towards the SAM).

Figure 4.13 is a logarithmic plot of the current. Four domains can be identified. Below -0.1nm, the tunneling current is lower than the noise level ($\sim 1pA$) so that only noise is measured. Above $-0.1nm$, all domains show a logarithmic dependency of the current I on the distance d and differ only in the slope of the function $\ln(I) = f(d)$. Whereas below $0.07nm$ the slope is steep, above $0.07nm$ the slope of the plot decreases

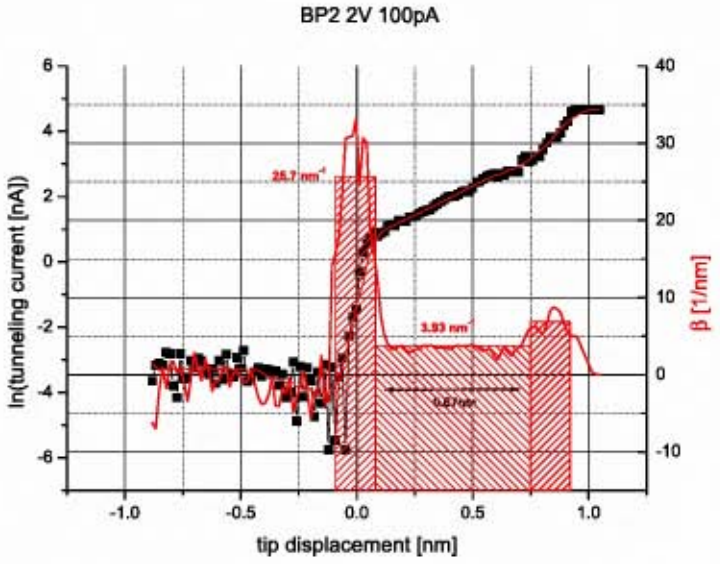

Figure 4.13: Dependence of the tunneling current on the distance. The origin of the x-axis corresponds to the tunneling set-point ($V_t = 2V, I_t = 100pA$). The slope of the logarithmic current is a measure of the decay constant β.

abruptly. The slope stays almost constant up to a distance of $0.75nm$ and increases again beyond this point.

The proportionality of $\ln(I)$ and d can easily be explained by the Simmons model. For low and intermediate voltages, equation (1.19) can be approximated by the simple exponential law (see equation (1.22))

$$I = G \exp(-\beta L_z) V \tag{4.4}$$

It follows for the logarithm of the current ($d = -L_z$)

$$\ln(I) = \ln GV + \beta d \tag{4.5}$$

i.e. the slope or derivative of the function $\ln(I) = f(d)$ is a direct measure of the decay constant β. However, in the STM measurement setup the decay constant β is not constant over the entire length of the device. Three different parts of the device with different decay constants can be identified: the tunneling gap between the STM tip and the molecule (β_{Vac}), the biphenyl (β_{Ph}) and the alkane group (β_{CH}). Therefore,

equation (1.22) can be refined:

$$I = G \exp\left(-(\beta_{Vac} d_{Vac} + \beta_{Ph} d_{Ph} + \beta_{CH} d_{CH})\right) V \tag{4.6}$$

It is tempting to identify the different slopes of the IS curve of figure 4.13 with the decay constants β_{Vac}, β_{Ph} and β_{CH} of equation (4.6) and in the following it is discussed if this interpretation is justified. For the measurement shown in figure 4.13, this interpretation would lead to decay constants of $25.7nm^{-1}$ and $3.93nm^{-1}$ for the vacuum gap and the biphenyl unit, respectively. The decay constant of the alkane group cannot be extracted since the current amplifier limited the tunneling current to $100\mu A$, a value that was reached above $\sim 0.9nm$.

For β_{Vac}, this interpretation is certainly justified, since at this position of the tip, it moves through the vacuum gap and the slope of the function $\ln(I) = f(d)$ is the decay constant of vacuum β_{Vac}.

The other parts of the IS plot are more difficult to interpret. If the tip is pushed further toward the SAM, it will touch the surface of the SAM at a certain point and the decay constant will change. Therefore, the first kink in figure 4.13 at $0.07nm$ can be interpreted as the point at which the STM tip touches the SAM surface.

In analogy to the interpretation of the decay constant of vacuum, the slope of the function $\ln(I) = f(d)$ in the range beyond the contact point could be seen as the decay constant of the biphenyl group β_{Ph}. But pushing the STM tip further into the SAM after the contact point has been reached perturbs the SAM and changes the tunneling conditions to a certain extent. However, there are three observations that suggest that this perturbation is small. First of all, the slope of the logarithmic plot of the tunneling current, i.e. the decay constant β, is $4.7 \pm 0.8nm^{-1}$[2]. This value is right within the published decay constants for an unperturbed phenylene layer ($\sim 4 - 6nm^{-1}$ [58 60, 200|). Furthermore, this value of β stays constant over a distance of $0.605 \pm 0.9nm$ and rises again if the tip is pushed further into the layer. This distance is close to the thickness of the biphenyl group ($0.608nm$) if the tilt of 45° is taken into account. Therefore, the additional rise in slope for distances above 0.75nm can be seen to be due to the tip pushing through the biphenyl layer and reaching the alkane spacer chain. The last indication that the perturbation is small is the repeatability of the measurement. The IS plot as shown in figure 4.13 can be acquired at the same position of the SAM at least 10-20 times without changing the overall characteristic of the plot. Therefore, the slope of the function $\ln(I) = f(d)$ can indeed be interpreted as the decay constant of the molecule.

All these observations point to the conclusion that IS spectroscopy can laterally and *vertically* probe the decay constants of the SAM without significantly damaging the

[2]The error margins are the standard deviation of ten successive measurements.

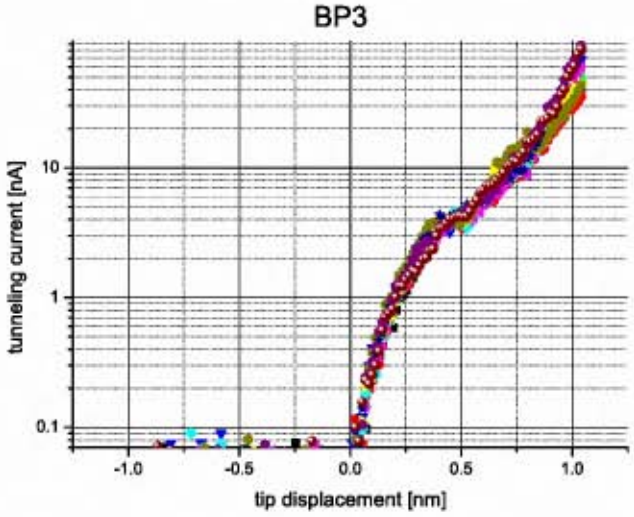

Figure 4.14: Current vs. distance spectroscopy for an odd numbered BPn molecule (n=3).

SAM. This interpretation is in accordance with the IS measurements of Yasutake et al. [201], who measured the current vs. distance dependency of SAMs of alkanethiols. They also observed two slopes in the logarithmic plot of the tunneling current and interpreted the slope of the current at positions where the tip penetrates the SAM as the decay constant of alkanes. By these measurements, they obtained a β_{CH} of 11-12 nm^{-1}, which is in close agreement to decay constants measured by Bumm et al. [52].

IS Spectroscopy of BP3

The result of a current vs. distance measurement for an odd numbered biphenylthiol (BP3) is shown in figure 4.14. Ten successive measurements are plotted. These measurements reassemble that of BP2 in figure 4.13 with one exception. Only two different slopes in the logarithmic plot are visible, which has been interpreted as being the decay constant of the vacuum and the biphenyl group. The additional rise in β for distances of above 0.75nm, which has been interpreted as being due to the tip pushing through the biphenyl layer and reaching the alkane spacer chain, is not visible. But this is in accordance with the conformation of the odd numbered BPn molecules. Whereas for n−even, the biphenyl group is tilted by approx. 45° out of the surface normal, for

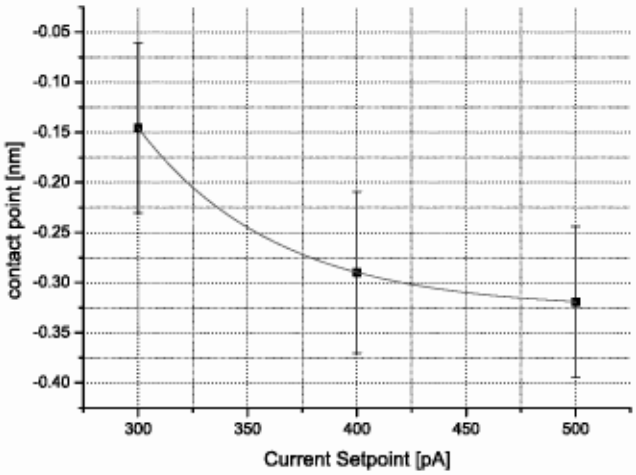

Figure 4.15: Dependence of the contact point on the tunneling set-point ($V_t = 0.2V$). The error bars correspond to 20 successive measurements. Increasing the current set-point moves the tip closer to the SAM.

n=odd, the biphenyl group is almost perpendicular to the surface (see figure 4.2(a)), thereby increasing the thickness of the biphenyl layer to ~ 8Å. Therefore, the tip cannot push through the biphenyl layer and reach the alkane spacer chain.

Adjusting the Vacuum Gap

Besides measuring the decay constants, IS spectroscopy has an additional application shown in figure 4.15. Considering that the first kink in the IS plot in figure 4.13 has been interpreted as the point where the tip touches the SAM, i.e. the contact point, IS spectroscopy is a method of measuring the size of the vacuum gap between the SAM and the STM tip. By changing the tunneling set-point, the size of the vacuum gap can be changed. This is shown in figure 4.15, where the contact point is plotted against the current set-point. The tunneling voltage is kept constant at $0.2V$. It can be seen that the contact point moves to the left in the IS plot, i.e. to increasingly negative values. This can be explained by the mode of operation of the STM. By increasing the current set-point, the tip is moved closer to the SAM and effectively shifts the whole IS curve to the left. Therefore, the contact point moves to the left in the IS plot.

4.4.3 Conclusion

Films of BPn have been electrically characterized. It is shown through IV spectroscopy that the current can be explained by a simple tunneling model as derived in section 1.3.1. No sharp features are observed either in the IV characteristics or in the plot of the differential conductance that would suggest a resonant transport across a molecular level.

It is shown that IS spectroscopy is a tool for measuring the decay constant of the SAM vertically resolved. The molecule is shown to be composed of three parts, each part with a different decay constant β. These parts are interpreted as the vacuum barrier above the SAM, the biphenyl unit and the alkane chain. The current tunnels through each of these parts and the overall current through the SAM is given by equation (4.6)

$$I = G \exp\left(-(\beta_{Vac} d_{Vac} + \beta_{Ph} d_{Ph} + \beta_{CH} d_{CH})\right) V$$

By these measurements the decay length β of the biphenyl unit is found to be $4.7 \pm 0.8 nm^{-1}$.

Chapter 5

Embedding Guest Molecules into an Alkanethiol SAM

After optimizing the bottom electrode and the alkanethiol self-assembled monolayer and after studying the current transport properties of BPn in full coverage SAMs, BPn is now embedded into an alkanethiol SAM.

The electrical characterization of the embedded molecules is experimentally more demanding than the characterization of full coverage SAMs as shown in sections 4.4.1 and 4.4.2. One method of measuring the current transport properties of embedded molecules is based on the Current Imaging Tunneling Spectroscopy (CITS) mode of the STM. In this mode, an image of the surface is scanned. In addition to the height information, at each pixel of the image an IV or IS characteristic of the film is taken. Thereby, the IV or IS characteristic can be directly mapped to the features of the surface, i.e. the IV or IS curves taken above the embedded molecules can be distinguished from the IV curves taken above the surrounding SAM.

A second method is based on the operational principle of the STM. If an SAM is scanned in the constant current mode, the height of the embedded BPn above the alkanethiol SAM does not solely represent the physical height of the BPn molecule, but is rather a combination of physical height and differences in the tunneling conductance between the embedded molecule and the surrounding SAM. Therefore, the current transport properties of BPn can be deduced simply from the height difference.

Compared to the CITS mode, the method, which is based on the height differences in STM images, has several advantages: The measurement of height differences in STM is more reliable than spectroscopic methods. For measuring an IV or IS characteristic, the feedback loop of the STM has to be switched off so that any drift of the piezo crystal that positions the STM tip cannot be controlled. Furthermore, during IS spectroscopy the STM tip necessarily pushes into the SAM, as discussed in section 4.4.2. It is argued that this perturbation of the SAM is small, but of course there is always an uncertainty

about the degree of perturbation. This uncertainty is avoided by the method based on the interpretation of the height differences. At last, the height difference between different domains of an SAM is unaffected by the specific shape of the STM tip. Whereas the absolute magnitude of the current in IV or IS measurements acquired with different tips is difficult to compare, for the measurement setup of mixed SAMs the influence of the tip is canceled out.

There are different methods of embedding specific molecules into a host SAM or, more generally, of preparing mixed SAMs that consist of multiple molecular species. These methods are described in the next section.

5.1 Mixed Self-Assembled Monolayers as a Tool for Molecular Electronics

As already mentioned in chapter 3, thiol based self-assembled monolayers (SAMs) are not only an effective tool for molecular electronics, but are more generally used as a method for tailoring the surface properties of metals [63, 115]. In particular, SAMs are used for wetting control [116–119], corrosion inhibition [120], protein adsorption [121], and lateral structuring [122]. For most of these applications, SAMs that consist of more than one component (mixed SAMs) are used, because they exhibit more degrees of freedom, i.e. the surface properties can be adjusted by the ratio of the different constituents of the film.

Mixed SAMs are especially promising for the application in this thesis, i.e. for measuring the electron transport properties of different molecules. Weiss et al. were the first to characterize electronic transport properties of single molecules via an STM setup by using mixed SAMs. A molecular wire candidate, a conjugated organic molecule, was diluted in an SAM of dodecanethiol [23]. Thereby, the molecular wire was shown to be indeed highly conductive compared to the alkanethiols.

There are several ways to prepare mixed SAMs. One method is to assemble the film from a mixture of different substances (coadsorption). Various mixed SAMs were realized using this approach: alkanethiols with different chain lengths [202, 203] and different terminal groups [203–205], as well as decanethiol and an amide-containing alkanethiol of similar length [206]. Bain et al. [203] showed that the composition of the monolayer does not fully correspond to the composition of the solution and that longer chains are preferentially adsorbed, which points toward thermodynamic control of the adsorption process. This was later confirmed by a theoretical study [207].

Another method of creating mixed SAMs is the adsorption of asymmetric disulfides [204, 208]. However, this process fixes the ratio of the two components to 0.5, thereby

limiting the advantage of continuously adjusting the surface properties in mixed monolayers by varying the ratio of the two components.

In contrast to the two above-mentioned methods, which always consist of a single deposition process, a two step deposition process is mainly used for isolating electrically active molecules in a host matrix [23, 209–216]. For this method, a preassembled, single component SAM (usually consisting of insulating alkanethiols) is dipped in a second step into a solution of the electronically active molecules. In this second step, molecules of the host matrix are replaced by the active molecules. It was shown that this process mainly takes place at defects in the host matrix [23, 209, 210]. Studies on the insertion of linear conjugated molecules showed that the amount of molecules incorporated into the monolayer is a function of immersion time [210]. The rate determining step is the replacement of host molecules by molecules from the second molecular solution.

Depending on the preparation technique and the molecular species used, the monolayers are either homogeneously mixed or the different molecules segregate into separate domains. For some applications uniformly mixed monolayers are preferred so that a kinetically trapped method for preparing truly molecular-scale mixed SAMs has been developed [202]. Similarly, the deposition of mixed monolayers from asymmetrical disulfides results in uniform mixed layers [204, 208]. In most of the molecular electronic studies that measure the electronic transport along a molecular wire, the electronically active molecules are rather isolated in the host matrix instead of being surrounded by a segregated domain of the same molecule [23, 209–211, 213, 214]. In some of these studies, the apparent height in the STM images of the molecules above the host matrix is related to the current transport properties. This is possible as the STM height does not solely reflect the physical height of the molecule, but also comprises the transconductance of the molecule.

Biphenylthiols are ideal substances for insertion into an alkanethiol host matrix. Compared to the conjugated molecules used by Bumm et al. [23], BPn can better adapt to the alkanethiol lattice due to the higher flexibility of the alkane chain. This is particularly important in the rate-determining exchange step of alkanethiols by biphenylthiols. As described above, the height difference of these domains measured by STM can be interpreted as a combination of physical height difference and difference in transconductance of the molecules. Compared to the structurally very similar molecules used by Ishida et al. (4-biphenylmethanethiol, [215, 216]), BPn and C12 have the same top and bottom group, which simplifies the interpretation. Therefore mixed SAMs consisting of insulating dodecanethiol (C12) and BPn are prepeared by a two step process with the aim of characterizing the current transport through biphenylthiols.

5.2 Experimental Details

Following most molecular electronic studies, the mixed SAMs used in this thesis are prepared in the two step deposition process. Before turning to mixed SAMs of alkanethiols and BPn, in first experiments alkanedithiols are embedded into an alkanethiol SAM. These prelimary studies serve as a test setup on which fundamentals of the deposition process are studied.

Alkanethiols, alkanedithiols and absolute ethanol are purchased from Aldrich and used as received. Analytically pure BPn is synthesized according to Buck et al. by Grignard C-C coupling reaction of the corresponding phenyl- or alkylbromide followed by the conversion of the bromide into the thiol via thiourea [187]. Characterization of the BP4 is done by NMR, massspectrometry and elemental analysis[1].

Gold films are deposited onto mica by the standard procedure developed in chapter 2, which results in (111)-oriented gold films with large terraces [88]. Dodecanethiol (C12) is deposited by the solution based growth described in chapter 3, i.e. the gold films are dipped into a 1mM ethanolic solution of dodecanethiol overnight. Alkanedithiols or BPn are inserted by immersing the single component SAM of C12 for several minutes into a solution of the alkanedithiol or BPn.

The films are characterized by Ultrahigh Vacuum Scanning Tunneling Microscopy (UHV-STM, JEOL JSPM 4500) at a base pressure of $\mathbf{3 \times 10^{-10}}$mbar. Home made tungsten STM tips are used. All STM scans are taken in constant current mode.

5.3 Mixed SAMs of Alkanethiols and Alkanedithiols

Before mixed SAMs of alkanethiols and BPn are examined, the embedding of alkanedithiols into an SAM of dodecanethiol (C12) is studied [155].

Figure 5.1 shows an SAM of C12 with embedded octanedithiols. The octanedithiols are embedded by immersing the preassembled C12 film into a 1mM solution of octandithiol for 10min. The characteristics of an alkanethiol SAM as described in chapter 3 are clearly visible. The film possesses monoatomic gold vacancy islands visible as holes in the surface. Furthermore, different domains of C12 are visible by different directions of the reconstruction lines of the c(4x2) structure of C12 on gold (111).

In addition to these features, which are also visible in SAMs consisting of a single molecular species, there are several bumps or hills in the surface (see white arrows in figure 5.1). These hills are absent in pure C12 SAMs and are therefore interpreted as embedded octanedithiols.

At first sight, it is surprising that the octanedithiols appear as hills in the SAM

[1]The synthesis was done in the group of Prof. U. Simon at the Institute of Inorganic Chemistry at RWTH Aachen.

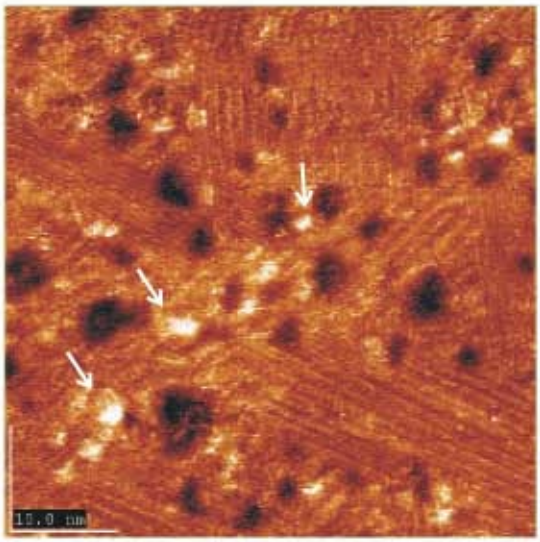

Figure 5.1: SAM of dodecanethiol with embedded octanedithiols (white arrows). The size of the image is $\mathbf{50 \times 50 nm^2}$, the tunneling voltage was $\mathbf{0.2V}$ and the tunneling current was set to $\mathbf{200pA}$.

image and not as depressions, although octanedithiol is $\sim$ **3.4**Å shorter than C12. However, as already discussed in section 5.1, the apparent height in STM scans is always a combination of real height information and changes in the tunneling conditions. The additional -SH group at the terminal of octanedithiol notably changes the tunneling conditions and in particular the contact conductance G (see equation 1.22), so that the dithiols appear higher than the surrounding C12 SAM.

The hills in figure 5.1 have a diameter of $\mathbf{2-3}$nm so that it can be estimated that each hill consists of 14-30 dithiols, assuming an area of $\mathbf{0.216nm^2}$ per molecule as for the $(\sqrt{3} \times \sqrt{3})$ structure. However, the lateral dimensions of the hills as measured by STM will always be exaggerated due to the imperfect shape of the STM tip. Therefore, the number of 14-30 molecules is only an upper bound; the real number will be lower.

The upper -SH group of the dithiols provides an additional functionality of the SAM. The dithiols as shown in figure 5.1 can be contacted by gold nanocluster by gold-sulfur bonding, thereby providing a symmetrical contact of the molecule.

5.3.1 Contacting Dithiols with Gold Nanoclusters

To contact the dithiols by a gold nanocluster, the mixed SAM is immersed into a solution of gold clusters. An STM scan of the resulting film is shown in figure 5.2. This film

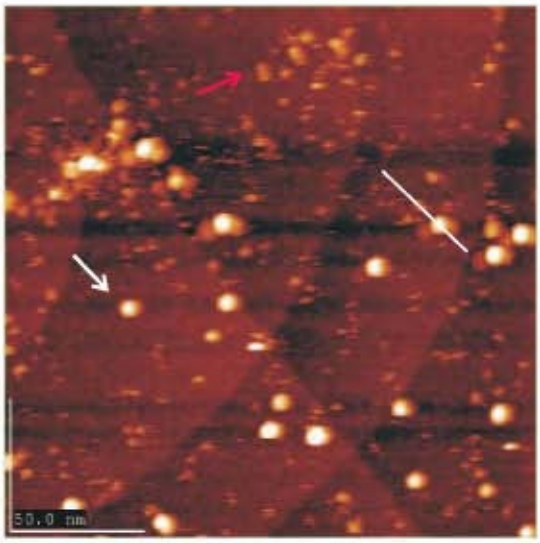

(a)

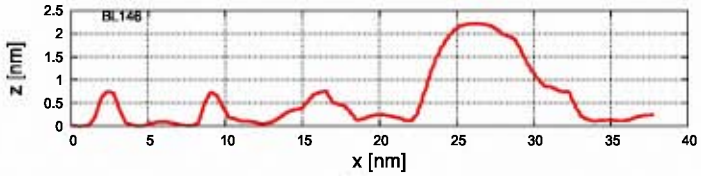

(b)

Figure 5.2: (a) $200 \times 200 nm^2$ STM scan ($V_t = 2V, I_t = 5pA$) of decanedithiols embedded into dodecanethiols and contacted via Au55 clusters. The lower protrusions are unbound dithiols (red arrow) and the large protrusions are the Au55 gold cluster (white arrow). (b) is a cross section along the white line in (a).

consists of decandithiols embedded into dodecanethiols and contacted by Au55 clusters[2] by immersing the film into a 100nM solution of Au55 in water for 15min. During immersion, the gold clusters selectively bind to the top -SH groups of the decanedithiols. Following deposition, the film is thoroughly rinsed to wash away physisorbed gold clusters.

In the STM scan of the resulting film (figure 5.2(a)), the terraces of the underlying gold film are still visible. More interestingly, two kinds of protrusions are visible: large, round protrusions with a height of $\sim 2nm$ and smaller and lower protrusions (height

[2]Clusters consisting of 55 gold atoms, stabilized by a ligand shell of triphenyl-phosphin molecules. The gold nanoclusters were prepared at the Institute of Inorganic Chemistry at the RWTH Aachen (Prof. U. Simon).

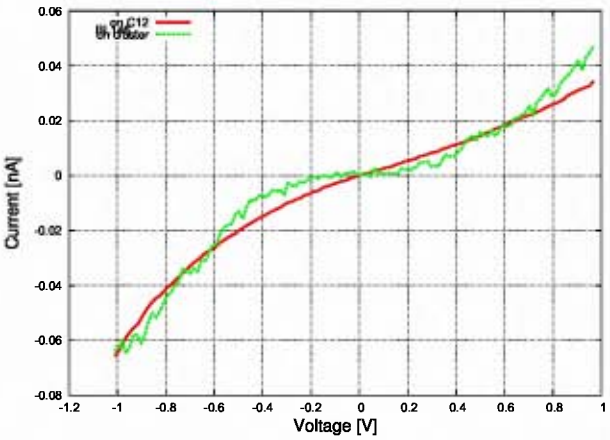

Figure 5.3: IV characteristic of the sample shown in figure 5.2 ($V_t = 1.5V, I_t = 50pA$). The red line is the current above the C12 layer, whereas the green line shows the current through the gold cluster. The current through the gold cluster is suppressed for voltages below $|V| < 0.2V$, which can be interpreted in terms of a Coloumb blockade.

$\sim 0.5 - 0.6nm$, see also the cross section in figure 5.2(b)).

The height of the large protrusions is almost identical to the diameter of the gold cluster (including the ligand shell, the cluster have a diameter of 2nm) and can therefore be interpreted as gold clusters, which are bound to the dithiols. Laterally, the clusters have a diameter of 7nm, but as in the discussion of figure 5.1, this diameter is exaggerated compared to the real diameter.

The lower protrusions have the same diameter as the dithiols in figure 5.1 (1.4nm−3.1nm) and are most probably decanedithiols that are not bound by a gold cluster. As in the preceding section, it can be estimated that these protrusions consist of 8 to 35 molecules [155].

5.3.2 Electrical Characterization

Placing a gold cluster on top of the decanethiol is a perfect method of providing a stable contact to the dithiol. To measure the current through the dithiol and gold cluster, the STM tip is placed above the gold cluster and the IV-characteristic is measured, similar to the measurements on full coverage layers in section 4.4.1. However, in contrast to the measurements shown in section 4.4.1, the position of the tip has to be exactly placed above the gold cluster. This is accomplished by scanning in the Current Imaging Tunneling Spectroscopy (CITS) mode of the STM, as described in the introduction to this chapter.

The result of such a CITS scan is shown in figure 5.3. The tunneling set-point is $V_t = 1.5V$ and $I_t = 50pA$. The IV characteristic of the C12 layer is shown in red, whereas the IV characteristic above a gold cluster is shown in green.

The current above the C12 layer is qualitatively identical to the IV plots measured above a full coverage BP2 layer (compare figure 4.12(a)) and can therefore be explained by a simple tunneling model. However, the current above the gold cluster deviates in a very interesting manner. The current above the gold cluster is suppressed for voltages below $|V| < 0.2V$. Above $0.2V$, the current rises exponentially and shows the same characteristic as the C12 layer.

Coulomb Blockade

The suppression of the current through the gold cluster and the dithiols can be explained by the Coulomb blockade effect. The basic idea of the Coulomb blockade is as follows: The gold cluster above the gold substrate forms a small capacitance, which can only be charged by multiplies of the elementary charge e. Due to the small capacitance, a relatively large energy is needed to bring one electron onto the cluster. Below this energy no electron can tunnel to the cluster and the current is suppressed.

To determine the minimum energy needed to charge the gold cluster, the tip/cluster/dithiol/electrode assembly is approximated by the equivalent circuit shown in figure 5.4. There are two capacitors: The capacitance between the tip and the gold cluster C_1 and the capacitance between the gold cluster and the gold bottom electrode C_2 (see figure 5.4(b)). Electrons can tunnel onto the cluster either from the tip or from the gold electrode.

The charge on the gold cluster Q is the difference of the charge on C_2 and C_1

$$Q = Q_2 - Q_1 = C_2V_2 - C_1V_1 = -ne \tag{5.1}$$

with V_1 and V_2: voltages across capacitance C_1 and C_2, Q_1 and Q_2: charge on C_1 and C_2 and $n \in \{0, 1, 2 \ldots\}$.

Equation 5.1 expresses the fact that the capacitance can only be charged by multiplies of e. The voltages across C_1 and C_2 are

$$V_1(n) = \frac{C_2V_t + ne}{C_1 + C_2} \tag{5.2}$$

$$V_2(n) = \frac{C_1V_t - ne}{C_1 + C_2} \tag{5.3}$$

Depending on the number of electrons n on the cluster the electrostatic energy E_s

stored in the capacitors is

$$E_s(n) = \frac{Q_1^2}{2C_1} + \frac{Q_2^2}{2C_2} = \frac{C_1C_2V_t^2 + (ne)^2}{2(C_1 + C_2)} \tag{5.4}$$

For charging the gold cluster with a single electron, the following energy has to be supplied

$$\Delta E = E_s(1) - E_s(0) = \frac{e^2}{2(C_1 + C_2)} \tag{5.5}$$

The gold cluster is charged if the energy, which is supplied by the voltage source to one of the capacitances C_1 or C_2, is larger than the energy difference ΔE, i.e. if $eV_1 > \Delta E$ or $eV_2 > \Delta E$. In the following, it is assumed that the capacitance between the tip and the gold cluster is larger than the capacitance between the gold cluster and bottom electrode ($C_1 < C_2$). This is certainly justified as the vacuum gap is much smaller than the length of decanedithiols (see figure 4.13). Therefore, the voltage drop is larger at C_2 than at C_1 (see equation 5.2) and it follows

$$e\frac{C_1V_t}{C_1 + C_2} > \frac{e^2}{2(C_1 + C_2)} \tag{5.6}$$

$$V_t > \frac{e}{2C_1} \tag{5.7}$$

Below $|V_t| = \frac{e}{2C_1}$, no electron can tunnel to the gold cluster and consequently the current is suppressed in this region. By approximating the tip/gold cluster capacitance C_1 by a plate capacitor and using the charging voltage of 0.2V as seen in figure 5.3, one can estimate the size of the vacuum gap as being ~ 0.7Å, i.e. the tip is just above the gold cluster.

Therefore, the current vs. voltage characteristic as shown in figure 5.3 can be explained by the Coulomb blockade effect of the gold cluster. However, this interpretation reveals a drawback of the method of contacting a molecule with a gold cluster. The measured IV curve is in large parts determined by an effect of the gold cluster and not of the molecule. In fact, all characteristics of the molecule within the Coulomb blockade are suppressed. The threshold voltage V_t could be lowered by using larger gold cluster (e.g. with a diameter of 5nm), but then the number of contacted molecules would be increased. Therefore, in later experiments, the molecules are not contacted by a gold cluster.

In conclusion, it is shown that alkanedithiols can be embedded into a C12 alkanethiol SAM. Immersing a preassembled C12 film into a 1mM solution of alkanedithiols for 10min yields embedded single or at least embedded bundles with a low number of molecules. The upper -SH group of the dithiols can be contacted by a gold cluster. The current vs. voltage characteristic of embedded alkanedithiols contacted by gold clusters

show a suppression of the current for voltages below 0.2V, which can be explained by the Coulomb blockade effect.

5.4 Mixed SAMs of Alkanethiols and BPn

The experiments on embedding dithiols into an alkanethiol SAM have provided a good basis for studies of other embedded molecules, i.e the characterization of embedded BPn molecules. Due to its similar length to dodecanethiol, BP4 is used from the homologous series of BPn.

5.4.1 Embedding BP4 Molecules in a C12 SAM

Figure 5.5(a) shows an STM scan of a C12 SAM with embedded BP4. The C12 SAM is grown by immersing the film for 24h in 1mM ethanolic solution of C12. The BP4 molecules are embedded by dipping the preassembled C12 film into a 100μM solution of BP4 for 10min at room temperature.

The resulting film is very similar to the SAM of embedded dithiols shown in figure 5.1. Apart from the gold vacancy islands, small protrusions are visible on the surface, which are interpreted as embedded BP4 molecules. These protrusions have a diameter of 1-3nm, leading to the estimation that these hills are composed of less than 30 BP4 molecules.

In principle, the height difference between the embedded BP4 molecules and the C12 SAM can be interpreted in terms of current transport properties of the molecules. Therefore, the distribution of heights of BP4 is shown in figure 5.5(b). From this distribution, the median height of the molecules can be estimated to be 1.8Å.

However, for an exact interpretation of the height of BP4 and in order to gain some insight into the electric properties, there is a fundamental problem. The exact conformation of embedded single molecules or embedded bundles of molecules as in figure 5.5(a) is mainly unknown and only a few studies have addressed this question [210]. Furthermore, the molecules are inserted at a variety of defects in the host matrix, which may affect the electrical properties of the molecules. This lack of information makes an exact interpretation of the current transport along these molecules difficult.

5.4.2 Growing Domains of BP4

In contrast to embedded single molecules or to bundles of a small number of molecules, the structure and conformation of molecules in full coverage SAMs is studied in more detail [63, 187] (compare chapter 3 and 4). These structures will prevail in phase segregated mixed SAMs if the domains are large enough so that the STM height difference

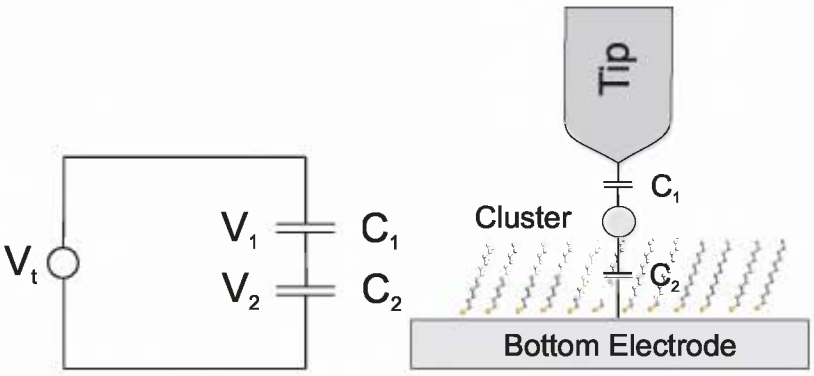

(a) (b)

Figure 5.4: Equivalent circuit of the electrical measurements shown in figure 5.3. The device consists of two capacitors: the capacitance between the STM tip and the gold cluster and the capacitance between the cluster and the bottom electrode.

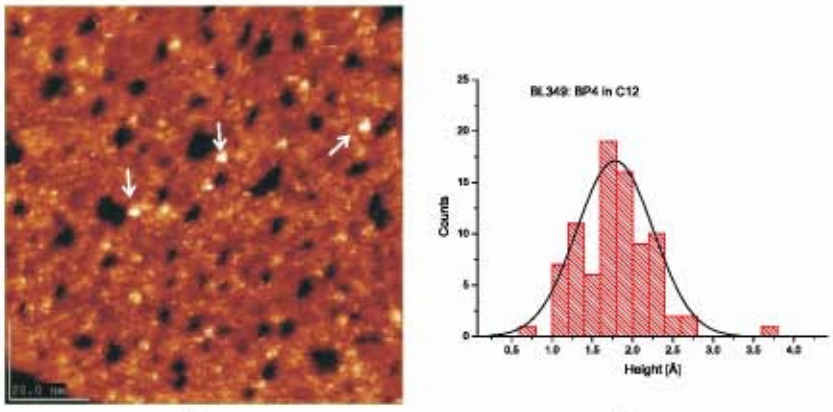

(a) (b)

Figure 5.5: (a) $100 \times 100nm^2$ STM scan of a C12 SAM with embedded BP4. The BP4 molecules are visible as protrusions (see white arrows). (b) shows the distribution of the height of BP4 molecules above the C12 SAM. The mean height is 1.8Å.

between separate domains in a mixed SAM can be interpreted in terms of transconductances of the different molecules without having the uncertainties of measurements on embedded single molecules |52|.

Structural properties

In figure 5.6, STM images of a mixed SAM consisting of C12 and BP4 are shown. To increase the number of embedded BP4 molecules and to cause phase segregation (i.e. separate domains of BP4 and C12), the insertion time is increased to 20min and the solution is heated to 70°C. In the large area scan (figure 5.6(a)) several gold terraces are seen that are covered by separate domains of BP4 and C12. Domains of BP4 and of C12 can be distinguished by the high resolution scan shown in figure 5.6(b). In this scan, domains that apprear lower are molecularly resolved and especially in the domains in the upper left corner, the c(4x2) structure of alkanethiols on gold can be seen (white arrows). Therefore, the domains that appear lower can be assigned to C12. Additionally, in the large area scan deep pits corresponding to a monoatomic gold step are seen, characteristic of SAMs of thiols on gold (white arrows in figure 5.6(a)) |167|. These holes are mostly surrounded by domains of BP4. Similarly, at domain boundaries of different C12 domains, islands of BP4 start to grow (black arrows in figure 5.6(a) and 5.6(b)), indicating that domain boundaries of the host matrix and pits in the gold surface act as nucleation points for BP4 domains. This confirms the results of Cygan and Weiss et al. for other electronically active molecules [209]. However, most BP4 domains in this and later measurements grow around pits so that the exchange of C12 molecules by BP4 molecules seems to be more effective at these defect sites.

In contrast to domains of C12, BP4 domains exhibit a rather amorphous texture. To increase the order in these films, the samples are annealed at 64°C in vacuum for several hours. An STM scan of the resulting film after 1h30min is shown in figure 5.7(a) and after 3h 45min in figure 5.7(b). The appearance of the BP4 islands changes from an amorphous (figure 5.6) towards a more textured shape, indicating a higher order in these films. This suggests that there is some rearrangement in the BP4 films, which should result in a change in the height difference of the BP4 and C12 domains.

To survey the height differences before and after annealing, it is evaluated as follows. From STM scans such as those shown in figure 5.6 and 5.7, the histogram of the height of each image pixel is taken (figure 5.8). These histograms display two distinct peaks: the lower one for the height of the C12 domains, the higher one for the BP4 domains. Both peaks are fitted to a Gaussian distribution and the difference in the center positions of the peaks is taken as the mean height difference of the BP4 and C12 domains. This kind of analysis is conducted for several scans, yielding the height differences shown in figure 5.9. The height difference slightly decreases from $0.14 \pm 0.045nm$ without heating to

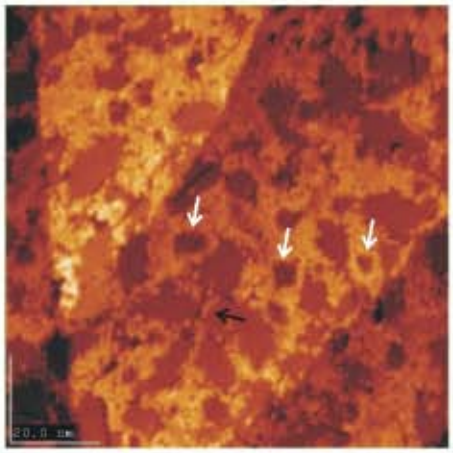

(a)

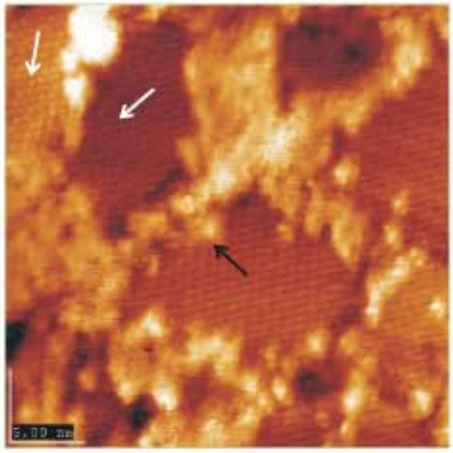

(b)

Figure 5.6: $100 \times 100nm^2$ STM (a) and $30 \times 30nm^2$ (b) STM scans of a C12/BP4 mixed monolayer. The film shows separate BP4 and C12 domains. Domains that appear higher consist of BP4. In the high resolution scan, the c(4x2) structure of C12 is visible (white arrows in b). Black arrows mark nucleation of BP4 domains at C12 domain boundaries. The white arrows in (a) mark nucleation of BP4 domains at holes in the gold surface.

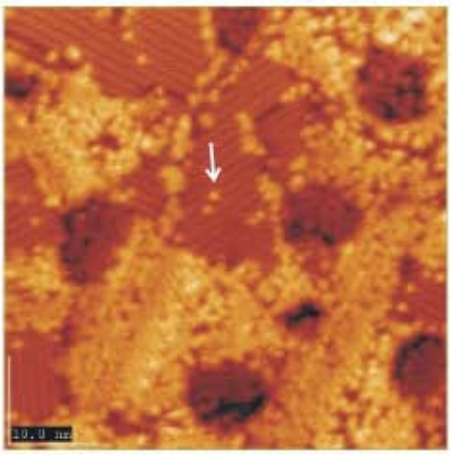

(a)

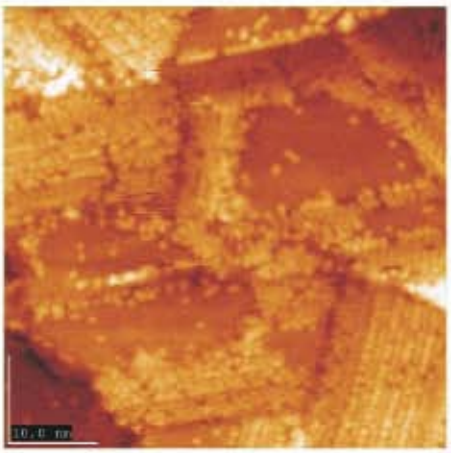

(b)

Figure 5.7: $50 \times 50 nm^2$ scans of a mixed C12/BP4 monolayer annealed at 64°C for 90min (a) and 225min (b). An increase in structural order of the BP4 domains is visible in the texture of these domains. The white arrow in (a) marks a BP4 molecule inserted in the middle of a C12 domain.

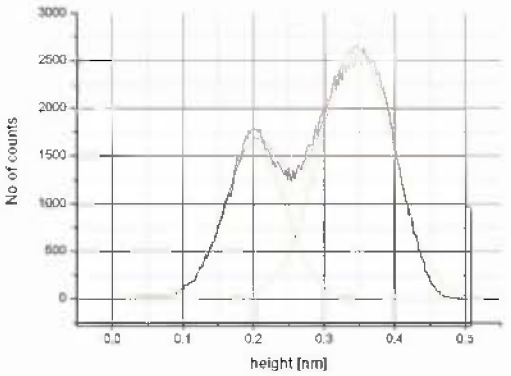

Figure 5.8: Height distribution of an STM scan of a mixed C12/BP4 monolayer. Two peaks are visible, which correspond to the different heights of the different domains. The distance of the center of these peaks is taken as the mean height difference of the C12 and BP4 domains.

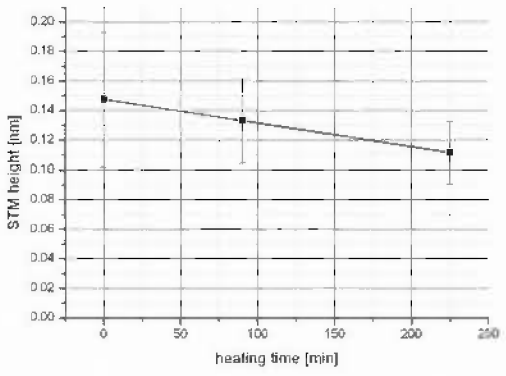

Figure 5.9: Height difference of BP4 and C12 domains depending on annealing time.

$0.133 \pm 0.03nm$ after 90min and $0.11 \pm 0.021nm$ after 3h45min of annealing. The C12 domains already exhibit their final c(4x2) structure before heating, making a strong rearrangement of the alkanes less probable. Therefore, most of the change in height difference should result from an increase in order in the BP4 domains.

A closer look at figure 5.7(a) reveals another interesting property of the mixed C12/BP4 film. Some BP4 molecules are not incorporated into the film at defect sites such as domain boundaries and pits in the gold surface, but into the middle of a C12 domain (see white arrow in figure 5.7(a)). However, this process has a much lower probability than insertion at defect sites.

Figure 5.10 shows a zoom of an area in which BP4 molecules are inserted into a C12 domain. BP4 molecules appear as protrusions. Also visible is the c(4x2) structure of the underlying C12 structure providing a coordinate system to measure the lateral dimensions of the embedded molecules. All protrusions appear to be smaller than one unit cell of the $(3 \times 2\sqrt{3})$ structure (equivalent to the notation c(4x2), see white box in figure 5.10), which consists of four C12 molecules per unit cell. This leads to the estimation that the protrusions consist of less than four BP4 molecules. Considering the relatively larger occupied area per molecule for BP4 than for C12 and the fact that the STM image is a convolution of the imperfect STM tip shape and surface geometry, the estimation of four molecules can be taken as an upper limit. Furthermore, since all islands of BP4 molecules inserted into the C12 domains have the same lateral size, it is proposed that these protrusions consist of only single molecules.

As already pointed out above, the c(4x2) structure of C12 provides a coordinate system to determine the lateral size and position of the embedded BP4 molecules. This is especially advantageous for the study of diffusion processes of BP4 molecules within the C12 domains. Figures 5.11(a)-5.11(c) show a scan of the same sample area and provide a comparison of this area 10min and 16min after the initial state. For example, one inserted molecule is marked by a white arrow. It can be seen that the inserted molecules are fixed at their insertion place and do not diffuse. This observation is in agreement with the observation by Cygan et al. for more rigid conjugated oligomers [209]. Even the higher flexibility of biphenylthiols compared to the molecules used by Cygan et al. does not increase the mobility or diffusion rate of the molecules in the C12 host matrix. However, this low mobility at room temperature is a prerequisite for embedding single molecules into a C12 host matrix, since a high diffusion constant would lead to diffusion of the isolated molecules to BP4 domains and single embedded molecules would become unstable.

The mixed monolayer presented here is a system in which both different BP4 and C12 domains as well as single BP4 molecules embedded into C12 domains exist. These STM scans give a unique possibility of comparing the structure of the BP4 domains,

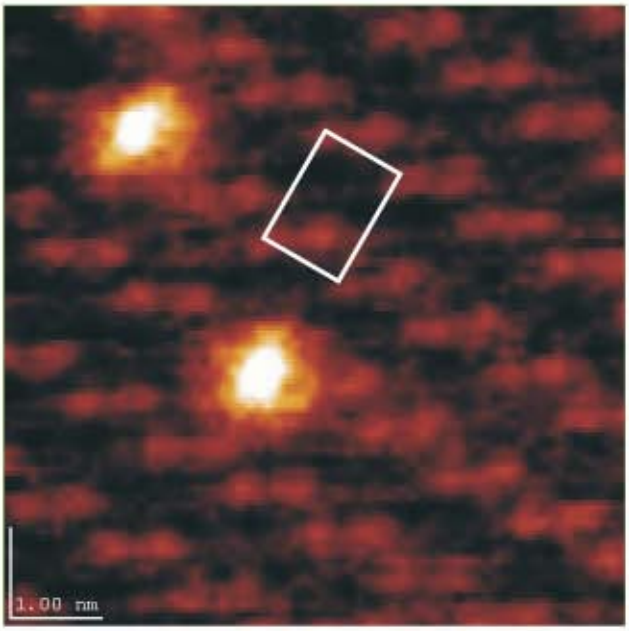

Figure 5.10: Zoom of BP4 molecules inserted into a C12 domain. The red box marks the $(3 \times 2\sqrt{3})$ unit cell of C12 (equivalent to the notation c(4x2)).

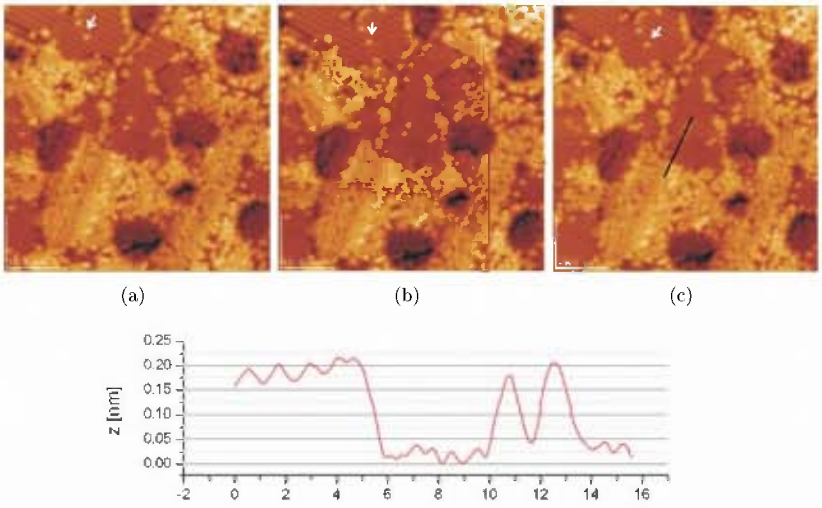

Figure 5.11: STM scan of the surface area at beginning (a) and after 10min (b) and 16min (c). No movement of BP4 molecules inserted into C12 domains is visible (see white arrow). Part (d) shows a cross section along the black line in (c). The inserted single molecules have almost the same height as the BP4 domains.

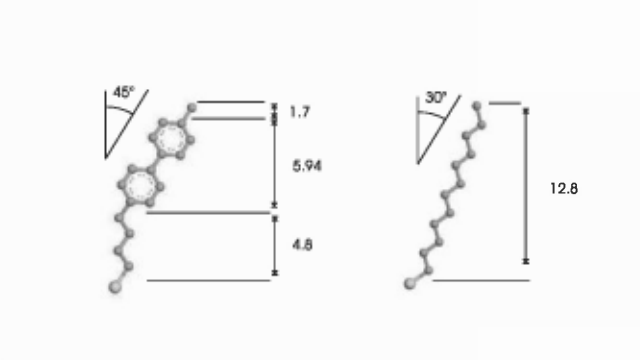

Figure 5.12: Conformation of BP4 and C12 in a full coverage SAM. The lengths are given in Angstrom.

which will approach the structure of full coverage BP4 monolayers, with single embedded molecules. As can be seen in the cross section in figure 5.11(d), the embedded molecules show almost the same height as the domains of BP4. This is an indication that the embedded molecules adopt the same conformation as the molecules in full coverage SAMs.

Electrical Characterization

As already mentioned in section 5.1, the height difference between the BP4 domains and the C12 layer can be interpreted in terms of different transconductances of these molecules [52].

For the following discussion, the conformation of BP4 as shown in figure 5.12 is assumed. The biphenyl group is tilted by 45° out of the surface normal, whereas the alkane chain has a rather upright orientation (see section 4) .

The conductance of a molecular wire can be expressed by equation (1.22) [52, 217]

$$G = G \exp(-\beta d) \tag{5.8}$$

with G: contact resistance, β: molecule dependent decay constant and d: molecular length.

Decay constants of alkanethiols have been measured by various methods [24, 52–57], but less data exists for the decay constant of phenylenes [58–60, 200]. As shown in section 4.4.2, BP4 consists of an alkane and a biphenyl part, so that the exponential term in equation (5.8) is split into an alkane dependent and a phenyl dependent part

(compare equation (4.6)):

$$I = G \exp\left(-\beta_{Ph} d_{Ph} - \beta_{CH} d_{CH}\right) V \tag{5.9}$$

with β_{CH}, β_{Ph}: decay constants of alkane chain and phenylene rings and d_{CH}, d_{Ph}: length of alkane chain and biphenyl group.

For a quantitative interpretation, the vacuum gap above C12 and BP4 domains has to be included

$$G_{Vac} = G_{0,Vac} \exp\left(-\beta_{Vac} d_{Vac}\right) \tag{5.10}$$

In general, the parameters $G_{0,Vac}$ and β_{Vac} can be different above C12 and BP4 (leading to parameters $G_{0,Vac,C12}, G_{0,Vac,BP4}, \beta_{Vac,C12}, \beta_{Vac,BP4}$). However, BP4 and C12 have the same top and bottom group, so that differences in the parameter of the vauum gap will be small. Therefore, it is assumed that $\beta_{Vac,C12} = \beta_{Vac,BP4}$. Following the experiments of Ishida et al. [215], this assumption is valid even without the top methyl group of BP4. Ishida et al. measured the increase in local barrier height (LBH) between a nonanethiol (C9) SAM and 4-biphenylthiol and 4-biphenylmethanethiol. Especially the latter molecule is almost identical to BP4, but does not possess the upper methyl group. Ishida et al. observed that the LBH increases only by 0.24eV for 4-biphenylmethanethiol and by 0.84eV for 4-biphenylthiol. The LBH Φ is connected with the decay constant by

$$\Phi = 0.952 \left(\beta_{Vac}\right)^2 \tag{5.11}$$

with Φ: LBH in eV, β_{Vac}: decay constant of vacuum in Å^{-1}

Using the literature value $\beta_{Vac} \approx 23\text{nm}^{-1}$ [52], the error made by the approximation $\beta_{Vac,C12} = \beta_{Vac,BP4}$ is less than 8%.

Including the vacuum gap, the tunnel conductance above C12 and BP4 domains can be rewritten in the form of equation (4.6):

$$G_{BP4} = G_{0,BP4} \exp\left(-\left(\beta_{Vac} d_{Vac,BP4} + \beta_{Ph} d_{Ph} + \beta_{CH} d_{CH,BP4}\right)\right) \tag{5.12}$$

$$G_{C12} = G_{0,C12} \exp\left(-\left(\beta_{Vac} d_{Vac,C12} + \beta_{CH} d_{CH,C12}\right)\right) \tag{5.13}$$

Measuring in constant current mode implies $G_{BP4} = G_{C12}$ leading to:

$$\beta_{Ph} = \frac{\ln\left(\frac{G_{0,BP4}}{G_{0,C12}}\right) + \beta_{CH}(d_{CH,C12} - d_{CH,BP4}) - \beta_{Vac}(d_{Vac,BP4} - d_{Vac,C12})}{d_{Ph}} \tag{5.14}$$

The difference in vacuum gap $\Delta h_{gap} = d_{Vac,BP4} - d_{Vac,C12}$ relates to the observed STM height Δh_{STM} and the physical height difference between BP4 and C12 Δh_{phys} as follows:

$$\Delta h_{gap} = \Delta h_{phys} + \Delta h_{STM} \tag{5.15}$$

BP4 and C12 have the same top and bottom groups and are scanned with the same tunneling tip. Therefore, it is assumed that $G_{0,BP4} = G_{0,C12}$, i.e. that BP4 and C12 have the same contact resistances. Wold et al. measured the contact resistances of alkanethiols and phenylenes and stated that the contact resistances are indistinguishable within their experimental errors [60]. Probably, this approximation works so well because only the logarithm of the ratio $\frac{G_{0,BP4}}{G_{0,C12}}$ enters the equation so that any error made by this approximation is small compared to the other summands. The same approximation was also applied by Moth Poulsen et al. [213], Szumacher Blum et al. [214] and for the homologous series of alkanethiols by Bumm et al. [52].

The literature values of β_{CH} are around unity [24, 52–57] (ranging from 0.7 $Å^{-1}$-1.2 $Å^{-1}$), so that a value of $\beta_{CH} = 1$ $Å^{-1}$ is chosen. The decay constant of vacuum is taken as $\beta_{Vac} \approx 2.3 Å^{-1}$ [52]. Using these values and the lengths given in figure 5.12, it follows $\beta_{Ph} = 0.5$ $Å^{-1}$. These values agree with the experiments by Wakamatsu et al. [58, 59](0.53 $Å^{-1}$ for STM and $0.55 Å^{-1}$ for AFM experiments) and is slightly lower than the values measured by Holmlin et al. [200], who found a decay constant of 0.67 $Å^{-1}$ by mercury droplet measurements and slightly higher than the values measured by Wold et al. [60](0.42 $Å^{-1}$ for AFM experiments) implying that the rather rough approximations applied seem to be justified. In this way, the apparent STM heights can be explained in terms of a higher tunneling conductance of BP4. Assuming tunneling through bond or through space leads to decay constants β_{Ph} within the variation of values found in literature.

5.5 Conclusion

Dithiols and biphenylthiols (BP4) are embedded into a C12 SAM. The dithiols are additionally contacted by a gold nanocluster and the current across these devices is explained by the coloumb blockade effect.

At first, biphenylthiols (BP4) are embedded as single molecules or in bundles of a few molecules. However, a quantitative interpretation of the height difference between BP4 and the surrounding C12 SAM is not possible since the conformation of BP4 embedded into C12 is unknown.

Therefore, by changing the deposition conditions, SAMs consisting of phase segregated BP4 and C12 domains are produced. It is shown that domain boundaries and pits in the gold surface act as nucleation points for BP4 domains. Annealing the film at 64°C results in a higher order of the BP4 domains and a slight decrease of the height of BP4 domains above C12.

For the experimental conditions discussed, some BP4 molecules are found to be inserted into the middle of a C12 domain. The size and position can be determined by using the underlying c(4x2) structure of the alkanethiols as a coordinate system.

Thereby, it is shown that the protrusions in the C12 domains contain less than four molecules and are most probably due to single embedded BP4 molecules. Furthermore, these molecules are fixed in the C12 structure and do not migrate at room temperature. Comparing the height of the embedded molecules with the height of the BP4 domains, it is proposed that the embedded single BP4 molecules have the same conformation as in the full coverage phase.

The height difference of the domains of BP4 compared to the C12 SAM is explained in terms of a higher tunneling conductance of BP4. A simple two-layer model is proposed by means of which the current transport through the BP4 group is discussed and the decay constant β_{Ph} is deduced.

By these experiments, the nanodevice as described in the introduction (section 1.5) is completed. The current transport properties of this device have been measured and have been described by a simple tunneling model. Within this model, the device is divided into three parts: the alkane chain, the biphenyl group and the vacuum gap. Therefore, the conductance of BPn can be determined by equation (4.6).

$$G_{BPn} = G_0 \exp\left(-(\beta_{Vac} d_{Vac} + \beta_{Ph} d_{Ph} + \beta_{CH} d_{CH})\right) \tag{5.16}$$

In conclusion, a brief comment will be made on the use of BPn for molecular electronics. In the absence of any further functionality, like a negative differential resistance as for the so-called Tour Wires [26–28] or two conduction states which could be employed as a building part for molecular memories, BPn can only be used as a molecular wire. But is this molecule conductive enough?

The answer to this question is twofold. Of course, BPn is more conductive than alkanethiols. This can be drawn from the fact that BP4 appears higher in STM images than C12, although its physical height is slightly shorter than C12. Therefore, in the interpretation of Bumm et al. [23] BPn is a conductive molecular wire.

However, although BPn is more conductive than alkanethiols, the current transport through this molecule is still characterized by a tunneling transport with a decay constant of $\beta \approx 5\text{nm}^{-1}$ of the biphenyl part. This decay parameter is, of course, still much too large to justify the BPn molecules being considered as a "conducting" molecular wire. The problem lies in the large HOMO-LUMO gap of the molecule. In our measurement setup it has not possible to access the HOMO or the LUMO, which would lead to a sharp increase in the conductance. Voltages of above 3V have to be applied, which lead to the destruction of the sample. Therefore, to obtain a real molecular wire, the BPn molecules will have to be chemically modified, i.e. by increasing the number of phenylene rings [199], to decrease the gap between HOMO and LUMO and to facilitate electron transport through these molecular levels.

Chapter 6

Resistive Switching of Rose Bengal Devices - a Molecular Effect?

In previous chapters, studies concerning the conduction mechanism of BPn molecules have been of a more fundamental character. For later applications, e.g. for molecular electronics, a molecule which shows different conduction states is of much greater interest. As a candidate for such a switching molecule, Rose Bengal has been proposed in literature [218–222]. It was shown that thin layers of Rose Bengal, sandwiched between metallic electrodes in an MIM structure, possess two different conduction states that differ in their resistivity. The change between these two states is triggered by applying a positive or negative voltage above a certain threshold voltage.

All measurements reported in literature so far have focused on the switching effect of thin layers of Rose Bengal ($\sim 100nm$) and did not examine if this effect can be scaled down to the size of a single molecule. Furthermore, there is no actual proof that the switching is really a molecular effect or if the switching is probably triggered by an electrode effect. Therefore, in this chapter, it is examined whether resistive switching of thin layers of Rose Bengal is a molecular effect and, if so, whether this effect can be scaled down to single molecules.

6.1 Resistive Switching of Molecular Devices

Switching effects in organic molecules have already been known for more than thirty years [223, 224]. Since then a wide variety of molecules like tetracene [223], anthracene [224], MDCPAC [225], phenylene-ethylene oligomers (known as Tour Wires) [226–230], bipolar diarylethene [231], Cu-TBPP [232] and Rotaxane [233] have been proposed as basic materials for molecular memories. Recently, layers of Rose Bengal (see figure 6.1(a)) have been shown to switch resistively with high R_{OFF}/R_{ON} values [218–222], but the switching mechanism is still under discussion. Possible explanations are a change in

electrical conjugation of the Rose Bengal molecule by electrochemical reduction [220], a twist of the upper benzene ring [218], and the formation and breaking of metallic filaments. Similarly, some changes in the electrodes (e.g. by oxidation) or the interface between the electrode and the molecular film can cause the resistive switching.

To examine the switching behavior in more detail the elements of a Rose Bengal device are systematically replaced. In particular, current vs. voltage (IV) characteristics of devices with different bottom electrodes, with different molecular layers and finally without any molecular layer between the top and bottom electrode are shown.

6.2 Experimental Details

In contrast to the preceding chapters, an MIM type device structure is used; a thin layer of Rose Bengal is sandwiched between two metallic electrodes. To obtain layers of Rose Bengal and Xanthene (see figure 6.1), a solution of 100mg Rose Bengal or Xanthene in 50ml Ethanol is spun onto Zinc Oxide (doped with 1% Al, sheet resistance 3.3 $\Omega/\square$, roughness 3nm (rms)) or onto ITO bottom electrodes at different revolutions per minute (rpm) resulting in varying film thicknesses (56.5nm - 143nm for ZnO, 42nm - 160nm for ITO, measured by ellipsometry). For macroscopic measurements, circular aluminum pads (100nm thick) with contact areas ranging from 0.013mm^2 to 0.233mm^2 are evaporated in an e-gun vacuum chamber at a base pressure of 10^{-7} mbar at a deposition rate of 0.1nm/s.

For IV measurements, the voltage is applied with ZnO or ITO as the cathode and the metal top electrode as the anode by a voltage source (burster Digistant 4462) for two seconds prior to current measurements. The applied voltage is increased in 0.1V steps resulting in a frequency of a few mHz (maximum voltage $\pm$ 1.5V-2.5V). High frequency measurements are taken by an Aixacct TF analyzer 2000.

6.3 Results and Discussion

Figure 6.2 shows the IV characteristics of Rose Bengal layers. The device (ZnO bottom electrode, 143nm of Rose Bengal and aluminum top electrode, black line) shows resistive switching behavior with on switching (i.e. switching from the high resistive to the low resistive state) at positive and off switching (i.e. from the low resistive to the high resistive state) at negative voltages. On switching occurs between 0.5V and 1V and off switching at -1V.

The on state shows a linear IV characteristic, whereas the off state deviates from linearity at high voltages. The impedance of the off state is 20kΩ and of the on state 400Ω, resulting in a R_{OFF}/R_{ON} ratio of 50. Typical R_{OFF}/R_{ON} ratios are obtained in the range of 2-50.

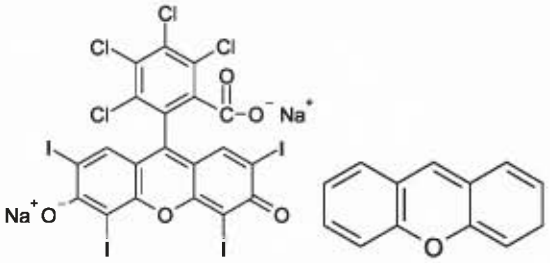

Figure 6.1: Molecular structure of Rose Bengal (a) and Xanthene (b).

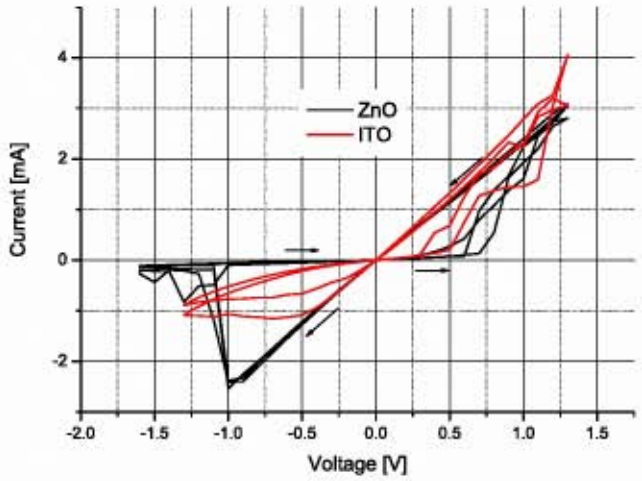

Figure 6.2: IV characteristic of a layer of Rose Bengal (143nm) on ZnO and on ITO (55nm). Both samples are contacted by an aluminum pad (contact area 0.0288mm^2). On-switching occurs at positive voltages and off-switching at negative values.

Frequency (Hz)	V_{ON}	V_{OFF}
100	0.64	-0,85
1K	0.76	-0,8
10K	0.65	-1
100K	–	–

Table 6.1: Frequency dependence of the switching voltages. Above 10kHz switching vanished. The device consists of an ITO bottom electrode, 85nm Rose Bengal and an aluminum top electrode (contact area 0.066mm^2).

Replacing the ZnO bottom electrode by ITO, the switching can be observed as well (shown in red in figure 6.2). The IV characteristics are basically the same, except that off switching is not as abrupt and the off state is not as highly insulating as in the case of ZnO, resulting in a lower R_{OFF}/R_{ON} ratio of about 6. This effect is most probably due to the thinner Rose Bengal film on ITO compared to the film on ZnO (55nm compared to 143nm)[1]. Generally, the switching of all devices shows the same distinct features: the on state is linear, whereas the off state deviates from linearity at higher voltages. Furthermore, on switching occurs at lower voltages than off switching. This switching behavior is almost identical to the switching behavior of Rose Bengal devices described by Jakobsson at al. [234] but shows significantly larger currents than the switching shown by Bandyopadhyay et al. [219].

For later applications, the switching speed of the devices is of fundamental interest. The frequency dependence of the switching voltages is shown in table 6.1. Up to 10kHz, there is no significant change in the switching properties. Above 10kHz the switching vanishes, giving a time constant of approximately 0.1ms for the switching mechanism. This time constant is surprisingly large pointing to a switching mechanism that is not purely electronic.

In literature, the resistive switching behavior of devices of Rose Bengal is explained by two different conduction states of the Rose Bengal molecule. Therefore, an attempt is made to study how the switching is influenced by the molecule, or if there is any influence at all, by replacing the layer of Rose Bengal by a layer of a much simpler molecule, Xanthene. The result is shown in figure 6.3.

The IV characteristic of the Xanthene film shows resistive switching with off switching at -1.1V and on switching at 0.7V and in this respect it is very similar to the layers of Rose Bengal. However, the R_{OFF}/R_{ON} ratio is much lower than for the Rose Bengal devices. Especially the off state has a much lower resistance ($\sim 230\Omega$), whereas the on state resistance (200Ω) is similar to the Rose Bengal devices.

Despite the much lower R_{OFF}/R_{ON} ratio of devices based on Xanthene, the switching

[1]The dependence of the R_{OFF}/R_{ON} ratio on the thickness of the Rose Bengal layer is studied in detail in section 6.3.1.

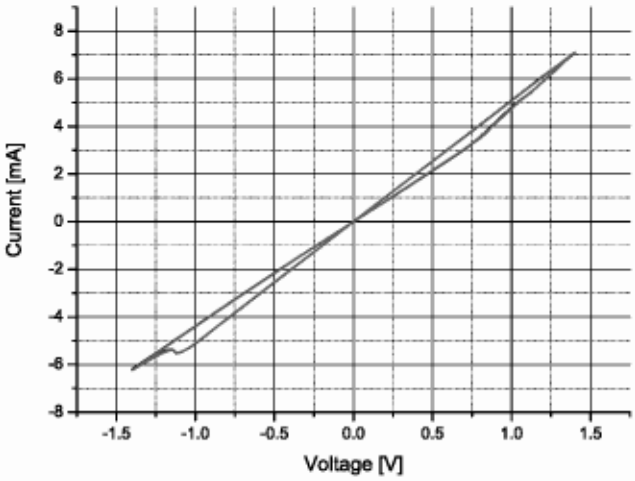

Figure 6.3: I/V characteristic of a device consisting of ZnO bottom electrode, Xanthene layer (135nm), and aluminum top electrode. Three subsequent loops are shown. The contact area is $0.0288mm^2$.

is reproducible and the switching voltages are identical for Rose Bengal and Xanthene devices. Therefore, some theories concerning the nature of the switching given elsewhere can be excluded. The Xanthene molecule does not possess the upper benzene ring, which has occasionally been suggested to cause the switching by a rotation and a subsequent change in conjugation [218]. However, it can be concluded that the molecule has an influence on the switching and that Rose Bengal amplifies the resistive switching compared to Xanthene.

Since the devices with a Xanthene layer show switching, some theories about switching in Rose Bengal devices can be excluded, but still no switching mechanism can be positively suggested. In this respect an experiment ist more helpful which has actually only been thought of as simple control experiment. In figure 6.4, the IV characteristic of devices where the molecular layer is completely omitted and aluminum was deposited directly onto ZnO and ITO is shown. Even in these devices, the switching persists in a very similar fashion to the switching of the Xanthene devices. For ZnO bottom electrodes, on switching occurs at ~1.2V and off switching at -1.5V. For ITO, the switching voltages are slightly reduced to 0.8V and -1V. Interestingly, when measured immediately after deposition of the top electrode, the IV measurement of the ITO devices displays a short circuit and only three days later was the stable hysteresis shown in figure 6.4(b)

obtained.

This result can be explained by considering the fact that a metal, which can be easily oxidized to Al_2O_3, and which has a more negative redox potential than zinc, indium and tin (the different bottom electrode components), is deposited onto an oxidic bottom electrode. Therefore, an insulating layer of aluminum oxide is formed at the interface between bottom and top electrode. Layers of aluminum oxide and of other metal oxides like TiO, NiO, HfO_2, ZrO_2 and V_2O_5 have already been shown to exhibit bistable switching [235–242]. Even in ultrathin layers of aluminum oxide (thickness below 1nm), two conduction states were found [239], one ohmic and one tunneling state. However, the transition between these two states in the ultrathin layers was not continuous and was probably triggered by external noise.

In literature, the switching is often related to a dielectric breakdown and forming process in the oxide, which changes the phase or composition of the material between the electrodes. For example, Ansari et al. [242] argued that TiO_x possesses different phases between TiO_2 and $TiO_{1.75}$. A change between these phases was suggested to be triggered by energy dissipation. Very often it was assumed that the switching effect is localized in small spots (filaments) [235, 237, 243]. Besides this filament approach to explain switching in simple oxides, there are different theories like current transport through two different defect states for the on and off state [236, 241] or the suppression of a tunneling barrier due to high currents [239].

To verify that an oxidic layer is responsible for switching in the aluminum/bottom electrode device, two experiments are conducted. Firstly, by replacing the aluminum top electrode by gold, which is a noble metal and cannot be oxidized, switching can successfully be suppressed pointing to an essential role of the oxide. Secondly, 2nm of aluminum are sputtered onto ZnO and oxidized at a pressure of 200mbar O_2 for 30min. By repeating this step, a ~5nm thick Al_2O_3 layer is grown. On top of the oxide, 80nm of aluminum is sputtered. By this procedure, a thin oxide layer between the top and bottom electrode is intentionally grown, which is argued to be responsible for switching. The result is shown in figure 6.5. Switching occurs in a very similar fashion to the Rose Bengal devices: on switching occurs at positive and off switching at negative voltages. The on state is linear, whereas the off state deviates from linearity and on switching occurs at lower voltages than off switching.

The similarity of the switching of aluminum oxide and Rose Bengal leads to the conclusion that the switching in Rose Bengal devices is closely related to the switching of Al_2O_3. From degradation studies of organic light emitting diodes (OLEDs) it is known that a thin Al_2O_3 layer is formed underneath the top electrode [244]. However, the low resistance and the linearity of the on state strongly suggest that the molecular layer does not take part in the conduction at all. Conduction in an organic layer would

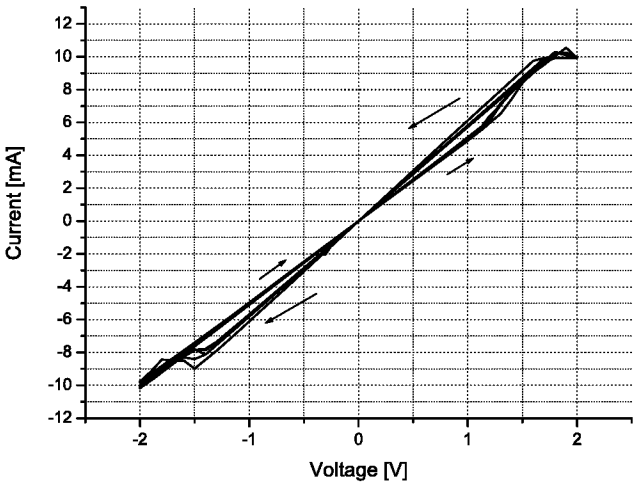

(a)

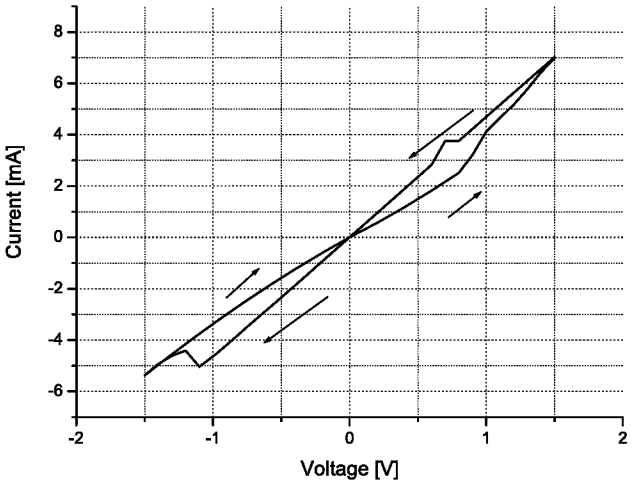

(b)

Figure 6.4: IV characteristic of a ZnO/aluminum (a) and ITO/aluminum (b) stack. Both show resistive switching. The contact area is 0.0288mm^2.

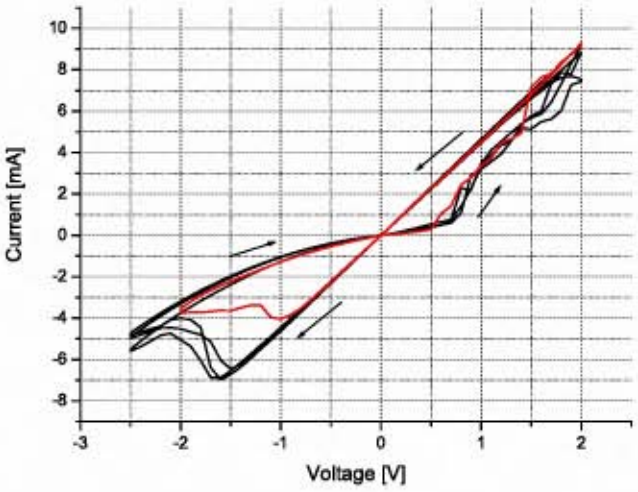

Figure 6.5: Switching of a device consisting of ZnO, 5nm Al_2O_3 and 80nm Al (black). For comparison, a IV characteristic of a ZnO/70nm Rose Bengal/aluminum is shown in red. The characteristic of the switching is almost identical. For both devices, the contact area is $0.0288mm^2$.

show a characteristic diode behavior that is governed by both, charge injection at the electrodes and charge carrier mobilities. Especially the large currents seen in figure 6.2 are not compatible with the charge carrier mobilities found in organic materials.

There are two ways in which the organic layer can be short circuited so that it does not take part in the conduction process. First of all, analogous to a breakdown mechanism of Al_2O_3 at high electric fields, aluminum ions can migrate through the sample and short circuit the organic layer [245]. Similarly, during deposition of the top electrode, aluminum ions can already punch through the molecular layer.

Either of these explanations results in paths of aluminum that bypass the organic layer. However, a complete short circuit is avoided since at the contact of these aluminum paths with the ZnO or ITO bottom electrode, the aluminum is oxidized similarly to the oxidation of an aluminum electrode which is directly deposited onto ZnO or ITO as seen in figure 6.4. Thereby, the whole switching as observed in figure 6.2 is explained by the switching of a thin layer of Al_2O_3 as seen in figure 6.5 and is thus not a molecular effect.

However, it has to be noted that the results presented here do not exclude the possibility that Rose Bengal can show a molecular switching effect in other experimental

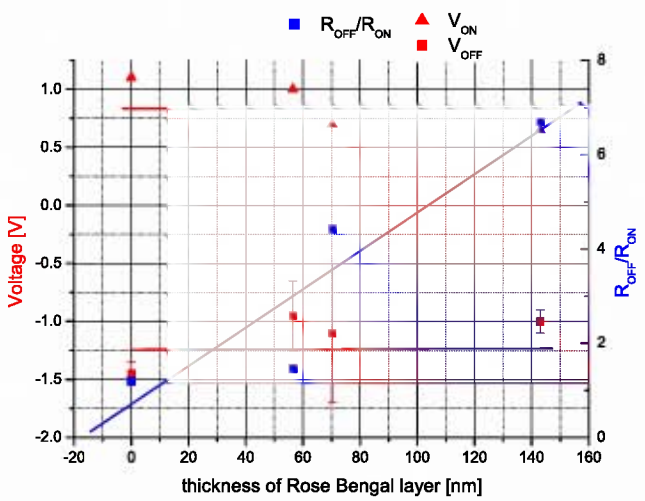

Figure 6.6: Thickness dependence of the on and off switching voltages of Rose Bengal devices contacted by a ZnO bottom and aluminum top electrode.

setups. In fact, in the on state the molecular layer is short circuited so that no conclusion about the molecule can be drawn. Furthermore, the magnitude of the currents shown in figure 6.2 is higher than that observed by Bandyopadhyay et al. [219], who also observed switching with mercury top electrodes [222]. But the findings of this chapter show that one has to be very careful in automatically assigning a bistable switching effect of a molecular layer contacted by metal electrodes to the molecule. Most importantly, a linear on state with a low resistivity, as occasionally reported for Rose Bengal and other molecular layers [234], is always a strong indication of an extrinsic electrode effect instead of molecular switching.

6.3.1 Thickness Dependence of the Switching Effect

Although the switching effect observed in these studies has turned out not to be a molecular effect, it is an interesting phenomenon which deserves to be looked at further. As an additional characterization, the switching voltages and the R_{OFF}/R_{ON} ratio was measured for films with varying thickness (see figure 6.6).

In figure 6.6 the switching voltages and the R_{OFF}/R_{ON} ratio is shown for different thicknesses (0nm-140nm, 0nm corresponds to the aluminum electrode directly deposited onto the ZnO electrode). The on switching voltage varies slightly between 1.1V and

0.7V and the off switching voltage between -1.4V and -1.0V. These switching voltages are another indication that the Rose Bengal layer does not take part in the switching process. If the thickness of the Rose Bengal layer is increased from $\sim$ 55nm to 140nm, the switching voltages have to increase by a factor of $\sim$ 3 to provide the same electric field in the sample. Instead, the magnitude of the switching voltages decreases slightly.

The R_{OFF}/R_{ON} ratio increases with increasing thickness. Again, this can be explained by the extrinsic switching mechanism proposed in the preceding section. If the thickness is increased, fewer aluminum ions can penetrate the Rose Bengal layer so that there are fewer filaments or conducting aluminum paths that short circuit the Rose Bengal layer. Consequently, at least the off resistance increases. The on resistance, on the other hand, is very low and is mainly determined by the series resistance of the measurement setup[2]. Therefore, the on resistance is not influenced by the thickness of the Rose Bengal layer so that the R_{OFF}/R_{ON} rises.

6.4 Conclusion

A Rose Bengal thin film sandwiched between a ZnO or ITO bottom electrode and aluminum top electrode is shown to exhibit resistive switching. By replacing Rose Bengal by Xanthene and finally omitting the molecular layer, it is shown that the switching observed in this thesis is not a molecular effect. Furthermore, due to the strong similarity of the switching of the Rose Bengal devices to the switching of a 5nm Al_2O_3 layer, it is suggested that the switching is completely extrinsic, i.e. an effect of the electrodes which is not due to the material of the layer between the electrodes.

Although the switching effect is not caused by Rose Bengal, Rose Bengal amplifies the switching, visible in the comparison of figure 6.2 and 6.3. This amplification can be explained by the oxidizing property of Rose Bengal. Rose Bengal is widely used as a photosensitizer and produces singlet oxygen [246, 247]. The sequence of events of photosensitized oxidation involves excitation of the sensitizer, intersystem crossing, energy transfer from the triplet of the sensitizer to molecular oxygen, and reaction of the formed singlet oxygen with the substrate. Especially if a reactive singlet oxygen acceptor (like aluminum) is used as the top electrode, this photoreaction can be very effective and will enhance the oxidation of the top electrode.

[2]The series resistance mainly consists of the resistance of the 1×1 inch ZnO bottom electrode

Chapter 7

Conclusion

The aim of this thesis is the development of a method for the characterization of the electrical transport across functional organic molecules. In particular, the electrical transport of a special class of molecules, biphenylthiols (BPn), is measured. A self organized device setup as shown in the introduction (see figure 1.9) is developed, which can be used for a wide variety of molecules. As a consequence of this device setup, the thesis is divided into five experimental parts: the optimization of the gold bottom electrode, the deposition of the SAM of dodecanethiol, the characterization of full coverage layers of BPn and the embedding of BPn molecules into a dodecanethiol monolayer. Finally, the switching effect of thin layers ($\sim 100nm$) of a more complex molecule, Rose Bengal is studied in a MIM-type setup.

Gold Bottom Electrode

In the first experiments, gold films are deposited onto mica at low deposition rates (1Å/s) and high temperatures (464°C-610°C). These films show pure three dimensional growth and only a very poor conductivity. By increasing the deposition rate to 50Å/s, the growth mode changes to layer by layer growth and a continuous layer of gold is produced. However, the high deposition rate leads to holes in the films, so that in order to fill these holes a second step of slow deposition is introduced (0.5Å/s).

This two step deposition process results in very smooth gold films (roughness of only 2-3Å) with large terraces. Two structures of the terrace edges can be seen: rounded step edges and linear step edges along the $\langle 01\bar{1} \rangle$ directions (faceting). The linear step edges are generated by a stress relaxation mechanism. At low temperatures, the stress is mainly due to the differences in the coefficients of thermal expansion of mica and gold, whereas at higher temperatures additional stress is introduced due to the decomposition of mica.

To summarize, a stable, fast and efficient process for the deposition of very smooth

gold films is developed. Due to the large, (111)-oriented terraces, the gold films are perfectly suited for the deposition of SAMs and characterization of these films by STM. Although Höpfner et al. [82] already proposed a similar two-step process as developed in this thesis, they did not optimize the films in terms of a low roughness. Therefore, the use of this two-step deposition method for obtaining smooth gold films is a valuable addition to the already existing literature in this field. Furthermore, the clarification of the origin of faceting of these gold films supplements the knowledge in this area [88].

Alkanethiol SAM

Two deposition methods are used to grow self-assembled monolayers of dodecanethiol: deposition from solution and from the gas phase.

SAMs grown from solution consist of many small molecular domains (diameter 5-15nm) and a high density of vacancy islands. By annealing the films at 78°C in a 1mM solution of dodecanethiol for one hour, the size of the domains is increased (diameter 15-25nm) and the density of vacancy islands is decreased. For longer annealing times (6.5h), molecules are desorbed from the surface and, besides the high coverage, standing up phase, lower coverage phases (lying-down phases) appear. The high coverage phase shows slight deviations in the molecular arrangement compared to the normal c(4x2) phase.

SAMs grown from the gas phase are superior to samples grown from solution in terms of domain size and cleanliness of the substrate. The molecular domain size is only limited by the size of the underlying gold terrace. It is shown that the samples display different phases of the c(4x2) structure, the well-known δ-phase and a new ζ-phase.

SAMs of alkanethiol are probably one of the best characterized classes of SAMs. Nonetheless, two details discovered in this thesis are new: the evidence that the structure of SAMs of C12 close to desorption deviates from the normal c(4x2) structure, described in the publication of Müller-Meskamp et al [170], and the discovery of a new phase of the c(4x2) structure [172].

Characterization of Full Coverage SAMs of BPn

SAMs of biphenylthiols display a distinct odd-even effect. Whereas BPn with n=3 shows a very well-defined $\left(2\sqrt{3} \times \sqrt{3}\right)$ structure, the structure of BPn with n=even is much less defined.

This behavior is explained by the structural misfit of BPn with n=even with the gold lattice. Whereas for BPn, n= odd, a low energy structure in terms of molecular conformation, Au-S-C binding angle and adsorption sites on the gold lattice can be obtained, for BPn, n=even, this configuration is not possible. Due to the even number

of CH_2 units the biphenyl unit is forced into a considerably more tilted conformation. The resulting structure is determined by a compromise between the forces acting on the molecule, such as the molecule-substrate interaction, the intermolecular interactions and the forces due to conformational energies. This renders the structure of BPn, n−even, much less defined and consequently different molecular structures are found: a $(4\times6\sqrt{3})$ structure for BP2 and BP4 and a $(4\times\sqrt{3})$ structure for BP4.

Besides the structural characterization, films of BPn are also characterized electrically. It is shown that the current vs. voltage characteristic can be explained by a simple tunneling model. No sharp features are observed in the IV characteristics nor in the plot of the differential conductance that would suggest a resonant transport across a molecular level.

By IS spectroscopy, the decay constant of the molecule is measured vertically resolved. The SAM is shown to be composed of two parts, each part with a different decay constant β. These parts are interpreted as the biphenyl unit and the alkane chain of BPn. By these measurements, the decay length β of the biphenyl unit is determined to be $4.7 \pm 0.8nm^{-1}$.

This chapter complements the existing literature in various ways. First of all, the $(4\times6\sqrt{3})$ structure for BP2 and BP4 has not been reported elsewhere. Furthermore, this chapter represents the first studies of the gas phase growth of SAMs of BPn and the first studies of the electronic transport properties by IV and IS spectroscopy.

Characterization of Embedded BPn in Alkanethiol SAMs

In the first experiments, alkanedithiols are embedded into a dodecanethiol SAM by immersing a preassembled C12 film into a 1mM solution of alkanedithiols for 10min. This process results in embedded single molecules or at least embedded bundles with a low number of molecules (<30 molecules). The upper -SH group of the dithiols can be contacted by a gold cluster. The current vs. voltage characteristic of embedded alkanedithiols contacted by a gold cluster shows a suppression of the current for voltages below 0.2V, which can be explained by the Coulomb blockade effect.

Following these experiments, biphenylthiols (BP4) are embedded into a dodecanethiol SAM. By immersion of a dodecanethiol SAM into a $100\mu M$ solution of BP4 for 10min at room temperature, single BP4 or small bundles of BP4 are embedded into the dodecanethiol layer (<30 molecules).

Increasing the deposition time to 20min and the temperature to 70°C, SAMs consisting of phase segregated BP4 and dodecanethiol domains are produced. It is shown that domain boundaries and pits in the gold surface act as nucleation points for BP4 domains. Annealing the film at 64°C results in a higher order of the BP4 domains and a slight decrease of the height of BP4 domains above C12.

For the presented experimental conditions, some BP4 molecules are found to be inserted into the middle of a C12 domain. Their size and position can be determined by using the underlying c(4x2) structure of the alkanethiols as a coordinate system. Thereby, it is shown that the protrusions in the C12 domains contain less than four molecules and are most probably due to single embedded BP4 molecules. Furthermore, these molecules are fixed in the C12 structure and do not migrate at room temperature.

The height difference of the domains of BP4 compared to the C12 SAM is explained in terms of a higher tunneling conductance of BP4. A simple two-layer model is proposed by means of which the current transport through the BP4 group is discussed and the decay constant β_{Ph} of $\sim 5nm^{-1}$ is deduced.

This chapter is the first study of embedded BP4 in C12 [248]. The interpretation of the height of the different molecular species follows the method first proposed by Bumm et al. [52]. However, for the first time, it is shown in this thesis that the tunneling conductance of BPn can be obtained by splitting the molecule up into the alkane and the biphenyl part and by combining the conductances of these two parts.

A Candidate for a Switching Molecule: Rose Bengal

A thin film consisting of Rose Bengal sandwiched between a ZnO or ITO bottom electrode and Al top electrode is shown to exhibit resistive switching with on- and off-switching voltages of $\sim 0.5 - 1V$ and $\sim -1V$, respectively. The R_{OFF}/R_{ON} ratio is dependent on the thickness of the Rose Bengal layer. Typical R_{OFF}/R_{ON} ratios are in the range of 2-50. By replacing Rose Bengal by Xanthene and finally leaving out the molecular layer, it is shown that the switching observed in this thesis is not a molecular effect. Furthermore, due to the strong similarity of the switching of the Rose Bengal devices to the switching of a 5nm Al_2O_3 layer, it is suggested that the switching is completely extrinsic, i.e. an effect of the electrodes which is not primarily dependent on the material of the layer between the electrodes.

The importance of this chapter for research in this area lies in the proposition of a molecularly independent switching effect, which may be in operation in other devices. Evidences for this switching effect are a very low on resistance and a linear IV dependence [249].

Outlook and Suggestions for Further Work

The device setup developed in this thesis can be used for the characterization of a wide variety of molecules. There are only a few demands that these molecules have to meet. First of all, to facilitate chemical binding to the substrate, the molecules have to possess a bottom group that binds to gold. Furthermore, at least for the deposition of phase segregated mixed SAMs, the molecules have to be able to form well ordered, single

component SAMs. For a quantitative interpretation of the height differences in STM images between the embedded molecules and the surrounding insulating SAM, e.g. for the deduction of the decay length β, the structure of the SAM and the conformation of the molecules has to be known. The interpretation is further simplified if both molecular species possess the same top and bottom groups.

Very interesting questions can be answered for these molecules. For example, how do side groups influence the electric transport? Is it possible to "tune" the molecules to possess a low HOMO-LUMO gap, e.g. by increasing the length of the phenylene part of the molecule? Does the decay length β depend on the voltage? How can the contact between the molecule and the gold substrate be optimized, e.g. through different bonding groups?

These measurements would lead to a more detailed understanding of the current transport mechanism of single molecules. These insights could be applied to optimize the molecules used, for example, for organic field effect transistors or organic light emitting diodes. Furthermore, molecules could be identified that possess two different conduction states and that could be used for molecular memories. Candidates for such molecules are redox-active substances such as ferrocene [42].

The device setup presented here is useful for fundamental research, but does not include a method for integrating molecules and contacting a large number of single molecular devices. Therefore, a necessary way to proceed from these basic studies towards real (single) molecular electronics would be to test and evaluate methods of integrating such molecular devices. In literature, some device setups are proposed that can be integrated, e.g. the nanopore [250], the nanowell [49] or the mushroom concept [251]. Probably the most promising setup for integration is a simple crossbar structure. For example, by the superlattice nanowire pattern transfer technique [252] or by nanoimprint techniques [253], it is possible to prepare nanowires with a diameter of below 10nm. Therefore, crossbar structures with device sizes of below $10 \times 10nm^2$ are possible, which would consist of only a few hundred molecules. This would be the first step towards the integration of a large number of molecular devices, but for real "single" molecular devices these techniques have to be improved and the device area has to be further decreased.

Bibliography

[1] J. Bardeen, W.H. Brattain, The Transistor, A Semi-Conductor Triode. *Physical Review* **74**, 230–231 (1948).

[2] J. S. Kilby, Turning Potential into Realities: The Invention of the Integrated Circuit. Nobel Lecture , December 2000. http://nobelprize.org/physics/laureates/2000/kilby-lecture.pdf.

[3] G.E. Moore, Cramming more components onto integrated circuits. *Electronics* **38** (1965).

[4] R. Doering, Societal Implications of Scaling to Nanoelectronics. In *Societal Implications of Nanoscience and Nanotechnology – NSET Workshop Report*, 2001.

[5] E.W.A. Young, S.Mantl, P.B. Griffin, *Nanoelectronics and Information Technology – Advanced Electronic Materials and Novel Devices*, Chapter Silicon MOSFETs-Novel Materials and Alternative Concepts, S. 361–385, Wiley-VCH, Weinheim (2003).

[6] R. Waser, *Nanoelectronics and Information Technology – Advanced Electronic Materials and Novel Devices*, Chapter Logic Devices, S. 323–358, Wiley-VCH, Weinheim (2003).

[7] J.D. Meindl, Low Power Microelectronics: Retrospect and Prospect. *Proceedings of the IEEE* **83**, 619–635 (1995).

[8] J.D. Meindl, Q. Chen, J.A. Davis, Limits on Silicon Nanoelectronics for Terascale Integration. *Science* **293**, 2044–2049 (2001).

[9] V.V. Zhirnov, R.K. Cavin, J.A. Hutchby, G.I. Bourianoff, Limits to Binary Logic Switch Scaling - A Gedanken Model. *Proceedings of the IEEE* **91**, 1934–1939 (2003).

[10] T. Schulz, *Konzepte zur lithographieunabhängigen Skalierung von vertikalen Kurzkanal-MOS-Feldeffekt-Transistoren und deren Bewertung.* Ruhr-Universität Bochum, 2001.

[11] International Technology Roadmap for Semiconductors, 2004 Update. http://public.itrs.net , 2004.

[12] National Nanotechnology Initiative: The Initiative and Its Implementation Plan. http://www.nano.gov/html/res/nni2.pdf , July 2000.

[13] C. Delerue, M. Lannoo, *Nanostructures – Theory and Modelling.* Springer-Verlag Berlin Heidelberg New York, 2004.

[14] R. A.L. Jones, *Soft Machines – Nanotechnology and Life.* Oxford University Press, 2004.

[15] G. Binning, H. Rohrer, Scanning Tunneling Microscopy. *Surface Science* **126**, 236–244 (1983).

[16] G. Binning, H. Rohrer, Scanning Tunneling Microscopy. *Helvetica Physica Acta* **55**, 726 735 (1982).

[17] G. Binning, H. Rohrer, E. Weibel, 7x7 Reconstruction on Si(111) Resolved in Real Space. *Physical Review Letters* **50**, 120–123 (1983).

[18] Gerd Binning, Heinrich Rohrer, Scanning tunneling microscopy - from birth to adolescence. *Reviews of modern physics* **59**, 615–625 July 1987. Lecture from Dec 1986 on the occasion of the presentation of the Nobel Prize in Physics.

[19] J. Tersoff, D.R. Hamann, Theory of the Scanning Tunneling Microscope. *Physical Review B* **31**, 805 813 (1985).

[20] R. Waser, *Nanoelectronics and Information Technology – Advanced Electronic Materials and Novel Devices.* Wiley-VCH Verlag GmbH, Weinheim, 2003.

[21] D.M. Eigler, E.K. Schweizer, Positioning Single Atoms with a Scanning Tunneling Microscope. *Nature* **344**, 524–526 (1990).

[22] S.-W. Hla, L. Bartels, G. Meyer, K.-H. Rieder, Inducing All Steps of a Chemical Reaction with the Scanning Tunneling Microscope Tip: Towards Single Molecule Engineering. *Physical Review Letters* **85**, 2777 2780 (2000).

[23] L.A. Bumm, J.J. Arnold, M.T. Cygan, T.D. Dunbar, T.P. Burgin, L. Jones II, D.L. Allara, J.M. Tour, P.S. Weiss, Are Single Molecular Wires Conducting? *Science* **271**, 1705–1707 (1996).

[24] W. Wang, T. Lee, M.A. Reed, Mechanism of Electron Conduction in Self-Assembled Alkanethiol Monolayer Devices. *Physical Review B* **68**, 035416 (2003).

[25] R. E. Holmlin, R. Haag, M. L. Chabinyc, R. F. Ismagilov, A. E. Cohen, A. Terfort, M. A. Rampi, G. M. Whitesides, Electron Transport Through Thin Organic Films in Metal-Insulator-Metal Junctions Based on Self-Assembled Monolayers. *Journal of the American Chemical Society* **124**, 8762–8762 (2002).

[26] J. Chen, M. A. Reed, A. M. Rawlett, J. M. Tour, Large On-Off Ratios and Negative Differential Resistance in a Molecular Electronic Device. *Science* **286**, 1550–1552 (1999).

[27] J. Chen, J. Su, W. Wang, M. A. Reed, Electronic Memory Effects in Self-Assembled Monolayer Systems. *Pysica E-Low Dimensional Systems & Nanostructures* **16**, 17–23 (2003).

[28] D. K. James, J. M. Tour, Electrical Measurements in Molecular Electronics. *Chemistry of Materials* **16**, 4423–4435 (2004).

[29] R. Martel, T. Schmidt, H. R. Shea, T. Hertel, Ph. Avourisa, Single- and Multi-Wall Carbon Nanotube Field-Effect Transistors. *Applied Physics Letters* **73**, 2447–2449 (1998).

[30] V. Sazonova, Y. Yaish, H. Üstünel, D. Roundy, T. A. Arias, P. L. McEuen, A Tunable Carbon Nanotube Electromechanical Oscillator. *Nature* **431**, 284–287 (2004).

[31] T. Rueckes, K. Kim, E. Joselevich, G. Y. Tseng, C. L. Cheung, C. M. Lieber, Carbon Nanotube-Based Nonvolatile Random Access Memory for Molecular Computing. *Science* **289**, 94–97 (2000).

[32] B. Q. Q. Xu, X. L. L. Li, X. Y. Y. Xiao, H. Sakaguchi, N. J. J. Tao, Electromechanical and Conductance Switching Properties of Single Oligothiophene Molecules. *Nano Letters* **5**, 1491–1495 (2005).

[33] C. P. Collier, G. Mattersteig, E. W. Wong, Y. Luo, K. Beverly, J. Sampaio, F. M. Raymo, J. F. Stoddart, J. R. Heath, A [2]catenane-Based Solid State Electronically Reconfigurable Switch. *Science* **289**, 1172–1175 (2000).

[34] H. Park, J. Park, A. K. L. Lim, E. H. Anderson, A. P. Alivisatos, P. L. McEuen, Nanomechanical Oscillations in a Single-C-60 Transistor. *Nature* **407**, 57 60 (2000).

[35] A. N. Pasupathy, J. Park, C. Chang, A. V. Soldatov, S. Lebedkin, R. C. Bialczak, J. E. Grose, L. A. K. Donev, J. P. Sethna, D. C. Ralph, P. L. McEuen, Vibration-Assisted Electron Tunneling in C-140 Transistors. *Nano Letters* **5**, 203–207 (2005).

[36] K. M. Roth, N. Dontha, R. B. Dabke, D. T. Gryko, C. Clausen, J. S. Lindsey, D. F. Bocian, W. G. Kuhr, Molecular Approach Toward Information Storage Based on the Redox Properties of Porphyrins in Self-Assembled Monolayers. *Journal of Vacuum Science & Technology B* **18**, 2359–2364 (2000).

[37] T. Xu, I. R. Peterson, M. V. Lakshmikantham, R. M. Metzger, Rectification by a Monolayer of Hexadecylquinolinium Tricyanoquino-Dimethanide Between Gold Electrodes. *Angewandte Chemie International Edition* **40**, 1749–1752 (2001).

[38] A. S. Martin, J. R. Sambles, G. J. Ashwell, Molecular Rectifier. *Physical Review Letters* **70**, 218–221 (1993).

[39] J. Park, A. N. Pasupathy, J. I. Goldsmith, C. Chang, Y. Yaish, J. R. Petta, M. Rinkoski, J. P. Sethna, H. D. Abruna, P. L. McEuen, D. C. Ralph, Coulomb Blockade and the Kondo Effect in Single-Atom Transistors. *Nature* **417**, 722–725 (2002).

[40] A. A. Dameron, J. W. Ciszek, J. M. Tour, P. S. Weiss, Effects of Hindered Internal Rotation on Packing and Conductance of Self-Assembled Monolayers. *Journal of Physical Chemistry B* **108**, 16761–16767 (2004).

[41] C.B. Gorman, R.L. Carroll, R.R. Fuierer, Negative Differential Resistance in Patterned Electroactive Self-Assembled Monolayers. *Langmuir* **17**, 6923–6930 (2001).

[42] L. Müller-Meskamp, B. Lüssem, S. Karthäuser, S. Prikhodovski, M. Homberger, U. Simon, R. Waser, Molecular Structure of Ferrocenethiol Islands Embedded Into Alkanethiol Self-Assembled Monolayers Studied by UHV-STM. *Physical status solidi (c)* submitted (2005).

[43] D. R. Stewart, D. A. A. Ohlberg, P. A. Beck, Y. Chen, R. S. Williams, J. O. Jeppesen, K. A. Nielsen, J. F. Stoddart, Molecule-Independent Electrical Switching in Pt/Organic Monolayer/Ti Devices. *Nano Letters* **4**, 133–136 (2004).

[44] C. Joachim, J. K. Gimzewski, A. Aviram, Electronics Using Hybrid-Molecular and Mono-Molecular Devices. *Nature* **408**, 541–548 (2000).

[45] M. Mayor, H.B. Weber, R. Waser, *Nanoelectronics and Information Technology – Advanced Electronic Materials and Novel Devices*, Chapter Molecular Electronics, S. 503–525, Wiley-VCH, Weinheim (2003).

[46] S. Datta, *Electronic Transport in Mesoscopic Systems.* Cambridge University Press, 1995.

[47] J. K. Tomfohr, *Electron Tunneling Transport Theory for Molecules.* Arizona State University, 2002.

[48] J. G. Simmons, Generalized Formula for the Electric Tunnel Effect between Similar Electrodes Separated by a Thin Insulating Film. *Journal of Applied Physics* **34**, 1793–1803 (1963).

[49] N. Majumdar, N. Gergel, D. Routenberg, J.C. Bean, L.R. Harriott, B. Li, L. Pu, Y. Yao, J.M. Tour, Nanowell Device for the Electrical Characterization of Metal-Molecule-Metal Junctions. *Journal of Vacuum Science Technology B* **23**, 1417 1421 (2005).

[50] V.L. Mironov, *Fundamentals of Scanning Probe Microscopy.* The Russian Academy of Science, 2004.

[51] J.G. Simmons, Low-Voltage Current-Voltage Relationship of Tunnel Junctions. *Journal of Applied Physics* **34**, 238–239 (1963).

[52] L.A. Bumm, J.J. Arnold, T.D. Dunbar, D.L. Allara, P.S. Weiss, Electron Transfer through Organic Molecules. *Journal of Physical Chemistry B* **103**, 8122–8127 (1999).

[53] K. Slowinski, H. K.Y. Fong, M. Majda, Mercury-Mercury Tunneling Junctions. 1. Electron Tunneling Across Symmetric and Asymmetric Alkanethiolate Bilayers. *Journal of the American Chemical Society* **121**, 7257–7261 (1999).

[54] Y. Yasutake, Z. Shi, T. Okazaki, H. Shinohara, Y. Majama, Single Molecular Orientation Switching of an Endohedral Metallofullerene. *Nano Letters* **5**, 1057 (2005).

[55] D. J. Wold, C.D. Frisbie, Formation of Metal-Molecule-Metal Tunnel Junctions: Microcontacts to Alkanethiol Monolayers with a Conducting AFM Tip. *Journal of the American Chemical Society* **122**, 2970–2971 (2000).

[56] Y. Selzer, A. Salomon, D. Cahen, The Importance of Chemical Bonding to the Contact for Tunneling through Alkyl Chains. *Journal of Physical Chemistry B* **106**, 10432 10439 (2002).

[57] C.-C. Kaun, H. Guo, Resistance of Alkanethiol Molecular Wires. *Nano Letters* **3**, 1521 1525 (2003).

[58] S. Wakamatsu, U. Akiba, M. Fujikira, Electronic Tunneling through Self-Assembled Monolayers of Phenylene Oligomers on Au(111). *Japanese Journal of Applied Physics* **41**, 4998–5002 (2002).

[59] S. Wakamatsu, S. Fujii, U. Akiba, M. Fujikira, Dependence of Tunneling Current Through a Single Molecule of Phenylene Oligomers on the Molecular Length. *Ultramicroscopy* **97**, 19–26 (2003).

[60] D.J. Wold, R. Haag, M.A. Rampi, C.D. Frisbie, Distance Dependence of Electron Tunneling through Self-Assembled Monolayers Measured by Conducting Probe Atomic Force Microscopy: Unsaturated versus Saturated Molecular Junctions. *Journal of Physical Chemistry B* **106**, 2813–2816 (2002).

[61] E.E. Polymeropoulos, J. Sagiv, Electrical Conduction through Adsorbed Monolayers. *Journal of Chemical Physics* **69**, 1836–1847 (1978).

[62] R.G. Nuzzo, D.L. Allara, Adsorption of Bifunctional Organic Disulfides on Gold Surfaces. *Journal of the American Chemical Society* **105**, 4481 4483 (1983).

[63] F. Schreiber, Structure and Growth of Self-Assembling Monolayers. *Progress in Surface Science* **65**, 151–256 (2000).

[64] A. Demoz, D.J. Harrison, Characterization of Extremely Low Defect Density Hexadecanethiol Monolayers on Hg Surfaces. *Langmuir* **9**, 1046–1050 (1993).

[65] M. Stratmann, Chemically Modified Metal Surfaces A New Class of Composite Materials. *Advanced Materials* **2**, 191–195 (1990).

[66] P.E. Laibinis, G.M. Whitesides, Self-Assembled Monolayers of n-Alkanethiolates on Copper are Barrier Films that Protect the Metal against Oxidation by Air. *Journal of the American Chemical Society* **114**, 9022–9028 (1992).

[67] C. Wade Sheen, J.-X. Shi, J. Martensson, A. N. Parikh, D.L. Allara, A New Class of Organized Self-Assembled Monolayers: Alkane Thiols on GaAs(110). *Journal of the American Chemical Society* **114**, 1514–1515 (1992).

[68] P. Fenter, P. Eisenberger, Structure of $CH_3(CH_2)_{17}SH$ Self-Assembled on the Ag(111) Surface: An Incommensurate Monolayer. *Langmuir* **7**, 2013 2016 (1991).

[69] C.M. Ruan, T. Bayer, S. Meth, C.N. Sukenik, Creation and Characterization of n-alkylthiol and n-alkylamine Self-Assembled Monolayers on 316L Stainless Steel. *Thin solid films* **419**, 95–104 (2002).

[70] N. Kaiser, Review of the Fundamentals of Thin-Film Growth. *Applied Optics* **41**, 3053 3060 (2002).

[71] J.A. Venables, Nucleation Calculations in a Pair-Binding Model. *Physical Review B* **36**, 4153–4162 (1987).

[72] J.A. Venables, G.D.T. Spiller, M. Hanbücken, Nucleation and Growth of Thin Films. *Reports on Progress in Physics* **47**, 399 459 (1984).

[73] C. Eisenmenger-Sittner, The Application of Rate Equations to Describe Nucleation and Growth on Rough Substrates: Tin and Lead on Aluminium. *Journal of Crystal Growth* **205**, 441–452 (1999).

[74] Z. Zhang, M.G. Lagally, Atomistic Processes in the Early Stages of Thin-Film Growth. *Science* **276**, 377–383 (1997).

[75] T. Sclator S. Nakahara C. Chidsey, D. Loiacono, STM Study of the Surface Morphology of Gold on Mica. *Surface Science* **200**, 45–66 (1988).

[76] J. DeRose, T. Thundat, L.A. Nagahara, S.M. Lindsay, Gold Grown Epitaxially on Mica: Conditions for Large Area Flat Faces. *Surface Science* **256**, 102 108 (1991).

[77] M. H. Dishner, M.M. Ivez, S. Gorer, J.C. Hemminger, F.J. Feher, Prepararion of Gold Thin Films by Epitaxial Growth on Mica and the Effect of Flame Annealing. *Journal of Vacuum Science and Technology A* **16**, 3295–3300 (1998).

[78] Y. Golan, L. Margulis, I. Rubinstein, Vacuum-Deposited Gold Films. *Surface Science* **264**, 312–326 (1992).

[79] M. Hegner, P. Wagner, G. Semenza, Ultralarge Atomically Flat Template-Stripped Au Surfaces for Scanning Probe Microscopy. *Surface Science* **291**, 39–46 (1993).

[80] A. Hiraki, M-A. Nicolet, J.W. Mayer, Low-Temperature Migration of Silicon in Thin Layers of Gold and Platinum. *Applied Physics Letters* **18**, 178 181 (1971).

[81] J. Hwang, M.A. Dubson, Atomically Flat Gold Films Grown on Hot Glass. *Journal of Applied Physics* **72**, 1852–1857 (1992).

[82] U. Höpfner, H. Hehl, L. Brehmer, Preparation of Ordered Thin Gold Films. *Applied Surface Science* **152**, 259 (1999).

[83] G. LeLay, Physics and Electronics of the Noble-Metal/Elemental-Semiconductor Interface Formation: a Status Report. *Surface Science* **132**, 169–204 (1983).

[84] G. LeLay, The Au/Si(111) Interface: Growth Mode, Energetics, Structural and Electronic Properties. *Journal of Crystal Growth* **54**, 551–557 (1981).

[85] T.-S. Lin, Y.-W. Chung, Measurement of the Activation Energy for Surface Diffusion in Gold by Scanning Tunneling Microscopy. *Surface Science* **207**, 539 546 (1989).

[86] X.F. Lin, J. Nogami, Au on the Si(001) surface: Room-temperature growth. *Journal of Vacuum Science Technology B* **12**, 2090 2093 (1994).

[87] X.F. Lin, K.J. Wan, J.C. Glueckstein, J. Nogami, Gold-Induced Reconstructions of the Si(001) Surface: The 5x3 and $\sqrt{26} \times 3$ phases. *Physical Review B* **47**, 3671–3676 (1993).

[88] B. Lüssem, S. Karthäuser, H. Haselier, R. Waser, The Origin of Faceting of Ultra-flat Gold Films Epitaxially Grown on Mica. *Applied Surface Science* **249**, 197–202 (2005).

[89] C. Masens, J. Schulte, M. Phillips, S. Dligatch, Ultra Flat Gold Surfaces for Use in Chemical Force Micorscopy: Scanning Probe Microscopy Studies of the Effect of Preparation Regime on Surface Morphology. *Microscopy and Microanalysis* **6**, 113 120 (2000).

[90] H. Okamato, H. Nejo, Atomically Flat Gold Film Surfaces Deposited on Si(111) Surfaces at Room Temperature. *Journal of Vacuum Science Technology B* **16**, 3013–3014 (1998).

[91] D. Porath, Z. Goldstein, A. Grazevskz, O. Millo, Scanning Tunneling Microscopy Studies of Annealing of Gold Films. *Surface Science* **321**, 81 (1994).

[92] C.I. Priest, K. Jacobs, J. Ralston, Novel Approach to the Formation of Smooth Gold Surfaces. *Langmuir* **18**, 2438–2440 (2002).

[93] A. Putnam, B. L. Blackford, M.H. Jericho, M.O. Watanabe, Surface Topography Study of Gold Deposited on Mica Using Scanning Tunneling Microscopy: Effect of Mica Temperature. *Surface Science* **217**, 276 (1989).

[94] P. Samori, J. Diebel, H. Löwe, J.P. Rabe, Template-Stripped Gold supported on Ni as a Substrate for SAMs. *Langmuir* **15**, 2592 2594 (1999).

[95] N.G. Semaltianos, E.G. Wilson, Investigation of the Surface Morphology of Thermally Evaporated Thin Gold Films on Mica, Glass, Silicon and Calcium Fluoride Substrates by Scanning Tunneling Microscopy. *Thin solid films* **366**, 111–116 (2000).

[96] P. Sobotik, I. Ostadal, Temperature Induced Change of Surface Roughness of Au(111) Epitaxial Films on Mica. *Journal of Crystal Growth* **197**, 955 962 (1999).

[97] D. Stamou, D. Gourdon, M. Liley, N.A. Burnham, A. Kulik, H. Vogel, C. Duschl, Uniformly Flat Gold Surfaces: Imaging the Domain Structure of Organic Monolayers Using Scanning Force Microscopy. *Langmuir* **13**, 2425 (1997).

[98] J. Vancea, G. Reiss, F. Schneider, K. Bauer, H. Hoffmann, Substrate Effects on the Surface Topography of Evaporated Gold Films - a Scanning Tunneling Microscopy Investigation. *Surface Science* **218**, 108–126 (1989).

[99] P. Wagner, M. Hegner, H.J. Güntherodt, G. Semenza, Formation and in Situ Modification of Monolayers Chemisorbed on Ultraflat Template-Stripped Gold Surfaces. *Langmuir* **11**, 3867 (1995).

[100] N.G. Woodard, G.P. Lafayatis, Fabrication and Characterization of Extremely Smooth Large Area Gold Surfaces. *Journal of Vacuum Science Technology A* **14**, 332–335 (1995).

[101] T. F. Young, J.F. Chang, H.Y. Ueng, Study on Annealing Effects of Au Thin Films on Si. *Thin solid films* **322**, 319–322 (1998).

[102] X.-Y. Zheng, Y. Ding, L.A. Bottomley, D.P. Allison, R. J. Warmack, Discontinuous Gold Islands Films on Mica. *Journal of Vacuum Science Technology B* **13**, 1320 1324 (1995).

[103] J. Perdereau, J.P. Biberian, G.E. Rhead, Adsorption and Surface Alloying of Lead Monolayers on (111) and (110) Faces of Gold. *J. Phys. F* **4**, 798 806 (1974).

[104] M.A. van Hove, R.J. Koestner, P.C. Stair, J.P. Biberian, L.L. Kesmodel, I. Bartos, G.A. Somorjai, The Surface Reconstructions of the (100) Crystal Faces of Iridium, Platinum and Gold. *Surface Science* **103**, 189–217 (1981).

[105] K. Takayanagi, K. Yagi, Monoatom-High Level Electron Microscopy of Metal Surfaces. *Transactions of the Japan Institute of Metals* **24**, 337 (1983).

[106] Y. Tanishiro, H. Kanamori, K. Takayanagi, K. Yagi, G. Honjo, UHV Transmission Electron Microscopy on the Reconstructed Surface of (111) Gold. *Surface Science* **111**, 395 413 (1981).

[107] K. Yagi, K. Takayanagi, K. Kobayashi, N. Osakabe, Y. Tanishiro, G. Honjo, Surface Study by an UHV Electron Microscope. *Surface Science* **86**, 174 181 (1979).

[108] J.C. Heyraud, J.J. Metois, Anomalous 1/3 422 Diffraction Spots from 111 Flat Gold Crystallites: (111) Surface Reconstruction and Moire Fringes between the Surface and the Bulk. *Surface Science* **100**, 519 528 (1980).

[109] U. Harten, A. M. Lahee, J.P. Toennies, Ch. Wöll, Observation of a Soliton Reconstruction of Au(111) by High-Resolution Helium-Atom Diffraction. *Physical Review Letters* **54**, 2619–2622 (1985).

[110] Ch. Wöll, S. Chiang, R.J. Wilson, P.H. Lippel, Determination of Atom Positions at Stacking-Fault Dislocations on Au(111) by Scanning Tunneling Microscopy. *Physical Review B* **39**, 7988–7991 (1989).

[111] J.V. Barth, H. Brune, G. Ertl, R.J. Behm, Scanning Tunneling Microscopy Observations on the Reconstructed Au(111) Surface: Atomic Structure, Long-Range Superstructure, Rotational Domains, and Surface Defects. *Physical Review B* **42**, 9307–9318 (1990).

[112] N. Shimoni, O. Biham, O. Millo, Current-Induced Surface Dislocations on Thin Gold Films. *Surface Science* **414**, L925 (1998).

[113] C. Maissen, H. Zogg, S. Blunier, A. Sultan, S. Teodoropol, T. Richmond, J.W. Tomm, G. Kostorz, . In *Mechanism of Heteroepitaxial Growth*, Bd. 263 S. 415. Materials Research Society Symposium Proceedings 1992.

[114] A.J. Moses, *The Practicing Scientists Handbook*. Van Nostrand Reinhold Company, 1978. p. 1126.

[115] J. C. Love, L. A. Estroff, J. K. Kriebel, R.G. Nuzzo, G. M. Whitesides, Self-Assembled Monolayers of Thiolates on Metals as a Form of Nanotechnology. *Chemical Review* **105**, 1103–1169 (2005).

[116] C.D. Bain, G.M. Whitesides, Formation of Two-Component Surfaces by the Spontaneous Assembly of Monolayers on Gold from Solutions Containing Mixtures of Organic Thiols. *Journal of the American Chemical Society* **110**, 6560–6561 (1988).

[117] S.V. Arte, B. Liedberg, D.L. Allara, Chain Length Dependence of the Structure and Wetting Properties in Binary Composition Monolayers of OH- and CH3-Terminated Alkanethiolates on Gold. *Langmuir* **11**, 3882–3893 (1995).

[118] S. Morgenthaler, S. Lee, S. Zürcher, N.D. Spencer, A Simple, Reproducible Approach to the Preparation of Surface-Chemical Gradients. *Langmuir* **19**, 10459–10462 (2003).

[119] R. Yamada, H. Tada, Manipulation of Droplets by Dynamically Controlled Wetting Gradients. *Langmuir* **21**, 4254–4256 (2005).

[120] J. Scherer, M.R. Vogt, O.M. Magnussen, R.J. Behm, Corrosion of Alkanethiol-Covered Cu(100) Surfaces in Hydrochloric Acid Solution Studied by in-Situ Scanning Tunneling Microscopy. *Langmuir* **13**, 7045 7051 (1997).

[121] K.L. Prime, G.M. Whitesides, Self-Assembled Organic Monolayers - Model Systems for Studying Adsorption of Proteins at Surfaces. *Science* **252**, 1164 1167 (1991).

[122] A. Kumar, G.M. Whitesides, Features of Gold Having Micrometer to Centimeter Dimensions Can be Formed Through a Combination of Stamping with an Elastomeric Stamp and an Alkanethiol "Ink" Followed by Chemical Etching. *Applied Physics Letters* **63**, 2002–2004 (1993).

[123] K.B. Blodgett, Films Built by Depositing Successive Monomolecular Layers on a Solid Surface. *Journal of the American Chemical Society* **57**, 1007 (1935).

[124] K.B. Blodgett, I. Langmuir, Built-Up Films of Barium Stearate and Their Optical Properties. *Physical Review* **51**, 964 (1937).

[125] unknown, Monolayer films that assemble themselves. *New Scientist* **98**, 20 (1983).

[126] Tomi T.-T. Li, H. Y. Liu, M.J. Weaver, Intramolecular Electron Transfer at Metal Surfaces. 3. Influence of Bond Conjugation on Reduction Kinetics of Cobalt(III) Anchored to Electrodes via Tiophenecarboxylate Ligands. *Journal of the American Chemical Society* **106**, 1233–1239 (1984).

[127] Tomi T.-T. Li, M.J. Weaver, Intramolecular Electron Transfer at Metal Surfaces.4. Dependence of Tunneling Probability upon Donor-Acceptor Separation Distance. *Journal of the American Chemical Society* **106**, 6107–6108 (1984).

[128] R. G. Nuzzo, F. A. Fusco, D. L. Allara, Spontaneously Organized Molecular Assemblies 3. Preparation and Properties of Solution Adsorbed Monolayers of Organic Disulfides on Gold Surfaces. *Journal of the American Chemical Society* **109**, 2358 2368 (1987).

[129] H. O. Finklea, S. Avery, M. Lynch, Blocking Oriented Monolayers of Alkyl Mercaptans on Gold Electrodes. *Langmuir* **3**, 409–413 (1987).

[130] R. G. Nuzzo, B. R. Zegarski, L. H. Dubois, Fundamental Studies of the Chemisorption of Organosulfur Compounds on Au(111). Implications for Molecular Self-Assembly on Gold Surfaces. *Journal of the American Chemical Society* **109**, 733–740 (1987).

[131] P. Fenter, P. Eisenberger, K.S. Liang, Chain-Length Dependence of the Structures and Phases of $\boldsymbol{CH_3(CH_2)_{n-1}SH}$ Self-Assembled on Au. *Physical Review Letters* **70**, 2447 1450 (1993).

[132] M.D. Porter, T.B. Bright, D.L. Allara, C.E. Chidsey, Spontaneously Organized Molecular Assemblies. 4. Structural Characterization of n-Alkyl Thiol Monolayers on Gold by Optical Ellipsometry, Infrared Spectroscopy, and Electrochemistry. *Journal of the American Chemical Society* **109**, 3559–3568 (1987).

[133] C.D. Bain, E.B. Troughton, Y.-T. Tao, J. Evall, G.M. Whitesides, R.G. Nuzzo, Formation of Monolayer Films by the Spontaneous Assembly of Organic Thiols from Solution onto Gold. *Journal of the American Chemical Society* **111**, 321–335 (1989).

[134] R. G. Nuzzo, L.H. Dubois, D. L. Allara, Fundamental Studies of Microscopic Wetting on Organic Surfaces. 1. Formation and Structural Characterization of a Self-Consistent Series of Polyfunctional Organic Monolayers. *Journal of the American Chemical Society* **112**, 558–569 (1990).

[135] L. Strong, G.M. Whitesides, Structures of Self-Assembled Monolayer Films of Organosulfur Compounds Adsorbed on Gold Single Crystals: Electron Diffraction Studies. *Langmuir* **4**, 546–558 (1988).

[136] C. E. D. Chidsey, G.-Y. Liu, P. Rowntree, G. Scoles, Molecular Order at the Surface of an Organic Monolayer Studied by Low Energy Helium Diffraction. *Journal of Chemical Physics* **91**, 4421–4423 (1989).

[137] N. Camillone III, C.E.D. Chidsey, G.-Y. Liu, T.M. Putvinski, G. Scoles, Surface Structure and Thermal Motion of n-Alkane Thiols Self-Assembled on Au(111) Studied by Low Energy Helium Diffraction. *Journal of Chemical Physics* **94**, 8493–8501 (1991).

[138] C.E.D. Chidsey, D.N. Loiacono, Chemical Functionality in Self -Assembled Monolayers: Structural and Electrochemical Properties. *Langmuir* **6**, 682 (1990).

[139] R. G. Nuzzo, E.M. Korenic, L. H. Dubois, Studies of the Temperature-Dependent Phase Behavior of Long Chain n-Alkyl Thiol Monolayers on Gold. *Journal of Chemical Physics* **93**, 767–773 (1990).

[140] N. Camillone III, C.E.D. Chidsey, G.-Y. Liu, G. Scoles, Superlattice Structure at the Surface of a Monolayer of Octadecanethiol Self-Assembled on Au(111). *Journal of Chemical Physics* **98**, 3503 3511 (1993).

[141] C.A. Widrig, C.A. Alves, M. D. Porter, Scanning Tunneling Microscopy of Ethanethiolate and n-Octadecanthiolate Monolayers Spontaneously Adsorbed at Gold Surfaces. *Journal of the American Chemical Society* **113**, 2805 2810 (1991).

[142] C. A. Alves, E.L. Smith, M.D. Porter, Atomic Scale Imaging of Alkanethiolate Monolayers at Gold Surfaces with Atomic Force Microscopy. *Journal of the American Chemical Society* **114**, 1222 1227 (1992).

[143] G.E. Poirier, M.J. Tarlov, The c(4x2) Superlattice of n-Alkanethiol Monolayers Self Assembled on Au(111). *Langmuir* **10**, 2853–2856 (1994).

[144] E. Delamarche, B. Michel, Ch. Gerber, D. Anselmetti, H.-J. Güntherodt, H. Wolf, H. Ringsdorf, Real-Space Observation of Nanoscale Molecular Domains in Self-Assembled Monolayers. *Langmuir* **10**, 2869–2871 (1994).

[145] E. Delamarche, B. Michel, H.A. Biebuyck, C. Gerber, Golden Interfaces: The Surface of Self-Assembled Monolayers. *Advanced Materials* **8**, 719–729 (1996).

[146] K. Kobayashi, H. Yamada, T. Horiuchi, K. Matsushige, The Molecular Arrangements of Alkanethiol Self-Assembled Monolayers on Au(111) Studied by Scanning Tunneling Microscopy. *Japanese Journal of Applied Physics* **37**, 6183–6185 (1998).

[147] T. Fukuma, T. Ichii, K. Kobayashi, H. Yamada, K. Matsushige, Molecular-Scale Noncontact Atomic Force Microscopy Contrasts in Topography and Energy Dissipation on c(4x2) Superlattice Structures of Alkanethiol Self-Assembled Monolayers. *Journal of Applied Physics* **95**, 1222–1226 (2004).

[148] P. Fenter, A. Eberhardt, P. Eisenberger, Self-Assembly on n-Alkyl Thiols as Disulfides on Au(111). *Science* **266**, 1216–1218 (1994).

[149] M. S. Yeganeh, S.M. Dougal, R.S. Polizzotti, P. Rabinowitz, Interfacial Atomic-Structure of a Self-Assembled Alkyl Thiol Monolayer Au(111)- A Sum-Frequency Generation Study. *Physical Review Letters* **74**, 1811–1814 (1995).

[150] P. Fenter, F. Schreiber, L. Berman, G. Scoles, P. Eisenberger, M.J. Bedzyk, On the Structure and Evolution of the Buried S/Au Interface in Self-Assembled Monolayers: X-ray Standing Wave Results. *Surface Science* **412/413**, 213–235 (1998).

[151] H. S. Kato, J. Noh, M. Hara, M. Kawai, An HREELS Study of Alkanethiol Self-Assembled Monolayers on Au(111). *Journal of Physical Chemistry B* **106**, 9655–9658 (2002).

[152] N. Camillone III, P. Eisenberger, T.Y.B. Leung, P. Schwartz, G. Scoles, G.E. Poirier, M.J. Tarlov, New Monolayer Phases of n-Alkane Thiols Self-Assembled on Au(111): Preparation, Surface Characterization, and Imaging. *Journal of Chemical Physics* **101**, 11031 11035 (1994).

[153] G.E. Poirier, E.D. Pylant, The Self-Assembly Mechanism of Alkanethiols on Au(111). *Science* **272**, 1145 1148 (1996).

[154] G. E. Poirier, Characterization of Organosulfur Molecular Monolayers on Au(111) using Scanning Tunneling Microscopy. *Chemical Review* **97**, 1117 (1997).

[155] Lars Müller-Meskamp, Charakterisierung von in einer SAM Hostmatrix immobilisierten funktionalen Molekülen mittels Rastersondenmethoden. RWTH Aachen, Germany, 2004.

[156] Y. Nakamura, Y. Mera, K. Maeda, A Reproducible Method to Fabricate Atomically Sharp Tips for Scanning Tunneling Microscopy. *Review of Scientific Instruments* **70**, 3373–3376 August 1999.

[157] J.P. Ibe, P.P. Bey Jr., S.L. Brandow, R.A. Brizzolara, N.A. Burnham, D.P. DiLella, K.P. Lee, C.R.K. Marrian, R.J.Colton, On the Electrochemical Etching of Tips for Scanning Tunneling Microscopy. *Journal of Vacuum Science & Technology A: Vacuum, Surfaces, and Films* **8**, 3570–3575 July 1990.

[158] O. Cavalleri, A. Hirstein, K. Kern, Ostwald Ripening of Vacancy Islands at Thiol Covered Au(111). *Surface Science* **340**, L960–L964 (1995).

[159] J.-P. Bucher, L. Santesson, K. Kern, Thermal Healing of Self-Assembled Organic Monolayers: Hexane- and Octadecanethiol on Au(111) and Ag(111). *Langmuir* **10**, 979–983 (1994).

[160] C. Schönenberger, J.A.M. Sondag-Huethorst, J. Jorritsma, L.G.J. Fokkink, What are the "Holes" in Self-Assembled Monolayers of Alkanethiols on Gold? *Langmuir* **10**, 611 614 (1994).

[161] R. L. McCarley, D.J. Dunaway, R. J. Willicut, Mobility of the Alkanethiol-Gold(111) Interface Studied by Scanning Probe Microscopy. *Langmuir* **9**, 2775–2777 (1993).

[162] U. Düring, O. Züger, B. Michel, L. Häussling, H. Ringsdorf, Electronic and Mechanical Characterization of Self-Assembled Alkanethiol Monolayers by Scanning Tunneling Microscopy Combined with Interaction-Force-Gradient Sensing. *Physical Review B* **48**, 1711 1717 (1993).

[163] W. Mizutani, B. Michel, R. Schierle, H. Wolf, H. Rohrer, Scanning Surface Harmonic Microscopy of Self-Assembled Monolayers on Gold. *Applied Physics Letters* **63**, 147–149 (1993).

[164] K. Edinger, A. Gölzhäuser, K. Demonta, C. Wöll, M. Grunze, Formation of Self-Assembled Monolayers of n-Alkanethiols on Gold: A Scanning Tunneling Microscopy Study on the Modification of Substrate Morphology. *Langmuir* **9**, 4–8 (1993).

[165] Y.-T. Kim, A. J. Bard, Imaging and Etching of Self-Assembled n-Octadecanethiol Layers on Gold with the Scanning Tunneling Microscope. *Langmuir* **8**, 1096–1102 (1992).

[166] L. Sun, R.M. Crooks, Imaging of Defects Contained within n-Alkylthiol Monolayers by Combination of Underpotential Deposition and Scanning Tunneling Microscopy: Kinetics of Self-Assembly. *Journal of the Electrochemical Society* **138**, L23–L25 (1991).

[167] G.E. Poirier, Mechanism of Formation of Au Vacancy Islands in Alkanethiol Monolayers. *Langmuir* **13**, 2019–2026 (1997).

[168] E. Delamarche, B. Michel, H. Kang, C. Gerber, Thermal Stability of Self-Assembled Monolayers. *Langmuir* **10**, 4103–4108 (1994).

[169] L.A. Bumm, J.J. Arnold, L.F. Charles, T.D. Dunbar, D.L. Allara, P.S. Weiss, Directed Self-Assembly to Create Molecular Terraces with Molecularly Sharp Boundaries in Organic Monolayers. *Journal of the American Chemical Society* **121**, 8017–8021 (1999).

[170] L. Müller-Meskamp, Björn Lüssem, S. Karthäuser, R. Waser, Rectangular ($\mathbf{3 \times \sqrt{3}}$)Superlattice of a Dodecanethiol Self-Assembled Monolayer on Au(111) Observed by Ultra-High-Vacuum Scanning Tunneling Microscopy. *Journal of Physical Chemistry B* **109**, 11424–11426 (2005).

[171] H. Kondoh, C. Kodama, H. Sumida, H. Nozoye, Molecular Processes of Adsorption and Desorption of Alkanethiol Monolayers on Au(111). *Journal of Chemical Physics* **111**, 1175–1184 (1999).

[172] B. Lüssem, L. Müller-Meskamp, S. Karthäuser, R. Waser, A New Phase of the c(4x2) Superstructure of Alkanethiols Grown by Vapor Phase Deposition on Gold. *Langmuir* **21**, 5256–5258 (2005).

[173] S. Frey, H.-T. Rong, K. Heister, Y.-J. Yang, M. Buck, M. Zharnikov, Response of Biphenyl-Substituted Alkanethiol Self-Assembled Monolayers to Electron Irradiation: Damage Suppression and Odd-Even Effects. *Langmuir* **18**, 3142–3150 (2002).

[174] G. Yang, Y. Qian, C. Engtrakul, L.R. Sita, G.-Y. Liu, Arenethiols Form Ordered and Incommensurate Self-Assembled Monolayers on Au(111) Surfaces. *Journal of Physical Chemistry B* **104**, 9059 9062 (2000).

[175] A.-A. Dhirani, R.W. Zehner, R.P. Hsung, P. Guyot-Sionnest, L. R. Sita, Self-Assembly of Conjugated Molecular Rods: A High-Resolution STM Study. *Journal of the American Chemical Society* **118**, 3319 3320 (1996).

[176] A. Bilic, J.R. Reimers, N.S. Hush, The Structure, Energetics, and Nature of the Chemical Bonding of Phenylthiol Adsorbed on the Au(111) Surface: Implications

for Density-Functional Calculations of Molecular-Electronic Conduction. *Journal of Chemical Physics* **122**, 094708 (2005).

[177] S. Frey, V. Stadler, K. Heister, W. Eck, M. Zharnikov, M. Grunze, Structure of Thioaromatic Self-Assembled Monolayers on Gold and Silver. *Langmuir* **17**, 2408–2415 (2001).

[178] J.F. Kang, A. Ulman, S. Liao, R. Jordan, G. Yang, G.-Y. Liu, Self-Assembled Rigid Monolayers of 4'-Substituted-4-mercaptobiphenyls on Gold and Silver Surfaces. *Langmuir* **17**, 95–106 (2001).

[179] W. Eck, V. Stadler, W. Geyer, M. Zharnikov, A. Gölzhäuser, M.l Grunze, Generation of Surface Amino Groups on Aromatic Self-Assembled Monolayers by Low Energy Electron Beams: First Step Towards Chemical Lithography. *Advanced Materials* **11**, 805–808 (2000).

[180] T.Y.B. Leung, P. Schwartz, G. Scoles, F. Schreiber, A. Ulman, Structure and Growth of 4-methyl-4'-mercaptobiphenyl Monolayers on Au(111): a Surface Diffraction Study. *Surface Science* **458**, 34 52 (2000).

[181] W. Geyer, V. Stadler, W. Eck, M. Zharnikov, A. Gölzhäuser, M. Grunze, Electron-Induced Crosslinking of Aromatic Self-Assembled Monolayers: Negative Resists for Nanolithography. *Applied Physics Letters* **75**, 2401–2403 (1999).

[182] W. Azzam, C. Fuxen, A. Birkner, H.-T. Rong, M. Buck, C. Wöll, Coexistence of Different Structural Phases in Thioaromatic Monolayers on Au(111). *Langmuir* **19**, 4958–4968 (2003).

[183] K. Heister, M. Zharnikov, M. Grunze, L. S. O. Johansson, Adsorption of Alkanethiols and Biphenylthiols on Au and Ag Substrates: A High-Resolution X-ray Photoelectron Spectroscopy Study. *Journal of Physical Chemistry B* **105**, 4058–4061 (2001).

[184] Y.-H. Kim, S.S. Jang, W.A. Goddard III, Conformations and Charge Transport Characteristics of Biphenyldithiol Self-Assembled-Monolayer Molecular Electronic Devices: A Multiscale Computational Study. *Journal of Chemical Physics* **122**, 244703– (2005).

[185] H.-J. Himmel, A. Terfort, C. Wöll, Fabrication of a Carboxyl-Terminated Organic Surface with Self-Assembly of Functionalized Terphenylthiols: The Importance of Hydrogen Bond Formation. *Journal of the American Chemical Society* **120**, 12069–12074 (1998).

[186] Y.-T. Tao, C.-C. Wu, J.-Y. Eu, W.-L. Lin, Structure Evolution of Aromatic-Derivatized Thiol Monolayers on Evaporated Gold. *Langmuir* **13**, 4018 4023 (1997).

[187] H.-T. Rong, S. Frey, Y.-J. Yang, M. Zharnikov, M. Buck, M. Wühn, C. Wöll, G. Helmchen, On the Importance of the Headgroup Substrate Bond in Thiol Monolayers: A Study of Biphenyl-Based Thiols on Gold and Silver. *Langmuir* **17**, 1582–1593 (2001).

[188] M. Zharnikov, S. Frey, H. Rong, Y.-J. Yang, K. Heister, M. Buck, M. Grunze, The Effect of Sulfur-Metal Bonding on the Structure of Self-Assembled Monolayers. *Physical Chemistry, Chemical Physics* **2**, 3359–3362 (2000).

[189] T. Felgenhauer, H.-T. Rong, M. Buck, Electrochemical and Exchange Studies of Self-Assembled Monolayers of Biphenyl Based Thiols on Gold. *Journal of Electroanalytical Chemistry* **550-551**, 309–319 (2003).

[190] Y.-T. Long, H.-T. Rong, M. Buck, M. Grunze, Odd–Even Effects in the Cyclic Voltammetry of Self-Assembled Monolayers of Biphenyl Based Thiols. *Journal of Electroanalytical Chemistry* **524-525**, 62–67 (2002).

[191] P. Cyganik, M. Buck, J.D.E.T. Wilton-Ely, C. Wöll, Stress in Self-Assembled Monolayers: ω-Biphenyl Alkane Thiols on Au(111). *Journal of Physical Chemistry B* **109**, 10902–10908 (2005).

[192] P. Cyganik, M. Buck, Polymorphism in Biphenyl-Based Self-Assembled Monolayers of Thiols. *Journal of the American Chemical Society* **126**, 5960–5961 (2004).

[193] P. Cyganik, M. Buck, W. Azzam, C. Wöll, Self-Assembled Monolayers of ω-Biphenylalkanethiols on Au(111): Influence of Spacer Chain on Molecular Packing. *Journal of Physical Chemistry B* **108**, 4989–4996 (2004).

[194] W. Azzam, P. Cyganik, G. Witte, M. Buck, Ch. Wöll, Pronounced Odd-Even Changes in the Molecular Arrangement and Packing Density of Biphenyl-Based Thiol SAMs: A Combined STM and LEED Study. *Langmuir* **19**, 8262–8270 (2003).

[195] J. Trotter, The Crystal and Molecular Structure of Biphenyl. *Acta Crystallographica* **14**, 1135–1140 (1961).

[196] W. Azzam, *Self-Assembled Monolayers on Gold Made from Organothiols Containing an Oligophenyl-Backbone*. Ruhr-Universität Bochum, Germany, 2003.

[197] C. Fuxxen, *Adsorption, Struktur und Desorption von Organothiolaten auf Goldsubstraten.* Ruhr-Universität Bochum, 2001.

[198] T. Wandlowski, personal communication.

[199] S. Hong, R. Reifenberger, W. Tian, S. Datta, J. Henderson, C.P. Kubiak, Molecular Conductance Spectroscopy of Conjugated, Phenyl-Based Molecules on Au(111): the Effect of End Groups on Molecular Conduction. *Superlattices and Microstructures* **28**, 289–303 (2000).

[200] R. E. Holmlin, R. F. Ismagilov, R. Haag, V. Mujica, M. A. Ratner, M. A. Rampi, G. M. Whitesides, Correlating Electron Transport and Molecular Structure in Organic Thin Films. *Angewandte Chemie International Edition* **113**, 2378–2382 (2001).

[201] Y. Yasutake, Y. Azuma, K. Nagano, Y. Majima, Tunneling Current-Distance Characteristic of Scanning Vibrating Probe/ 1-Alkanethiol Self-Assembled Monolayer (SAM)/ Au (111) Structure. *Mat. Res. Soc. Symp. Proc.* **782**, 17–21 (2004).

[202] S. Chen, L. Li, C.L. Boozer, S. Jiang, Controlled Chemical and Structural Properties of Mixed Self-Assembled Monolayers of Alkanethiols on Au(111). *Langmuir* **16**, 9287–9293 (2000).

[203] C.D. Bain, G.M Whitesides, Formation of Monolayers by the Coadsorption of Thiols on Gold: Variation in the Length of the Alkyl Chain. *Journal of the American Chemical Society* **111**, 7164 7175 (1989).

[204] T. Takami, E. Delamarche, B. Michel, Ch. Gerber, H. Wolf, H. Ringsdorf, Recognition of Individual Tail Groups in Self-Assembled Monolayers. *Langmuir* **11**, 3876–3881 (1995).

[205] L. Li, S. Cheng, S. Jiang, Molecular-Scale Mixed Alkanethiol Monolayers of Different Terminal Groups on Au(111) by Low-Current Scanning Tunneling Microscopy. *Langmuir* **19**, 3266–3271 (2003).

[206] R.K. Smith, S.M. Reed, P.A. Lewis, J.D. Monnel, R.S. Clegg, K.F. Kelly, L.A. Bumm, J.E. Hutchison, P.S. Weiss, Phase Separation Within a Binary Self-Assembled Monolayer on Au(111) Driven by an Amide-Containing Alkanethiol. *Journal of Physical Chemistry B* **105**, 1119 (2001).

[207] A.V. Shevade, J. Zhou, M.T. Zin, S. Jiang, Phase Behavior of Mixed Self-Assembled Monolayers of Alkanethiols on Au(111): A Configurational-Bias Monte Carlo Simulation Study. *Langmuir* **17**, 7566 (2001).

[208] S. Chen, L. Li, C.L. Boozer, S. Jiang, Controlled Chemical and Structural Properties of Mixed Self-Assembled Monolayers by Coadsorption of Symmetric and Asymmetric Disulfides on Au(111). *Journal of Physical Chemistry B* **105**, 2975 (2001).

[209] M.T. Cygan, T.D. Dunbar, J.J. Arnold, L.A. Bumm, N.F. Shedlock, T.P. Burgin, L. Jones II, J.J. Jackiw, J.M. Tour, P.S. Weiss, Insertion, Conductivity, and Structures of Conjugated Organic Oligomers in Self-Assembled Alkanethiol Monolayers on Au111. *Journal of the American Chemical Society* **120**, 2721–2732 (1998).

[210] T.D. Dunbar, M.T. Cygan, L.A. Bumm, G.S. McCarty, T.P. Burgin, W.A. Reinerth, L. Jones II, J.J. Jackiw, J.M. Tour, P.S. Weiss, D.L. Allara, Combined Scanning Tunneling Microscopy and Infrared Spectroscopic Characterization of Mixed Surface Assemblies of Linear Conjugated Guest Molecules in Host Alkanethiolate Monolayers on Gold. *Journal of Physical Chemistry B* **104**, 4880–4893 (2000).

[211] S. Wakamatsu, U. Akiba, M. Fujihira, Electronic Tunneling Through a Single Molecule Embedded in Self-Assembled Monolayer Matrices. *Colloids and Surfaces A* **198**, 785–790 (2002).

[212] A. Nakasa, U. Akiba, M. Fujihira, Self-Assembled Monolayers Containing Biphenyl Derivatives as Challenge for nc-AFM. *Applied Surface Science* **157**, 326–331 (2000).

[213] K. Moth-Poulsen, L. Patrone, N. Stuhr-Hansen, J.B. Christensen, J.-P. Bourgoin, T. Bjørnholm, Probing the Effects of Conjugation Path on the Electronic Transmission through Single Molecules Using Scanning Tunneling Microscopy. *Nano Letters* **5**, 783–785 (2005).

[214] A. Szuchmacher Blum, T. Ren, D.A. Parish, S.A. Trammell, M.H. Moore, J. G. Kushmerick, G.-L. Xu, J.R. Deschamps, S.K. Pollack, R. Sashidhar, $Ru_2(ap)_4(\sigma$-oligo(phenyleneethynyl)) Molecular Wires: Synthesis and Electronic Characterization. *Journal of the American Chemical Society* **127**, 10010–10011 (2005).

[215] T. Ishida, W. Mizutani, N. Choi, U. Akiba, M. Fujihira, H. Tokumoto, Structural Effects on Electrical Conduction of Conjugated Molecules Studied by Scanning Tunneling Microscopy. *Journal of Physical Chemistry B* **104**, 11680–11686 (2000).

[216] T. Ishida, W. Mizutani, H. Tokumoto, N. Choi, U. Akiba, M. Fujihira, Insertion Process and Electrical Conduction of Conjugated Molecules in n-Alkanethiol Self-Assembled Monolayers on Au(111). *Journal of Vacuum Science Technology A* **18**, 1437–1442 (2000).

[217] M. Magoga, C. Joachim, Conductance and Transparence of Long Molecular Wires. *Physical Review B* **56**, 4722 4729 (1997).

[218] A. Bandyopadhyay, A. J. Pal, Multilevel Conductivity and Conductance Switching in Supramolecular Structures of an Organic Molecule. *Applied Physics Letters* **84**, 999–1001 (2004).

[219] A. Bandyopadhyay, A. J. Pal, Large Conductance Switching and Memory Effects in Organic Molecules for Data-Storage Applications. *Applied Physics Letters* **82**, 1215–1217 (2003).

[220] A. Bandyopadhyay, A. J. Pal, Large Conductance Switching and Binary Operation in Organic Devices: Role of Functional Groups. *Journal of Physical Chemistry B* **107**, 2531 2536 (2003).

[221] A. Bandyopadhyay, A.J. Pal, Memory-Switching Phenomenon in Acceptor-Rich Organic Molecules: Impedance Spectroscopic Studies. *Journal of Physical Chemistry B* **109**, 6084–6088 (2005).

[222] S.K. Majee, A. Bandyopadhyay, A.J. Pal, Electrical Bistability in Molecular Films: Transition from Memory to Threshold Switching. *Chemical Physics Letters* **399**, 284–288 (2004).

[223] A. Szymanski, D.C. Larson, M.M. Labes, A Temperature-Independent Conducting State in Tetracene Thin Film. *Applied Physics Letters* **14**, 88–90 (1968).

[224] A.R. Elsharkawi, K.C. Kao, Switching and Memory Phenomena in Anthracene Thin Films. *Journal of Physical Chemistry Solids* **38**, 95–96 (1977).

[225] D. Ma, M. Aguiar, J. A. Freire, I.A. Hümmelgen, Organic Reversible Switching Devices for Memory Applications. *Advanced Materials* **12**, 1063–1066 (2000).

[226] J. Taylor, M. Brandbyge, K. Stokbro, Conductance Switching in a Molecular Device: The Role of Side Groups and Intermolecular Interactions. *Physical Review B* **68**, 121101 (2003).

[227] M.A. Reed, J. Chen, A.M. Rawlett, J.M. Tour, Molecular Random Access Memory Cell. *Applied Physics Letters* **78**, 3735–3737 (2001).

[228] Z.J. Donhauser, B.A. Mantooth, T.P. Pearl, K.F. Kelly, S. U. Nanayakkara, P.S. Weiss, Matrix-Mediated Control of Stochastic Single Molecule Conductance Switching. *Japanese Journal of Applied Physics* **41**, 4871–4877 (2002).

[229] Z.J. Donhauser, B.A. Mantooth, K.F. Kelly, L.A. Bumm, J.D. Monnell, J.J. Stapleton, D.W. Price Jr., A.M. Rawlett, D.L. Allara, J.M. Tour, P.S. Weiss, Conductance Switching in Single Molecules Through Conformational Changes. *Science* **292**, 2303–2307 (2001).

[230] J. Chen, M.A. Reed, A.M. Rawlett, J.M. Tour, Large On-Off Ratios and Negative Differential Resistance in a Molecular Electronic Device. *Science* **286**, 1550 1552 (1999).

[231] T. Tsujioka, H. Kondo, Organic Bistable Molecular Memory using Photochromic Diarylethene. *Applied Physics Letters* **83**, 937–939 (2003).

[232] F. Moresco, G. Meyer, K.-H. Rieder, H. Tang, A. Gourdon, C. Joachim, Conformational Changes of Single Molecules Induced by Scanning Tunneling Microscopy Manipulation: A Route to Molecular Switching. *Physical Review Letters* **86**, 672 675 (2001).

[233] C.P. Collier, E.W. Wong, M. Belohradsky, F.M. Raymo, J.F. Stoddart, P.J. Kuekes, R.S. Williams, J.R. Heath, Electronically Configurable Molecular-Based Logic Gates. *Science* **285**, 391–394 (1999).

[234] F. L. E. Jakobsson, X. Crispin, M. Berggren, Towards Addressable Organic Impedance Switch Devices. *Applied Physics Letters* **87**, 063503 063505 (2005).

[235] V.S. Shirodkar, A.G. Chourey, Bistable Switching in Al/Al2O3/Al devices. *Journal of Materials Science Letters* **7**, 1235 1236 (1988).

[236] S. Seo, M.J. Lee, D.H. Seo, E.J. Jeoung, D.S. Suh, Y.S. Joung, I.K. Yoo, I.R. Hwang, S.H. Kim, I.S. Byun, J.-S. Kim, J.S. Choi, B.H. Park, Reproducible Resistance Switching in Polycrystalline NiO Films. *Applied Physics Letters* **85**, 5655 5657 (2004).

[237] P.E. Schmidt, C.Davila, P. Esqueda, R. Callarotti, Memory Switching in Al-Al2O3-Al Thin Film Devices. *Journal of Solid State Chemistry* **12**, 293 (1975).

[238] G.S. Nadkarni, V.S. Shirodkar, Experiments and Theory for Switching in Al/V2O5/Al Devices. *Thin Solid Films* **105**, 115 129 (1983).

[239] K. Gloos, P.J. Koppinen, J.P. Pekola, Properties of Native Ultrathin Aluminium Oxide Tunnel Barriers. *Journal of Physics: Condensed Matter* **15**, 1733 1746 (2003).

[240] G. Dearnaley, A.M. Stoneham, D.V. Morgan, Electrical Phenomena in Amorphous Oxide Films. *Reports on Progress in Physics* **33**, 1129–1191 (1970).

[241] I.G. Baek, M.S. Lee, S.O. Park, H.S. Kim, U-In Chung, S. Seo, M.J. Lee, D.H. Seo, D.-S. Suh, J.C. Park, I.K. Yoo, J.T. Moon, Highly Scalable Non-volatile Resistive Memory using Simple Binary Oxide Driven by Asymmetric Unipolar Voltage Pulses. *IEDM Tech. Dig.* 587 – 590 (2004).

[242] A.A. Ansari, A. Qadeer, Memory Switching in Thermally Grown Titanium Oxide Films. *J.Phys.D.: Appl. Phys* **18**, 911 917 (1985).

[243] C.N. Lau, D.R. Stewart, R.S. Williams, M. Bockrath, Direct Observation of Nanoscale Switching Centers in Metal/Molecule/Metal Structures. *Nano Letters* **4**, 569–572 (2004).

[244] M. Schaer, F. Nüesch, D. Berner, W. Leo, L. Zuppiroli, Water Vapor and Oxygen Degradation Mechanisms in Organic Light Emitting Diodes. *Advanced Functional Materials* **11**, 116 121 (2001).

[245] H.J. DeWit, C. Crevecoeur, The Dielectric Breakdown of Anodic Aluminium Oxide. *Physics Letters* **50A**, 365 366 (1974).

[246] J. Paczkowski, D.C. Neckers, Polymer-Based Sensitizers for the Formation of Singlet Oxygen. New Studies of Polymeric Derivatives of Rose Bengal. *Macromolecules* **18**, 1245–1253 (1985).

[247] J. Paczkowski, D.C. Neckers, Photochemical Properties of Rose Bengal. 11. Fundamental Studies in Heterogeneous Energy Transfer. *Macromolecules* **18**, 2412–2418 (1985).

[248] B. Lüssem, L. Müller-Meskamp, S. Karthäuser, R. Waser, Melanie Homberger, Ulrich Simon, A STM Study of Mixed Alkanethiol/Biphenylthiol Self Assembled Monolayers on Au(111). *Langmuir* submitted.

[249] B. Lüssem, M. Alba, S. Karthäuser, S. Kronholz, M. Weides, R. Waser, Resistive Switching of Devices Based on Thin Films of Rose Bengal: a Molecular Effect? **in preparation**.

[250] C. Zhou, M. R. Deshpande, M. A. Reed, L. Jones II, J. M. Tour, Nanoscale Metal/Self-Assembled Monolayer/Metal Heterostructures. *Applied Physics Letters* **71**, 611–613 (1997).

[251] E. Ruttkowski, *Molecular Electronics*. RWTH Aachen, 2005.

[252] N.A. Melosh, A. Boukai, F. Diana, B. Gerardot, A. Badolato, P. M. Petroff, J. R. Heath, Ultrahigh-Density Nanowire Lattices and Circuits. *Science* **300**, 112 115 (2003).

[253] M. D. Austin, H. Ge, W. Wu, M. L, Z. Yu, D. Wasserman, S. A. Lyon, Stephen Y. Chou, Fabrication of 5 nm Linewidth and 14 nm Pitch Features by Nanoimprint Lithography. *Applied Physics Letters* **84**, 5299–5301 (2004).

Schriften des Forschungszentrums J lich
Reihe Informationstechnik / Information Technology

1. **SAM - Untersuchung von Aushandlungen in Gruppen mittels Agentensimulation**
   von N. Lepperhoff (2002), VI, 278 Seiten
   ISBN: 3-89336-298-3

2. **Praxisbezogene IDL-Programmierung**
   von M. Busch, R. Bauer, H. Heer, M. Wagener (2002), XVI, 216 Seiten, 12 farb. Abb.
   ISBN: 3-89336-308-4

3. **Segmentierung von Volumendatens tzen mittels dreidimensionaler hierarchischer Inselstrukturen**
   von J.-F. Vogelbruch (2002), V, 191 Seiten, zahlr. farb. Abb.
   ISBN: 3-89336-309-2

4. **ComputerMathematik mit Maple**
   von J. Grotendorst (2003), VI, 274 Seiten mit beiliegender CD-ROM, zahlr. farb. Abb.
   ISBN: 3-89336-325-4

5. **ComputerMathematik mit Maple – Zweite berarbeitete und erweiterte Auflage**
   von J. Grotendorst (2004), VI, 294 Seiten mit beiliegender CD-ROM, zahlr. farb. Abb.
   ISBN: 3-89336-354-8

6. **The Internet in Germany: Atlas of Providers and Regions**
   by N. Lepperhoff, W. Fischer (2004), VIII, 103 pages, many coloured fig.
   ISBN: 3-89336-358-0

7. **St rstellen in Galliumnitrid-basierenden Transistoren**
   von M.J. Wolter (2004), V, 132 Seiten, 19 farb. Abb.
   ISBN: 3-89336-361-0

8. **Programming in C++: Audio-Visual Lecture of the course "Object-oriented programming in C++"**
   von B. Mohr, M. Boltes, R. Koschmieder (2004), DVD (18 hours, 22 minutes recorded in 15 sessions)
   ISBN: 3-89336-369-6

9. **Fabrication and characterization of planar Gunn diodes for Monolithic Microwave Integrated Circuits**
   by S. Montanari (2005), c. 150 pages, 26 col. fig.
   ISBN: 3-89336-396-3

10. **IDL Referenz der ICG-Daten-Struktur**
    von R. Bauer (2006), XIV, 130 Seiten
    ISBN: 3-89336-426-9

Schriften des Forschungszentrums J lich
Reihe Informationstechnik / Information Technology

11. **Piezoresponse Force Microscopy and Surface Effects of Perovskite Ferroelectric Nanostructures**
by F. Peter (2006), 106 pages
ISBN: 3-89336-444-7

12. **Molecular Electronic Building Blocks Based on Self-Assembled Monolayers**
by B. L ssem (2006), 138 pages
ISBN: 3-89336-454-4

Band/Volume 12
ISBN 3-89336-454-4

Informationstechnik
Information Technology